Master's thesis

NTNU
Norwegian University of Science and Technology
Faculty of Engineering
Department of Marine Technology

Eirik Tysseland Holmefjord

Numerical and Experimental Investigation on a Circular FOWT Foundation with a Moonpool

Master's thesis in Marine Technology
Supervisor: Professor Trygve Kristiansen
June 2023

NTNU
Norwegian University of
Science and Technology

Eirik Tysseland Holmefjord

Numerical and Experimental Investigation on a Circular FOWT Foundation with a Moonpool

Master's thesis in Marine Technology
Supervisor: Professor Trygve Kristiansen
June 2023

Norwegian University of Science and Technology
Faculty of Engineering
Department of Marine Technology

NTNU
Norwegian University of
Science and Technology

Department of Marine Technology

Master Thesis

Numerical and Experimental Investigation on a Circular FOWT Foundation with a Moonpool

Author:
Eirik Tysseland Holmefjord

June 2023

Preface

This thesis is the final work of my Master of Science Degree within Marine Hydrodynamics in Marine Technology at the Department of Marine Technology (IMT) at the Norwegian University of Science and Technology (NTNU) in Trondheim, Norway.

The motivation for the chosen subject in this thesis has been the growing potential in renewable resources where floating offshore wind is a big investment area as well as an interest of the hydrodynamic aspects of floating structures. The thesis investigates the presence of a moonpool and its associated effects and how varying sizes of horizontal and vertical damper plates influence the rigid body motion in regular waves. The concept that has been studied is developed by Sevan SSP. The goal of this concept is to provide a cost-effective solution for the floating offshore wind industry to offer renewable energy at a lower cost.

Eirik Tysseland Holmefjord

Trondheim, June 10, 2023

Acknowledgements

Several people have been central in completion of this thesis which deserves my sincere gratitude.

This thesis has been under the supervision of Professor Trygve Kristiansen. His knowledge and guidance within the field of hydrodynamics have been fundamental for completion of the work that has been conducted. He has always been available for my questions, and his quick response in both weekends and late evening have been most appreciated.

I would like to thank Terje Rosten, Robert Opland and Trond Innset for the great help during the planning and execution of the experiments. Their knowledge on instrumentation, model construction and experimental testing have been crucial in completion of the experiments.

I would also like to thank Mael Korentin Ivan Moreau for great help with the numerical simulation and meshing procedure. His help during numerical crisis have been most prominent and the numerical work would not have been as successful without his guidance.

Finally, i would like to thank Richard Verley and Lise Kvittingen for expert help during the finalization of the thesis.

Abstract

The present work investigates different variations of horizontal and vertical damper plates on a circular floating offshore wind turbine concept with a large centred moonpool. This is done through both experimental and numerical procedures. The concept in question is developed by Sevan SSP, which have expertise in the design of cylindrical hulls and have been a provider for offshore oil and gas production for many years. They are using their knowledge in developing a cost-effective solution for the floating offshore wind turbine industry.

A potential flow solver called Wamit have been utilized for the numerical simulations and the experimental work have been conducted in the Small Towing Tank at NTNU. Five different horizontal damper plates have been tested as well as one type of vertical damper plates situated inside the moonpool at 90° and 270° normal to the incoming waves. A total of eight design configurations have been tested. The main purpose of testing different sizes of damper plates is to see if this could reduce the pitch motion at kR=0.7-0.9 by approximately 25%. Results is presented in term of response amplitude operator, RAO.

A parametric study on two of the design configuration involving adding an approximate damping value for viscous damping as well as varying the inertia term I_{55} have been conducted. A new set of RAO were produced in MATLAB using the linear added mass, damping and restoring coefficients as well as excitation forces evaluated by Wamit. The aim of this study is to investigate methods on implementing viscous effects in domains that exclude viscosity. This study showed that both viscous damping and viscous excitation is prominent on this type of concept.

The results from the numerical simulation and experimental work showed that the rigid body motion changed significantly with the different type of horizontal damper plates. The configuration with the largest horizontal damper plate showed the best result at kR=0.7-0.9. The vertical damper plates indicated little to no improvement on the motion. The moonpool takes up a substantial proportion of the concept which means that the free-surface motion inside the moonpool is bound to affect the rigid body motion. Sloshing and piston-mode resonance is two major type of free-surface motion that can occur for this type of concept which have been studied here. The results showed that the first transverse sloshing mode cancels out the surge motion almost completely at kR=1.8-2.5 depending on which horizontal damper plate were attached. The piston-mode also marked its presence at kR=1.3 which indicated some cancellation of the motion in heave for one design configuration.

Sammendrag

Denne oppgaven undersøker forskjellige variasjoner av horisontale og vertikale dempeplater på et sirkulært flytende vindkraft konsept som innehar et stort sentrert "moonpool". Arbeidet er blitt utført både eksperimentelt og numerisk. Det gjeldende konseptet er utviklet av Sevan SSP, som har stor ekspertise innen design og utvikling av sirkulære skrog, og har vært en stor bidragsyter for olje og gass næringen i lang tid. De bruker nå sin ekspertise til å utvikle et kostnadseffektivt design innenfor flytende offshore vindkraft.

Wamit, et numerisk panel kode program basert på lineær potensial teori, har blitt brukt til de numeriske simuleringene og eksperimentene er blitt utført i Lilletanken på NTNU. Fem forskjellige horisontale dempeplater har blitt undersøkt samt ett sett med vertikale dempeplater montert i konseptets "moonpool" ved henholdsvis 90° og 270° normalt på de innkommende bølgene. Totalt, åtte forskjellige konfigurasjoner har blitt testet. Hovedhensikten ved å teste forskjellige størrelser av disse dempe platene er om dette kan gi en 25% reduksjon i stamp bevegelse rundt kR=0.7-0.9. Resultatene er presentert i form av respons amplitude operator, RAO.

En parametrisk studie ble gjennomført på to av designkonfigurasjonene ved å legge til en omtrentlig dempingsverdi for viskøs demping og variere treghetsmomentet I55. En ny serie RAO ble produsert i MATLAB ved hjelp av de lineære koeffisientene for tilleggsmasse, dempning og hydrostatisk stivhet samt eksitasjonskrefter kalkulert av Wamit. Målet med denne studien er å undersøke metoder for implementering av viskøse effekter i domener som ekskluderer viskositet. Denne studien viste at både viskøs demping og viskøs eksitasjon er betydelige for denne typen konsept.

Resultatene fra eksperimentet og de numeriske simuleringene viste at bevegelsen endret seg betydelig med de forskjellige horisontale demperplatene. Konfigurasjonen med den største horisontale demperplaten gav det beste resultatet ved kR=0.7-0.9. De vertikale demperplatene viste liten eller ingen forbedring av bevegelsen. "Moonpoolen" tar opp en betydelig del av konstruksjonen, noe som betyr at bevegelsen av fluidet i "moonpoolen" vil påvirke konstruksjonens bevegelse betraktelig. Skvulping og stempel bevegelses resonans (sloshing og piston-mode) er to viktige typer bevegelse av væskeoverflaten som kan oppstå for denne type konsept, som også er studert her. Resultatene viste at den første skvulpe-modusen omtrent kansellerer jag bevegelsen helt ved kR=1.8-2.5, avhengig av hvilken horisontal demperplatesom var festet. Stempeleffekten markerte også sin tilstedeværelse ved kR=1.3, noe som indikerte en viss kansellering av bevegelsen i hiv for én av designkonfigurasjonene.

Contents

Nomenclature

$\boldsymbol{A}(\omega)$	Frequency dependent added mass matrix
$\boldsymbol{B}(\omega)$	Frequency dependent damping matrix
$\boldsymbol{C}$	Restoring matrix
$\boldsymbol{F}_{exc}$	Excitation force matrix
$\boldsymbol{M}$	Mass matrix
$\boldsymbol{u}$	Velocity vector
$\ddot{\eta}$	Acceleration
$\Delta\omega$	Frequency interval
$\dot{\eta}$	Velocity
ϵ	Wave steepness
ϵ_n	Phase angle
η	Motion/position
η_{ja}	Motion amplitude in mode j
η_j	Motion in mode j
Λ	Scale factor
λ	Wave length
∇	Vector of partial derivatives
ω	Wave frequency
ω_p	Peak frequency
ρ	Water density
φ, ϕ	Velocity potential
$\zeta(x,t)$	Wave elevation
ζ	Wave profile
ζ_a, ζ_{An}	Incident wave amplitude
$B_{jk}^{(1)}$	Linear damping coefficient
$B_{jk}^{(2)}$	Quadratic damping coefficient
$B_{jk}^{(eqv)}$	Equivalent damping coefficient
C_D	Drag coefficient
C_{jk}	Restoring coefficient
f	Wave frequency in Hz

F_m	Drag load term in Morison equation
$f_{m,i}(r,\theta)$	Surface of a 3D standing wave
f_p	Peak wave frequency in Hz
g	Gravitational acceleration
H	Wave height
h	Water depth
H_{m0}	Significant wave height
$J_m(k_r r)$	Bessel function
k	Wave number
$l_{m,i}$	Roots of the Bessel function
p	Pressure
T_P	Piston-mode resonance period
$T_{m,i}$	Natural sloshing period
T_p	Peak period
u	Horizontal particle velocity
u_r	Relative velocity
u_w	Incident particle velocity
V	Wind speed
v	Kinematic viscosity
$x_{An}(\omega_i)$	Response amplitude

Chapter 1

Introduction

The industry today is facing a major shift from fossil fuel to renewable energy as a cleaner source of electricity. This is where floating offshore wind comes into play as this is at present an area that has not yet fully been explored. There are many advantages of offshore wind compared to wind farms on land such as larger area to utilise, more stable wind conditions and less controversy. There are also some disadvantages which are mainly due to the complexity and cost. The need for more research on this topic is therefore highly desirable.

Sevan SSP has developed a wind-power generation concept that shows promising results. Sevan SSP have expertise in the design of cylindrical hulls and have been a provider for offshore oil and gas production for many years. They are now using this knowledge to develop their own design for a floating offshore wind turbine, denoted FOWT. Their design is a so-called small waterplane area cylindrical hull, denoted SWACH, which could provide a cost-effective design if acceptable results are obtained. The concept has a circular moonpool present which takes up a substantial portion of the concept. This means that the complex behaviour of moonpools is bound to affect the rigid body motion in both advantageous and disadvantageous ways. Sloshing and piston-mode are two resonant phenomena that are excited by external waves and could lead to an increased motion of the free-surface and ultimately increase the rigid body motions. These effects may also result in cancellation effects which could substantially reduce the motion at certain frequencies. The idea is to study and utilize these effects to hopefully provide the desired outcome.

1.1 Literature Review

The literature review was completed during the project thesis and is presented here in full. The aim of this review is to try to capture essential information about previous work on moonpools, and associated effects such as sloshing-mode and piston mode resonance.

Moonpools provide a highly complex dynamic problem that is not yet fully understood. They typically exist in ships and barges where the moonpools take up a small proportion of the total size of the body. For the wind concept established by Sevan SSP, the moonpool takes up a substantial proportion of the total structure which means it could have a considerable effect on the motion and response of the body. This makes it necessary to learn more about moonpools and associated effects to hopefully achieve beneficial results for the SWACH concept.

Extensive research has been conducted on moonpools and approximately 20 years ago Molin (2001) studied the sloshing-and piston-modes on a new barge concept with rectangular moonpools. He established a theoretical model based on linearized potential flow theory in two and three dimensions. The results showed that the natural frequencies of the longitudinal sloshing modes increased with decreasing draught and width. The water depth was assumed infinite, and the horizontal dimensions of the barge (beam and length) were both assumed infinitely long compared to the moonpool dimensions, so the equations and results may not be comparable with the work in this project thesis; nevertheless this is still relevant information to consider. Further in 2018 a paper by Molin et al. (2018) was published where the theoretical model from Molin (2001) was further developed considering finite water depth and horizontal barge dimensions. In the paper they studied a circular moonpool using both methods, (infinite and finite assumptions): this is more relevant for this project thesis. In Molin et al. (2018), the theoretical model is compared with results from WAMIT, and Figure 1.1 shows natural frequency of the piston-mode for a circular moonpool. It can be seen that the results obtained using WAMIT agree well with the proposed model.

In 2021, Reiersen et al. (2021) published an article where they studied a rectangular body employing two moonpools as a pitch reducing device. The study was conducted experimentally, numerically and with an approximate theory similar to that developed by Molin (2001). Forced heave and pitch motion were studied as well as a freely floating case. Different moonpool inlets were investigated, seen in Figure 1.2.

The results showed that the square and rounded inlet configurations showed the best results with regards to the pitch cancellation problem. This was mostly due to how the flow separation formed at the inlets, indicating that flow separation can be an important damping mechanism for moonpool resonance problems. There was also an undesired effect of the moonpool where both pitch and heave resonance periods were close to the cancellation period such that a larger response was obtained compared to a corresponding body without moonpools. This article, in particular generated some ideas with regards to

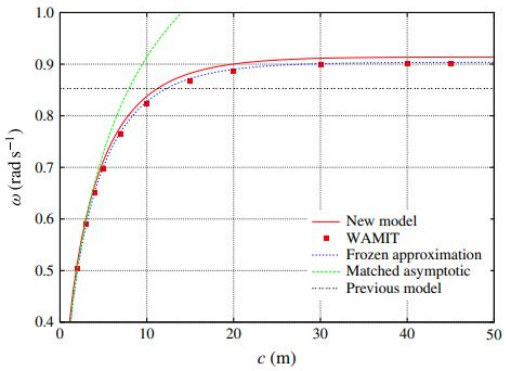

(a) Natural frequency of the piston mode for a=10 m, d=5 m, b=30 m, and varying c.

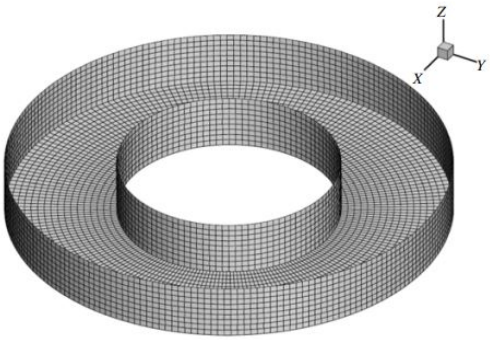

(b) Circular moonpool that shows the paneling used in WAMIT.

Figure 1.1: Results for the different methods in Figure 1.1a and the body in question in Figure 1.1b (Molin et al. 2018).

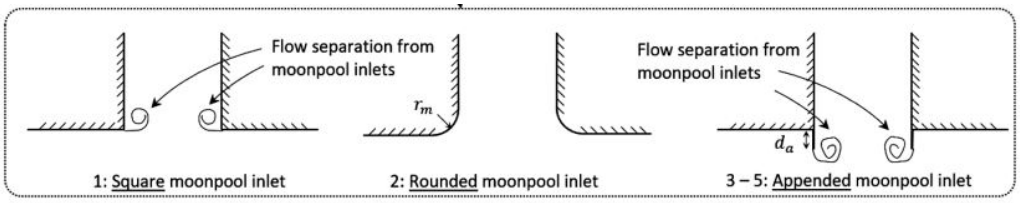

Figure 1.2: Moonpool inlet configuration from the article Reiersen et al. (2021) showing how it affect flow separation.

flow separation that would be interesting to look into. More detailed information on these ideas can be found in Chapter 4.

A majority of the investigations conducted on moonpools has considered 2D scenarios. There is less information regarding freely floating bodies with moonpools and their effects. However, Moreau et al. (2022) investigated an upright bottomless cylinder floating in waves, a similar design to the SWACH wind concept. The purpose of the body in question was to serve as a floating dock for installing deep-draft floating wind turbines. Damping investigation of surge and pitch motion as well as the first lateral sloshing mode was the subject of this study. Also considered were baffles mounted inside the moonpool with different perforation ratios, the intention of which was to dampen the sloshing motion and corresponding heave and surge motions. The results showed that the solid baffles provided more damping of the sloshing motion. The perforated plates also showed good results. This article was a major inspiration for the master thesis by Wettre (2022) where she conducted numerical and experimental investigations on the same concept as in the present project thesis. However the results did not yield the desired outcome of reduced pitch motion for a certain period range. Different baffles mounted inside the moonpool were investigated, however with little improvement in the body motion.

Mukhlas (2017), as part of his master thesis, investigated the roll damping effects of varying bilge-box sizes for a two-dimensional ship section. The results showed that the damping coefficient increased with increasing bilge-box length. The added mass in roll

also increased for larger bilge-boxes. This might be self- evident since the structure has to move more water. But this increase in added mass also has an effect of shifting the natural period of the structure. However, Mukhlas (2017) is less relevant for the present work due to the absence of a moonpool. It did nonetheless spark the idea of adjusting the bilge-boxes on the Sevan SWACH concept to see the effect this might have.

1.2 Objectives

Preliminary results from Sevan SSP have shown excessive pitch motions for wave periods around 12-14s (SevanSSP 2022). If this response can be reduced by approximately 25%, the concept can be further developed. During the work done in the project thesis in the autumn, several ideas around design variation were generated; these are explained in more detail in Chapter 4. These ideas are a result of the literature review and discussion with my supervisor Professor Trygve Kristiansen. The scope of work of this master thesis is listed below;

- Gain a better understanding of moonpools and dynamic behaviour of rigid body motions.
- Perform experiments on the SWACH concept with particular focus on design variations of the skirts and introducing two vertical damper-plates inside the moonpool.
- Perform experiments on the SWACH concept with particular focus on design variations of the skirts and introducing two vertical damper-plates inside the moonpool.
- Perform numerical simulation on the design configurations of the SWACH concept.
- Perform a parametric study on I_{55} and an approximate investigation on including viscous damping on the results from the numerical simulations.
- Discuss results and propose further work.

1.3 Project Thesis

This master thesis work is a continuation of the project thesis work conducted in the autumn 2022 and parts of it have been included here. The main focus of the project thesis was to perform a literature review on moonpools, conduct preparatory work and obtain a solid theoretical foundation for the work in this thesis. Therefore, much of the content with regards to the introduction and theory comes from the project thesis but in an improved and more relevant form. The literature review has also been included here in its full extent.

Chapter 2

Theory

In this chapter, relevant theory, governing equations and important quantities established from several well known authors and books are presented.

2.1 Governing Equations

2.1.1 Navier-Stokes Equations

The Navier-Stokes equations are the governing equations of fluid motion often referred to as momentum equations. They were developed in early to mid-19th century by the French engineer and physicist Claude-Louis Navier and Anglo-Irish physicist and mathematician George Gabriel Stokes. They are derived from Newton's second law of motion. The fluid is imagined to be divided into numerous small elements in order to solve for its motion and obtain the pressure that provides the main part of wave loads acting on a body. Figure 2.1 shows a simplified sketch of the idea behind the equations.

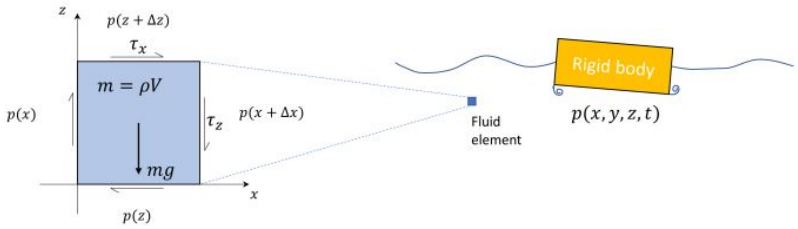

Figure 2.1: Simplified sketch of pressure and shear forces acting on a fluid element (Bachynski-Polic et al. 2021).

The Navier-Stokes equation in Cartesian coordinates is as followed:

$$\frac{\partial \boldsymbol{u}}{\partial t} + \boldsymbol{u} \cdot \nabla \boldsymbol{u} = -\frac{1}{\rho}\nabla p + \boldsymbol{g} + v\nabla^2 \boldsymbol{u} \tag{2.1}$$

The equation in full is a set of three partial differential equations with four unknowns. This is where the continuity equation,

$$\nabla \cdot \boldsymbol{u} = 0, \tag{2.2}$$

comes in which states that, what comes in must go out of a fixed control volume. ∇ is defined as a vector of the partial derivatives ($\nabla = \partial/\partial x, \partial/\partial y, \partial/\partial z$). The quantity $\mathbf{u} = (u, v, w)$ is the velocity vector of the fluid element (Bachynski-Polic et al. 2021). This system of equations, together with the continuity equation, governs the motion of a viscous fluid subject only to the assumptions of constant density and a Newtonian stress-strain relationship (Newman 2017). This system of equations is very complex to solve and for complex bodies it is practically impossible to solve analytically. Therefore, considerable research has been conducted over the last decades to develop practical usage of these equations. They can roughly be divided into two categories: Computational fluid dynamics (CFD), which solves the momentum equations numerically, and potential flow theory which is a simplification of the momentum equations by assuming zero viscosity.

2.1.2 Potential Flow Theory

Potential theory, which is very relevant in this thesis, is a state-of-the-art method to predict forces on and motions of bodies. The main assumption of this method is that there are no shear forces acting on the fluid element, such that the shear term in Equation 2.1 disappears. This is referred to as inviscid fluid. Further it is assumed that the flow is irrotational. This is expressed mathematically as $\nabla \times \mathbf{u} = 0$. A velocity potential, φ, is introduced and can be expressed as $\mathbf{u} = (u, v, w) = \nabla\varphi$. Due to the introduction of irrotational flow we get the following equation:

$$\nabla \boldsymbol{u} = 0 \quad \text{and} \quad \boldsymbol{u} = \nabla\varphi \Rightarrow \nabla^2\varphi = 0 \tag{2.3}$$

This is also known as the Laplace equation which ultimately results in a fluid that is assumed incompressible and inviscid while the flow is assumed irrotational. This yields both advantages and drawbacks. The biggest advantage is that it is practical and fast. The biggest drawback is that it does not capture any flow separation effects at all. For many applications this is good enough, but for resonance problems, for example the roll motion of a ship this might be inadequate. Flow separation at the bilge-keels, resulting in drag loads, is a critical damping mechanism at roll resonance and in fact provides the only source of damping (Bachynski-Polic et al. 2021).

2.2 Rigid Body Motions

A rigid body can be described mathematically to respond in six degrees of freedom, three translational and three rotational, as shown in figure Figure 2.2.

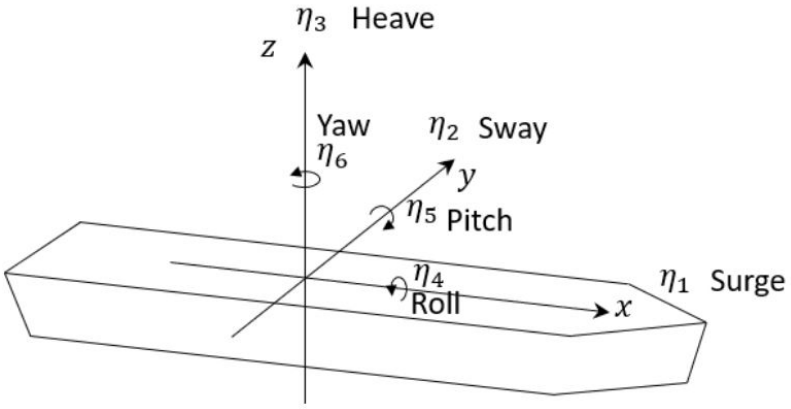

Figure 2.2: Illustration of six degrees of freedom (Bachynski-Polic et al. 2021).

The motion of a rigid body floating in waves can be found by solving the equation of motion:

$$(\mathbf{M} + \mathbf{A}(\omega))\ddot{\eta} + \mathbf{B}(\omega)\dot{\eta} + \mathbf{C}\eta = \mathbf{F}_{exc} \tag{2.4}$$

The bold notation reflects that it is in a matrix-vector form because of six degrees of freedom. The mass matrix is in principle a full six by six matrix but for the Sevan concept symmetry about xz- and yz planes, reduces the matrix to:

$$\mathbf{M} = \begin{bmatrix} M & 0 & 0 & 0 & Mz_g & 0 \\ 0 & M & 0 & -Mz_g & 0 & 0 \\ 0 & 0 & M & 0 & 0 & 0 \\ 0 & -Mz_g & 0 & I_{44} & 0 & 0 \\ Mz_g & 0 & 0 & 0 & I_{55} & 0 \\ 0 & 0 & 0 & 0 & 0 & I_{66} \end{bmatrix} \tag{2.5}$$

2.3 Linear Hydrodynamic Loads

The linear wave-induced loads and the corresponding motion of a body is usually obtained by solving the radiation and diffraction problem. The wave excitation forces are computed in the diffraction problem by obtaining the linear dynamic pressure due to waves and multiplying this dynamic pressure with the body normal and integrating over the mean wetted body surface in each degree of freedom as shown below.

$$F_j^{exc} = \int_{S_0} p_d n_j dS = \rho \int_{S_0} \frac{\partial \varphi_0}{\partial t} n_j dS + \rho \int_{S_0} \frac{\partial \varphi_7}{\partial t} n_j dS \tag{2.6}$$

The velocity potential φ_0 is known a-priori whereas the velocity potential φ_7 in general must be solved using a numerical method. The last integral in Equation 2.6 is the diffraction force, while the second last term is the Froude-Kriloff force.

The hydrodynamic loads from the radiation problem yields expressions for the added mass and damping coefficients. The load can be expressed as the sum of the velocity and acceleration of the body in any mode as,

$$F_{jk}^{hd} = -A_{jk}\frac{d^2\eta_j}{dt^2} - B_{jk}\frac{d\eta_j}{dt} \tag{2.7}$$

which defines the added mass and damping coefficients, A_{jk} and B_{jk}, respectively. In principle, there is a total of 36 added mass and damping coefficients, but if there is symmetry about one or more axes, some terms will reduce to zero. There will inevitably be cross-terms which means that for instance a hydrodynamic pitch moment F_{53}^{hd} will occur due to forced oscillation in heave. If the body has front-aft symmetry, such as the Sevan concept, this term will reduce to zero. There will likely be cross-terms for surge and pitch, such as A_{15} and A_{51} which means that the motion in pitch will be strongly influenced by the motion in surge and vice versa. The restoring coefficients are a result of the change in hydrostatic pressure and displaced volume of the body and, unlike the added mass and damping they are not frequency dependent. The restoring term can be expressed as,

$$F_{jk}^{hs} = C_{jk}\eta_j \tag{2.8}$$

where the superscript hs means hydrostatic. There will also be cross-terms for the restoring coefficient in the same way as for the added mass and damping coefficients. If the body has no forward speed or is subject to current, the cross terms can be shown to be equal such that $C_{jk} = C_{kj}$, $A_{jk} = A_{kj}$ and $B_{jk} = B_{kj}$ (Faltinsen 1990).

2.4 Linear Wave Theory

Linear wave theory, often called Airy theory, is a useful tool considering regular waves propagating in x-direction. With the free-surface condition,

$$-\omega^2\phi + g\frac{\partial\phi}{\partial z} = 0 \quad \text{on} \quad z = 0 \tag{2.9}$$

together with the Laplace equation (2.3), and the sea bottom condition,

$$\frac{\partial\phi}{\partial z} = 0 \quad \text{on} \quad z = -h \tag{2.10}$$

it is possible to derive the linear wave theory. Results for finite water depth in terms of velocity potential, ϕ, wave frequency, ω, and wave profile, ζ, are:

$$\phi = \frac{g\zeta_a}{\omega}\frac{\cosh(k(z+h))}{\cosh(kh)}\cos(\omega t - kx) \tag{2.11}$$

$$\omega^2 = k\tanh(kh)g \tag{2.12}$$

$$\zeta = \zeta_a \sin(\omega t - kx) \tag{2.13}$$

The advantage of using linear wave theory, is that analyses can be conducted in the frequency domain. In this approach, the steady-state response is solved for each wave frequency, producing the so-called *Response Amplitude Operator* also denoted RAO.

RAO-Response Amplitude Operator

The RAO, also called the transfer function, describes the ratio between the incident wave and response in mode j of the body,

$$H_j(\omega) = \frac{\eta_j a}{\zeta_a} \tag{2.14}$$

In terms of heave RAO, the equation of motion can be rearranged to produce the heave RAO:

$$\frac{\eta_3 a}{\zeta_a} = \frac{f_3 a}{-\omega^2(M + A_{33}) + i\omega B_{33} + C_{33}} \tag{2.15}$$

This requires the added mass, damping and restoring effect to be known. In order to keep these formulations in a compact form, the RAO is expressed with complex numbers which means the RAO is in fact complex valued.

2.4.1 Regular Waves

A regular wave is characterized by constant period, amplitude and wavelength. A regular wave can be described through the wave period and wave steepness $\epsilon = H/\lambda$, where the wavelength is related to the wave period through the wave number $k = 2\pi/\lambda$. The wave number k is found from the dispersion relation which is briefly described for finite water depth in section 2.4. The definition of water depth outlined in Bachynski-Polic et al. (2021) states that $h/\lambda \geq 0.5$, is referred to as deep water. Finite water depth is defined when $0.05 \leq h/\lambda \leq 0.5$. The different waves that will be utilized in the experiment and simulation will result in water depths within both of these ranges.

2.5 Second Order Effects

Second order effects such as viscous effects are not captured by linear potential flow theory but can have a significant impact on a structure's behaviour. A brief discussion on how to implement this into the linear theory is given below.

2.5.1 Viscous Loads

Due to the design of the Sevan SWACH body, there is bound to be flow separation at several points on the body. Especially the skirts will generate vortices and viscous effects will be important. The viscous effects are often difficult to properly account for in a simple manner and in potential flow theory they are not accounted for at all. One way to include viscous loads, is the Morison equation and more specifically the drag term only:

$$F_m(t) = \frac{1}{2}\rho D C_D u|u| \tag{2.16}$$

The drag coefficient and particle velocities are well established for circular objects that are subject to current or oscillating flows like waves. Some trouble arises for the SWACH concept as these terms are not well defined for this kind of concept especially for bodies with skirts. In addition, the body moves in the waves which introduces more complexity. It is possible to deal with these challenges by replacing the u term in Eq. 2.16 with a relative velocity u_r. This term will include the incident particle velocity, the heave and pitch motion when expressed in the coupled form of heave and pitch,

$$u_r = u_w - \dot{\eta_3} + \dot{\eta_5} b \tag{2.17}$$

Where b is the distance the load takes place for the pitch motion. By inserting this expression into Eq. 2.16, it yields,

$$F_m(t) = \frac{1}{2}\rho D C_D (u_w - \dot{\eta_3} + \dot{\eta_5} b)|(u_w - \dot{\eta_3} + \dot{\eta_5} b)| \tag{2.18}$$

The relations above have been established for a two-dimensional circular cross-section, but the theory applies well for three dimensional bodies as well. The difference in Eq. 2.18 would be that the term, D, is replaced by a projected area, A, normal to the incoming oscillating flow.

2.5.2 Viscous Damping

For structures with bilge-keels or skirts, viscous damping might be nontrivial and often the only source of damping, as in the roll resonance motion of ships which depends solely on the bilge-keels for damping, which is why these are so important. For the SWACH concept, the same philosophy holds true due to the skirts. This will induce flow separation which will result in additional damping effects that can be described with a quadratic damping model. By including the quadratic damping term in the equation of motion, it can be written as,

$$\sum_{j=1}^{6} \Big((M_{kj} + A_{kj})\ddot{\eta}_j + B_{kj}^{(1)}\dot{\eta}_j + B_{kj}^{(2)}\dot{\eta}_j|\dot{\eta}_j| + C_{kj}\eta_j \Big) = F_j^{exc} \tag{2.19}$$

The quadratic damping coefficient $B_{kj}^{(2)}$ has to be found from experiments or CFD. For a ship, it is also possible to apply a 2D CFD of a mid-ship section and apply a strip theory approach Bachynski-Polic et al. 2021, but this would not be a valid approach for the SWACH concept due to its circular design. The quadratic term is non-linear which means it can be used directly in a time domain simulation and solving for the roll motion time-step by time-step. Another approach is to use something called an *equivalent linearisation*. In practical terms this means that the quadratic term is linearized around a chosen amplitude, in this case for pitch. The linearized damping term can be written as,

$$B_{kj}^{(eqv.)} = B_{kj}^{(1)} + B_{kj}^{(2)}\dot{\eta}_j \tag{2.20}$$

and the updated equation of motion then becomes,

$$\sum_{j=1}^{6}\Big((M_{kj} + A_{kj})\ddot{\eta}_j + B_{kj}^{(eqv.)}\dot{\eta} + C_{kj}\eta_j\Big) = F_j^{exc} \tag{2.21}$$

Chapter 3

Moonpools

A moonpool is an opening from deck to keel in ships and barges and is used for marine operations where it is desirable to shield the operations from external weather. It is also used for drilling operations for FPSO's. The moonpool can experience piston-mode and sloshing-mode resonance effects, where the motion of the liquid inside the moonpool can be larger than the incident waves acting on the ship. This can lead to unwanted motion of the water in the moonpool and even unwanted motion of the vessel.

3.1 Sloshing

Sloshing is a resonant phenomenon where liquid with a free-surface is confined in a tank or tank-like construction. Sloshing is a horizontal motion that can be described as a standing waves and can occur in various forms or modes. The motion can be symmetrical or asymmetrical and the sloshing resonance is not necessarily excited by the largest external waves. This means that the external wave induced loads can often be described by linear theory (Faltinsen and Timokha 2009). Figure 3.1 illustrates six different linear sloshing modes confined in a 2D rectangular tank derived by Faltinsen and Timokha (2009). These different modes can be excited by different frequencies. Typically, the exciting frequency increases with increasing mode numbers. The first sloshing mode is generally most important since this anti-symmetrical wave has the largest wave elevation at the tank walls.

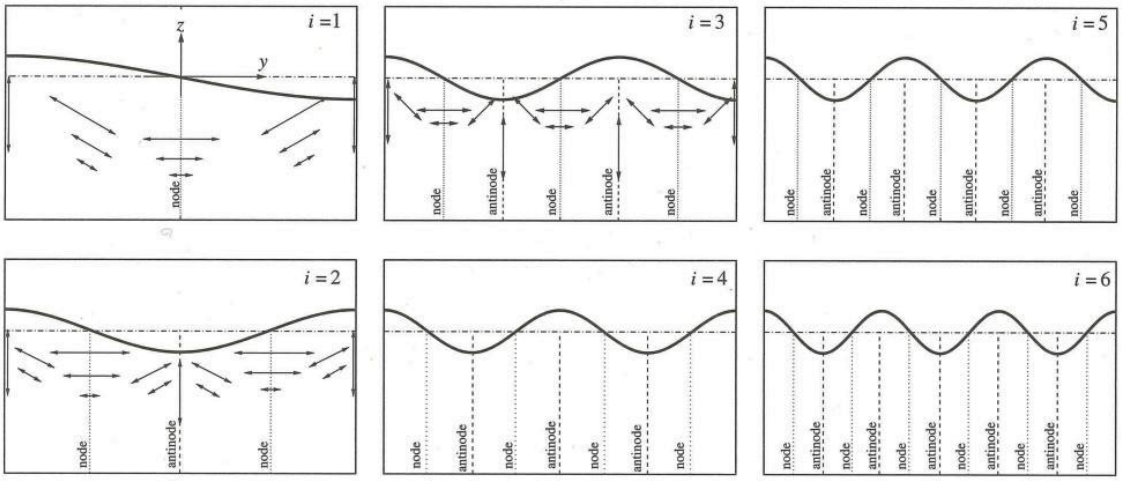

Figure 3.1: Standing waves corresponding to odd and even sloshing modes of a rectangular 2D tank. i=1,3,5 refers to the antisymmetrical modes and i=2,4,6 refers to the symmetrical modes (Faltinsen and Timokha 2009).

In order to estimate the natural sloshing frequencies in a vertical circular cylindrical tank, the procedure is usually performed in cylindrical coordinates (r, θ, z). This is then linked to the Cartesian coordinate system by the transformation $x = rcos\theta, y = rsin\theta, z = z$.

The surface wave pattern of a standing wave can be expressed as:

$$f_{m,i}(r,\theta) = \varphi_{m,i}(r,\theta,0) = J_m\left(l_{m,i}\frac{r}{R_0}\right) \times \begin{cases} cos(m\theta) \\ sin(m\theta), \end{cases} \quad m = 0,1,...; \quad i = 1,2,... \tag{3.1}$$

With the corresponding natural frequencies,

$$\sigma_{m,i}^2 \frac{R_0}{g} = R_0 k_{m,i} = l_{m,i} tanh\left(\frac{l_{m,i}h}{R_0}\right), \quad m = 0,1,...; \quad i = 1,2,... \tag{3.2}$$

Writing this equation in terms of the natural wave period yields;

$$T_{m,i} = \frac{2\pi}{\sqrt{gl_{m,i}tanh\left(\frac{l_{m,i}h}{R_0}\right)/R_0}} \tag{3.3}$$

In order to solve Eq. 3.3, the nondimensional term, $l_{m,i}$ needs to be solved with a known Bessel function $R(r) = J_m(k_r r)$. If this is not known then the first natural sloshing period can be estimated using Figure 3.2, where R_0 is the radius of the moonpool. The figure shows different sloshing periods of varying cylindrical radius and height.

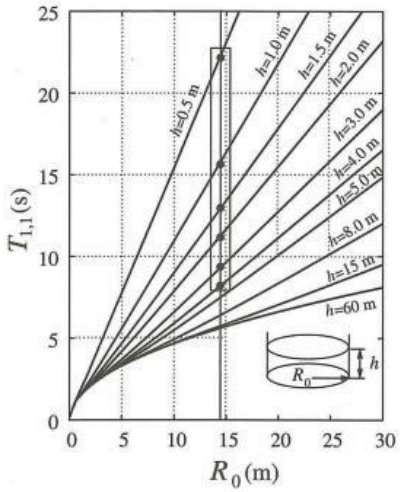

Figure 3.2: Natural period for the first sloshing-mode for a circular tank with varying radius and height (Faltinsen and Timokha 2009).

3.2 Piston Mode

Another resonance phenomenon is piston-mode oscillation. The liquid is moving like a rigid body almost only vertically inside the moonpool. The resonance occurs in a frequency range where the vertical motion of a vessel is relatively large and the frequency corresponds to the piston-mode frequency. A general notion is that the piston-mode motion is larger for a moonpool with smaller cross-section. Flow separation at the inlet of the moonpool or by plates could cause significant damping. A typical damping mechanism in ships with a moonpool is to use perforated plates at the moonpool wall. An illustration of this piston-mode behaviour can be seen in Figure 3.3a. Figure 3.3b shows how the first sloshing mode could look like. The figures are used for illustration purposes only and originate from the article *Design, modelling, and analysis of a large floating dock for spar floating wind turbine installation* by Jiang et al. (2020).

Molin (2001) derived a method to estimate the natural frequency for piston mode behaviour where the volume inside the moonpool is assumed to be a solid body. For a circular moonpool as in this project thesis, the natural frequency can be estimated as,

$$\omega_p = \sqrt{\frac{C_{77}}{M_p + A_{77}}} \tag{3.4}$$

where the added mass of the fluid volume inside the moonpool $A_{77} = \frac{2}{3}\rho r^3$, the restoring term $C_{77} = \rho g A_{w_{mp}}$ and M_p is the mass of the fluid volume inside the moonpool.

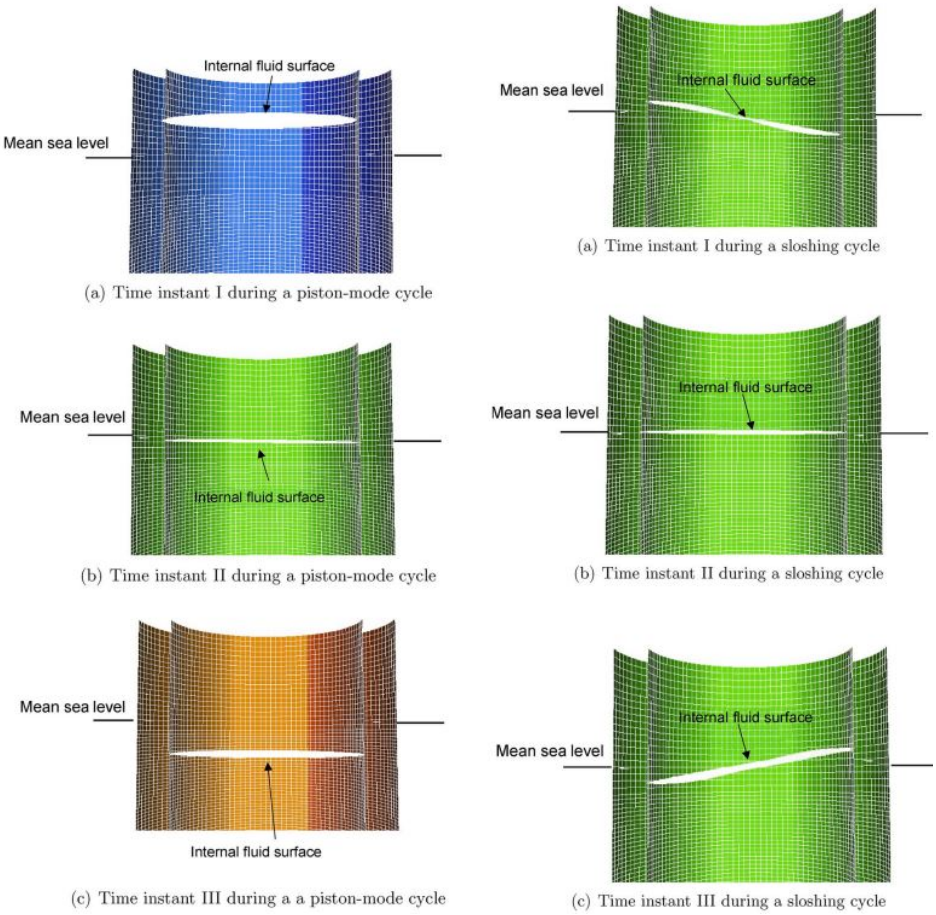

(a) Time instant I during a piston-mode cycle

(b) Time instant II during a piston-mode cycle

(c) Time instant III during a a piston-mode cycle

(a) Time instant I during a sloshing cycle

(b) Time instant II during a sloshing cycle

(c) Time instant III during a sloshing cycle

(a) Piston mode (b) Sloshing

Figure 3.3: Visualization of the piston-mode and sloshing motion at different time instances (Jiang et al. 2020).

Chapter 4

Experiment

This chapter describes the experimental setup and model test alongside with the post-processing procedure for the experimental data. The planning of the experimental work started in autumn 2022 during the project thesis in collaboration with the lab technicians and supervisor and further developed in January/February 2023 for this thesis. The experiment is based on the work done by Wettre (2022) and the same basic model has been used with modifications and Figure 4.1 shows the 1:100 scaled model prior to the modifications. The model has an intricate weight system that consist of 16 steel rods placed with equal spacing around the model which can be seen in Figure 4.1a and Figure 4.1b. These rods are approximately 35mm in diameter with a height of 94mm. Sufficient buoyancy elements are placed below the steel rods (not shown here). The yellow items that are placed on the top of the model are small weights used to tweak the model to the correct draught. The model is equipped with a horizontal damper plate permanently mounted on the underside of the model which is the main design parameter that is subject to design variation in this thesis work.

(a) (b)

Figure 4.1: The existing model used in the experimental work prior to modifications.

The experiments have been conducted in the Small Towing Tank (Lilletanken) at NTNU during March 2023. The tank measures 25 meters long, 2.5 meters wide and the water level for the experiment was set equal to 0.7 meters. The density is assumed to be 1000 kg/m^3. An illustration of the model setup used in the experiment can be seen in Figure 4.2.

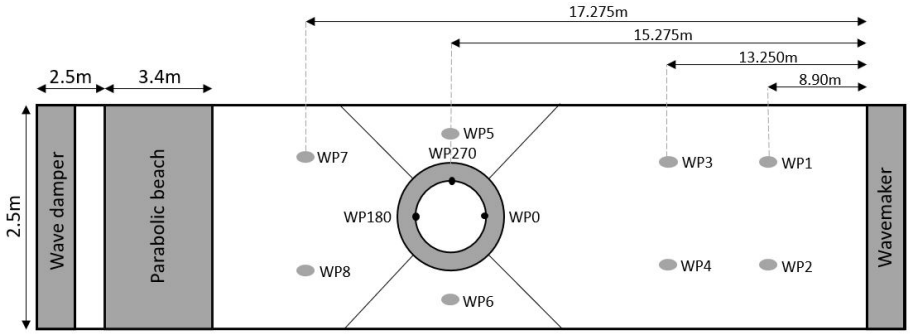

Figure 4.2: Illustration of the model setup used in the experiment.

Figure 4.3 shows the baseline model in the tank with four mooring lines and the instrument cable bundle attached. The mooring lines are connected in a 45° interval and the cable bundle is attached to the side at approximately 270° where 0° indicate the fore of the model. The picture shown in Figure 4.3a is taken upstream of the model.

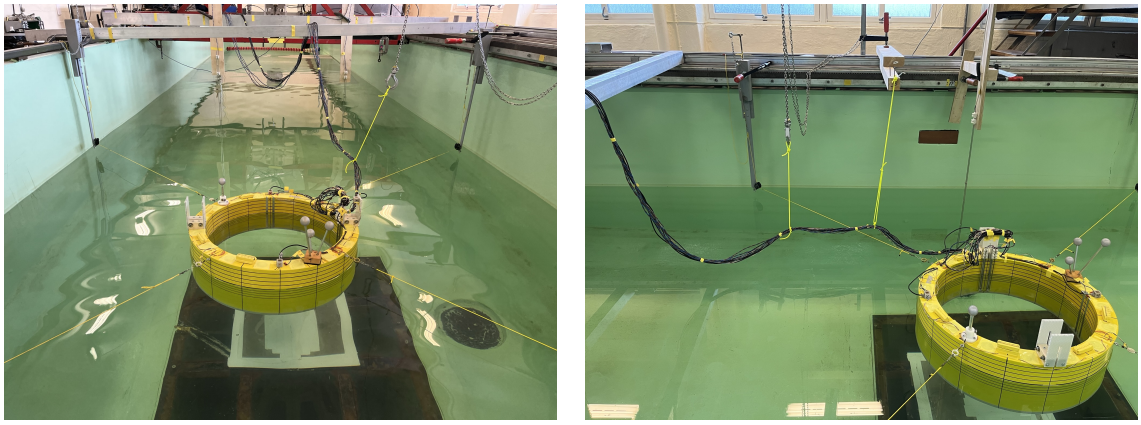

(a) (b)

Figure 4.3: Model setup showing one configuration of the model. 4.3b shows how the cable bundle is positioned behind the model in the setup.

The lab setup is similar to that used in Wettre's work. The model has been modified with different design changes with regards to the horizontal damper plate. A total of five different sizes of this horizontal damper plate have been tested. These plates usually influence the added mass and damping coefficient drastically which is a point of interest to investigate. A new detail has been added to the model, to be referred to as vertical damper plates. These are mounted inside the moonpool at 90° and 270° relative to the incoming wave. These are only present for two of the design configurations. It is known that bilge-keels on ships provide a crucial damping mechanism for roll resonance and this is the general idea behind these so-called vertical damper plates. The aim is to see if this design configuration will produce vortices during the sloshing motion and if these have

desired effects such as reducing the body motion in pitch specifically, or other unforeseen effects.

Instrumentation

The standard setup for measuring the motion in the Small Towing Tank is a system called Oqus. This is an optical tracking technology that enables capturing fast moving objects with high level of accuracy by utilizing cameras and reflective markers (Qualysis 2023). In case the Oqus system does not function as intended or fails completely, the model is equipped with three accelerometers. They are placed on top of the model at 0°, 180° and 270°. In order to achieve the desired pre-tension in the mooring lines, a force transducer was attached to each mooring line.

A total number of eight wave probes in the tank and four additional located on the model inside the moonpool have been used. The location of these have been presented in the lab setup illustration in Figure 4.2.WP1-8 refers to the wave probes placed in the tank and WP1-4 is placed upstream of the model to measure the incident waves. WP0, WP180 and WP270 refers to the wave tapes and wave probes located inside the moonpool in order to evaluate the surface elevation. Due to the presence of the vertical damper plates, two wave probes at 270° have been used where they are placed on both side of the plate which can be seen in Figure 4.4.

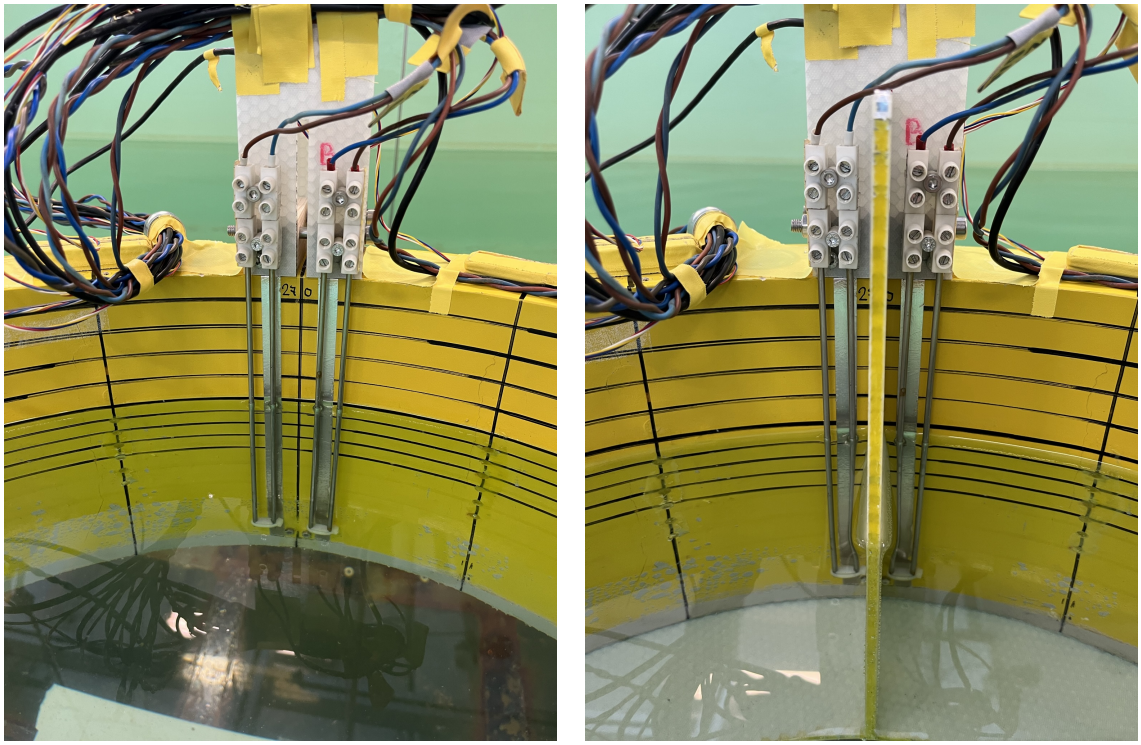

(a) (b)

Figure 4.4: The wave probe setup at 270° inside the moonpool in order to evaluate the damper plate influence on the wave elevation.

4.1 Scaling and Scale Effects

When conducting experiments on offshore structures, Froude scaling is commonly used to ensure similarity between gravitational and inertia forces from waves from full to model scale. By require geometrical and kinematic similarity and equality in Froude number F_N from full to model scale, will ensure similarity between inertial and gravitational forces (Steen 2014). Important quantities are summarized in Table 4.1.

Table 4.1: Scale ratio and how different quantities are scaled using Froude scaling (Steen 2014).

Physical parameter	Multiplication factor
Scale factor	$\Lambda = L_F/L_M$
Mass	$M_F = \Lambda^3 M_M$
Force	$F_F = \Lambda^3 F_M$
Moment	$M_F = \Lambda^4 M_M$
Acceleration	$a_F = a_M$
Time	$t_F = \sqrt{\Lambda} t_M$
Velocity	$U_F = U_M \sqrt{\Lambda}$

Ensuring the same Froude number in full and model scale is usually not an issue. Ensuring equal Froude number and Reynolds number at the same time from full to model scale is practically impossible which yields an important thing to discuss; gravitational and viscous forces are not scaled correctly at the same time. By calculating the mass force and drag force using the scale multiplication factor only, shows how scale effects increase the discrepancy for small models:

$$F_m = M_M a_m = \Lambda^3 1 = \Lambda^3$$

$$F_d = L_M U_M^2 = \Lambda \sqrt{\Lambda}^2 = \Lambda^2$$

This means that the drag force in model scale is Λ times too large compared to the mass force. This can yield more damping and further underestimate the rigid body motions. Therefore, it is vital to have the model as large as possible when conducting experiments to reduce this discrepancy. For this experimental work, an already exiting model were used and limitation in lab facilities did not allow to consider this other than discussing it as a potential bias error.

4.2 Model Parameters and Design Configurations

The parameters of the model and the modifications will be presented in this section. As previously mentioned, the main parameters of the model are the same as those used in Wettre's work. Figure 4.5 shows an overview of the main parameters in addition 3D views of the model visualized in Rhino with the new vertical damper plates in. The values of the main parameters of the model can be seen in Table 4.2.

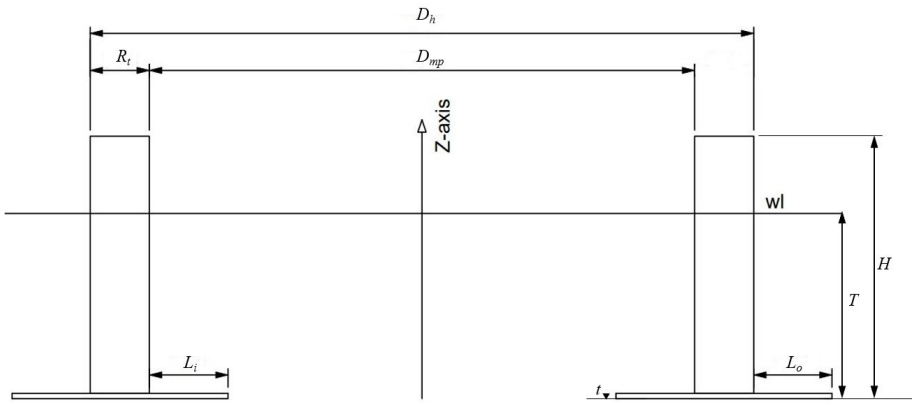

(a) 2D view of the model showing the main parameters of the model.

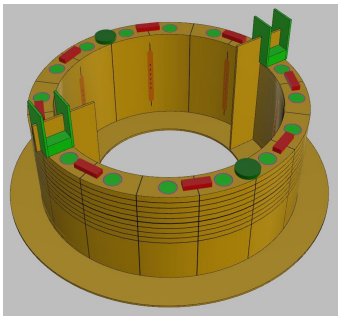

(b) Inner and outer skirt.

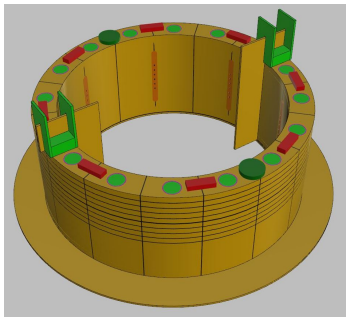

(c) Outer skirt only.

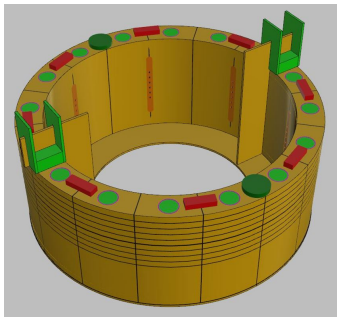

(d) Inner skirt only.

Figure 4.5: 2D section and 3D illustration of the model and its main parameters as made by lab technician Trond Innset.

Table 4.2: Model data of the main parameters.

Parameters	Symbol	Lab model [cm]
Model Height	H	26.1
Draught	T	18
Hull diameter	D_h	64.7
Moonpool diameter	D_{mp}	52.7
Hull thickness	R_t	5.75
Outer skirt length	L_o	See Table 4.3
Inner skirt length	L_i	See Table 4.3
Skirt height	t	0.5

The parameter L_o and L_i in Table 4.2 is referring to the horizontal damper plates. These terms have been introduced since at some design configurations, there is no presence of horizontal damper plates on either the outside of the model or either inside the moonpool

as Figure 4.5c and Figure 4.5d illustrates.

A list of the different design configurations is given below and the dimension of these design variations can be seen in Table 4.3.

1. **Configuration 1**: Without inner and outer skirt and no vertical damper plates.
2. **Configuration 2**: With inner and outer skirt and no vertical damper plates.
3. **Configuration 3**: Without inner skirt, with outer skirt and no vertical damper plates.
4. **Configuration 4**: With inner skirt, without outer skirt and no vertical damper plates.
5. **Configuration 5**: With 30% larger outer and inner skirt in relation to configuration 2 and no vertical damper plates.
6. **Configuration 6**: With 30% smaller outer and inner skirt in relation to configuration 2 with no vertical damper plates.
7. **Configuration 7**: Without inner and outer skirt with vertical damper plates.
8. **Configuration 8**: With inner and outer skirt and with vertical damper plates.

Table 4.3: Dimension of the different skirt variations. Configuration 7 and 8 refers to skirt dimension including the vertical damper plates.

Skirt dimensions		
	L_i [cm]	L_o [cm]
Conf. 1	0	0
Conf. 2	7.65	7.6
Conf. 3	0	7.6
Conf. 4	7.65	0
Conf. 5	9.75	9.85
Conf. 6	5.4	5.35
Conf. 7	0	0
Conf. 8	7.65	7.6
Vertical damper plates dimension		
-	Height [cm]	Width [cm]
Conf. 7/8	25	7.38

Table 4.4 shows the mass and mass-moments of inertia alongside the vertical centre of gravity where Vcg=0 is located in the free surface. Due to the symmetry of the model, it has been assumed that the centre of gravity in x and y directions are at the centre of the model. The values presented in this table have been provided by lab technician Trond Innset and are based on the 3D model made in Rhino. These are the values that have been utilized in the numerical work for the mass matrix. Due to the potential discrepancies between experimental and numerical results, these values may be different in the actual

model during the model tests which will be noticeable in the RAO's of the rigid body motion if the differences are large enough.

Table 4.4: Mass of the model and mass-moments of inertia as well as the vertical centre of gravity for the different configurations.

Parameter	M [kg]	I_{44} [kgm^2]	I_{55} [kgm^2]	I_{66} [kgm^2]	Vcg [m]
Conf. 1	19.61	0.942	0.940	1.693	0.009
Conf. 2	20.64	1.037	1.026	1.802	-0.001
Conf. 3	20.36	1.009	1.008	1.779	0.002
Conf. 4	20.19	0.982	0.980	1.734	0.003
Conf. 5	20.86	1.047	1.045	1.821	-0.003
Conf. 6	20.42	1.007	1.005	1.768	0.001
Conf. 7	19.77	0.953	0.942	1.702	0.009
Conf. 8	20.80	1.037	1.026	1.802	-0.001

Since the size of the moonpool takes up a substantial portion of the total volume of the body, sloshing and piston mode is assumed to impact the motion significantly. By using the relation provided in Figure 3.2 and Equation 3.4 for the sloshing and piston mode resonance respectively, estimates of the resonant frequencies for configuration 1 can be seen in Table 4.5.

Table 4.5: Resonant frequency of the piston-mode and first sloshing-mode presented in terms of kR number for configuration 1.

	Piston-mode [kR]	First sloshing-mode [kR]
Configuration 1	1.371	2.315

A major part of the work in this thesis has been to investigate the effects different sizes of damper plates have on the motion of the structure. As mentioned previously in this chapter, the model is tested with five different horizontal damper plates mounted at the underside of the model as well as two vertical damper plates mounted inside the moonpool. Figure 4.6 shows configuration 1-6 with the different skirts attached to the model in the tank. Configuration 1 has no damper plates attached which can be viewed as a baseline model.

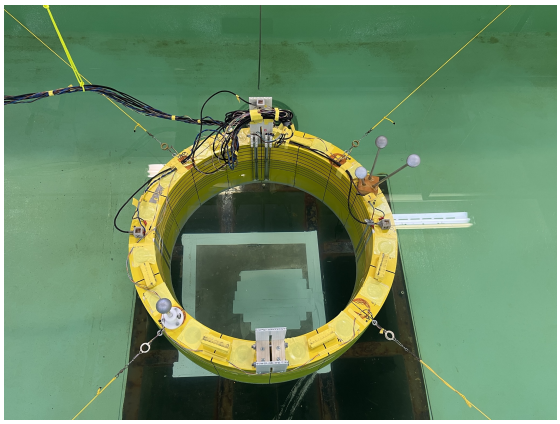

(a) Configuration 1

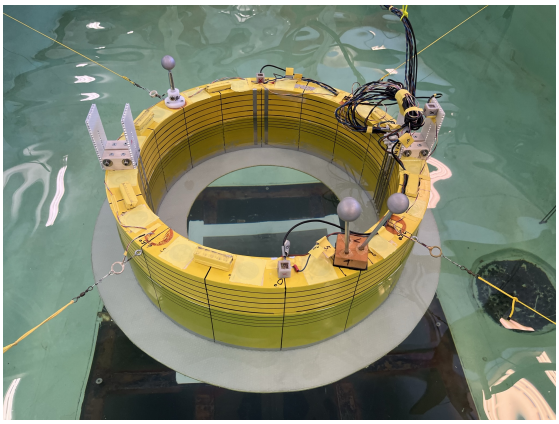

(b) Configuration 2

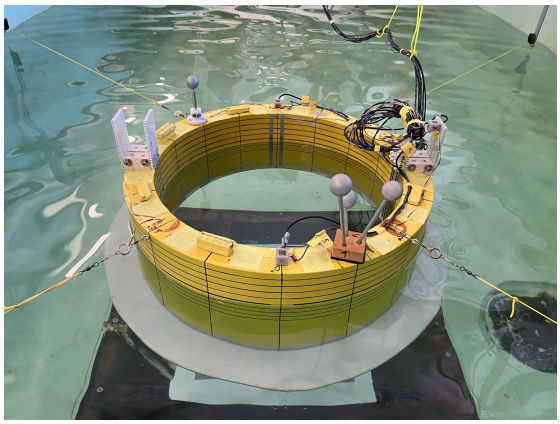

(c) Configuration 3

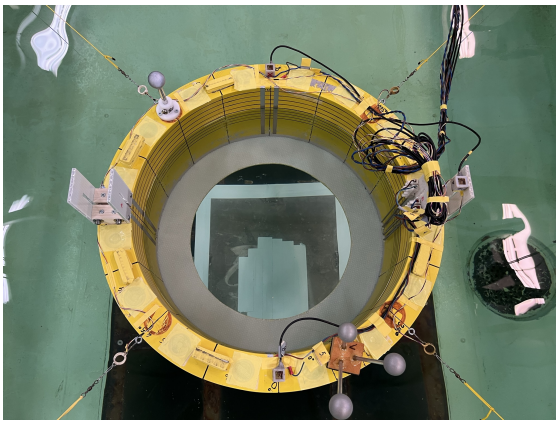

(d) Configuration 4

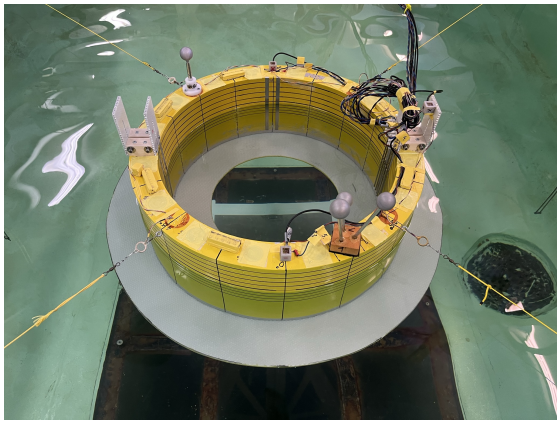

(e) Configuration 5

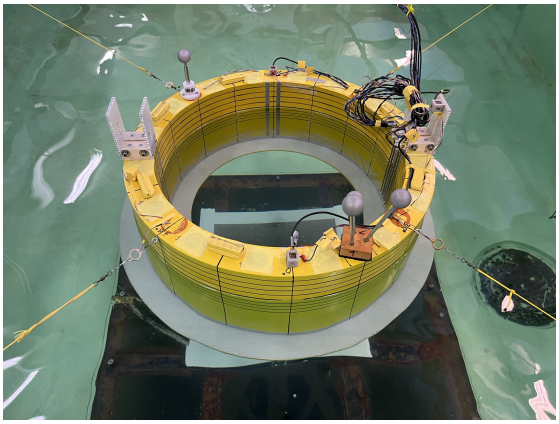

(f) Configuration 6

Figure 4.6: The model with all the different horizontal damper plates.

In order to be able to assemble and disassemble these plates in an easy manner, eight holes have been drilled at the underside of the model where a pipe with internal threads is glued tight inside each of these holes such that the plates could be fastened with bolts. This made it possible to easily assemble and disassemble the skirts while the model was in the tank, reducing both time and work. Figure 4.7 shows more clearly how the plates are attached to the model. These pictures were taken after the experiment was done. Figure 4.7c and Figure 4.7d show the underside of the model where it can be seen that two of these fastening mechanisms are missing. These came loose during an assembly

phase due to over tightening of the bolts. This may have led to more flexible behaviour of the skirts that were only fastened with six bolts rather than eight.

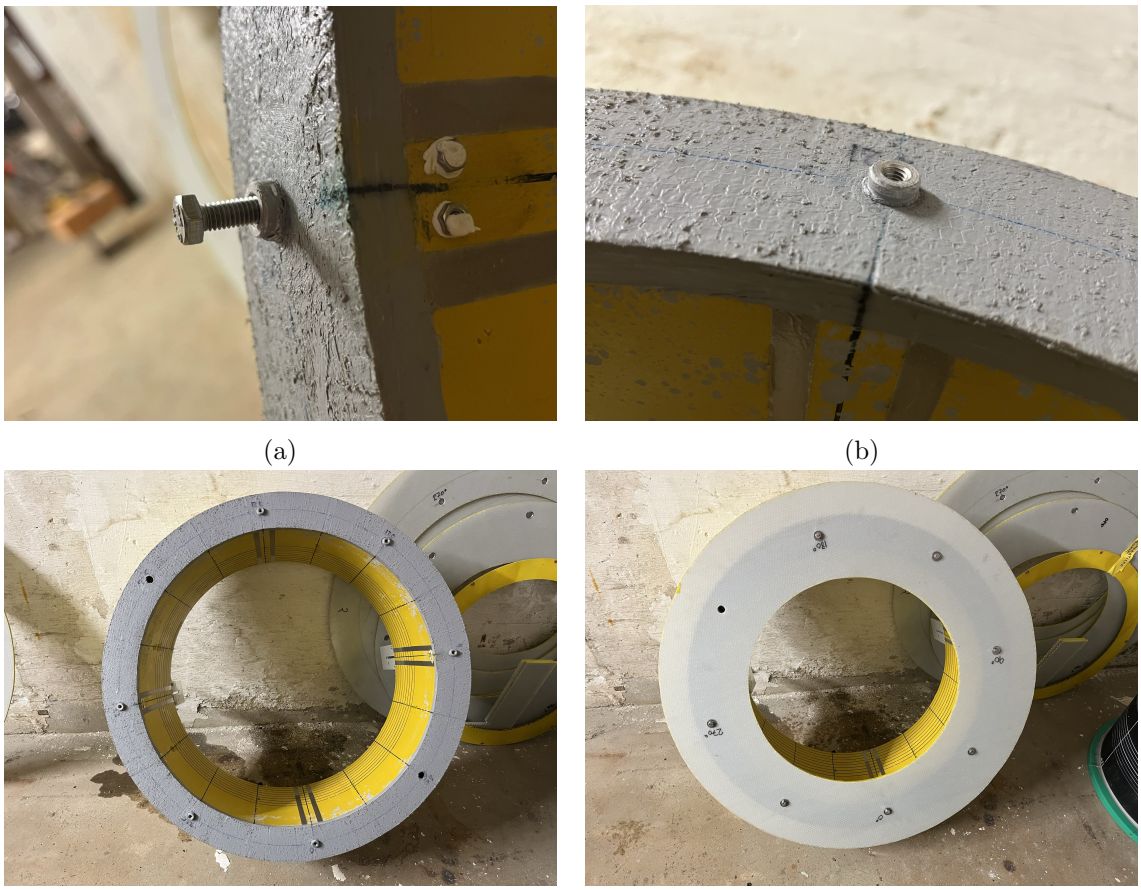

(a) (b)

(c) (d)

Figure 4.7: Detailed photograph of how the horizontal damper plates are assembled onto the model.

Since the vertical damper plates are only present in two of the design configuration, they were required to be removable. Figure 4.8a shows the damper plates and Figure 4.8b shows the device that the plates are mounted in. As can be seen in the latter figure, there is a slot which the plate slides into and is then fastened with through-bolts secured with nuts on the backside. Figure 4.8c and Figure 4.8d shows the fully assembled vertical damper plates.

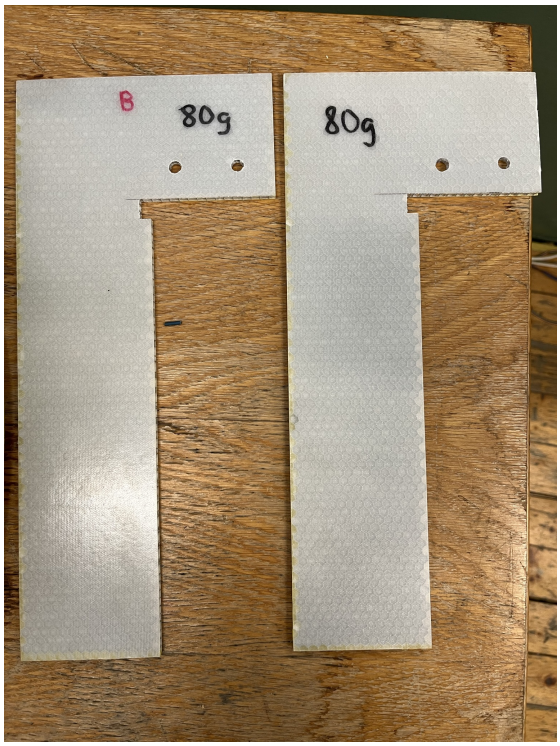

(a) Vertical damper plates.

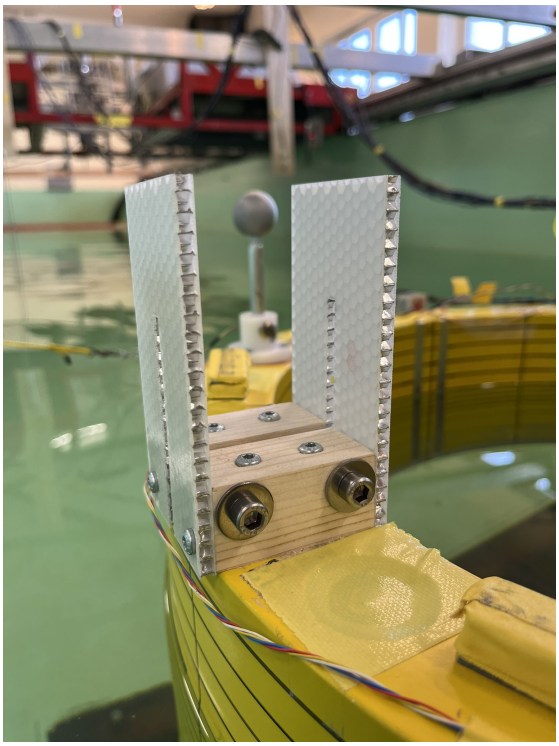

(b) Mounting device for the plates.

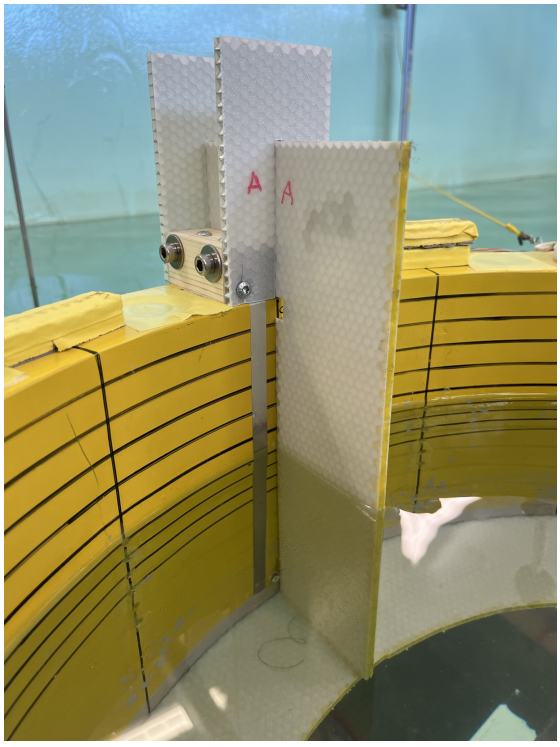

(c) Vertical damper plate at 90°.

(d) Vertical damper plate at 270°.

Figure 4.8: Snapshot of the vertical damper plates mounted inside the moonpool.

Figure 4.9 shows configuration 7 and 8 where the vertical damper plates are assembled.

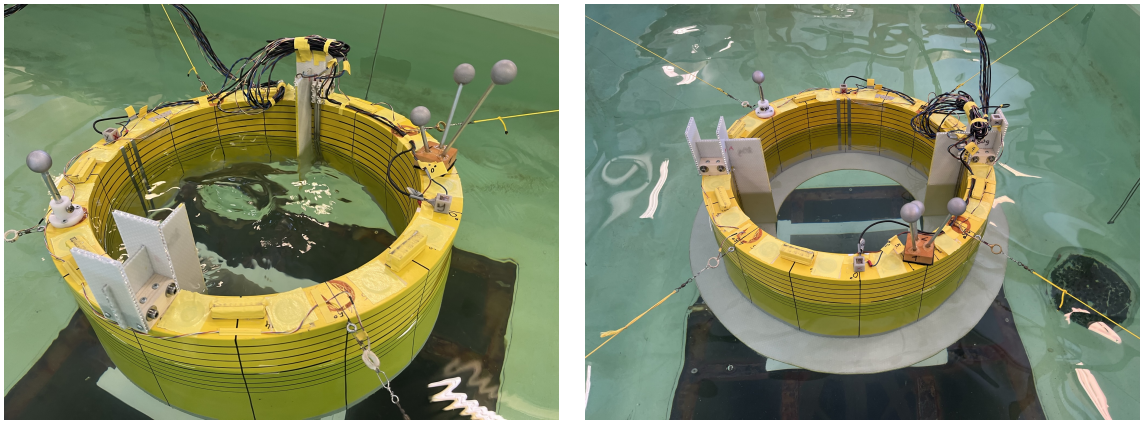

(a) Configuration 7 (b) Configuration 8

Figure 4.9: Snapshot of configuration 7 and 8 showing the model with the vertical damper plates mounted.

From the master thesis by Wettre (2022), it was evident that there were some issues with the cable bundle that attached the sensors to the model. Due to the number of sensors, the cable bundle became rather stiff and could influence the motion of the model and therefore influence the response. This is generally difficult to avoid completely in this kind of model setup but a general note is to have as little instrumentation as possible attached to the model. For this reason, in the model setup used in this thesis, there is no wave probe at 90° inside the moonpool. It was assumed that the wave elevation at position 90° and 270° would be similar enough due to the symmetry of the model and model setup. The presence of the vertical damper plates was also part of the decision as it made it necessary to have two wave probes, one on each side of the plate, as previously shown in Figure 4.4, in order to evaluate the influence the plates has on the wave elevation. There were also some issues with the mooring lines as they appeared to be too flexible which resulted in slow surge-motion and slack in the rear mooring lines during the most severe waves. The spring stiffness used in Wettre's master thesis was equal to 10 N/m with a pretension equal to 3 N. In this experiment, springs with stiffness equal to 25 N/m was used along with a pretension of 4 N. The mooring lines also produces additional restoring effects in mostly surge, pitch and coupled surge/pitch motion which can be calculated as,

$$C_{11} = 4k_x \tag{4.1}$$

$$C_{55} = F_{pre}D_h \tag{4.2}$$

$$C_{51} = C_{15} = 2k_x h \tag{4.3}$$

where k_x is the spring stiffness in x-direction, F_{pre} is the pretension in each mooring line, D_h is the hull diameter and h is the vertical distance from vcg to the mooring line.

4.3 Regular Wave Tests

The model has been subject to regular waves with different frequencies and wave steepness. It is easier to find the resonant frequencies in regular waves than irregular waves so that is one main reason for doing this. Also, linear wave theory is easy to implement to get some estimates in the results. In the planning stage and execution of the experiment the location of where the concept will be installed was not known so it was chosen to use wave data for the northern North Sea. A typical wave period range of interest is between 5-20s (0.5-2s in model scale) for this area and Table 4.6 shows an excerpt of proposed wavelength, wave-height and wave steepness in model scale.

Table 4.6: An excerpt of regular waves.

		$\epsilon = 1/100$	$\epsilon = 1/60$	$\epsilon = 1/40$	$\epsilon = 1/30$
k	λ[m]	H[m]	H[m]	H[m]	H[m]
16.0972	0.390	0.0039	0.0065	0.0097	0.013
4.0521	1.563	0.0156	0.026	0.0391	0.0521
1.1445	5.4898	0.0548	0.0915	0.1372	0.1829

The input that generates the wave signal needed for the wavemaker has been given in terms of the wavenumber, k. The wavenumber range has been from 16.0972 to 1.1445 that is equivalent to waveperiods 0.5 to 2.3s. A total amount of 37 wavenumbers has been tested, equivalent to wave period 0.5 to 2.3s with steps of 0.5s. The choice of this particular step is mainly due to time limitations. Table 4.7 shows the test procedure for all runs which has been the same for all wave steepness's and design configurations. The total time in the table is for one wave steepness only and a total of four different steepness's have been investigated resulting in a total test time for each design configuration equal to about 14 hours.

Table 4.7: Test procedure

Min. k	Max. k	Num. of k	Num. of k cycles	Rest time [s]	Total time [hours]
1.1445	16.0972	37	60	300	3.5

4.4 Sources of Errors

When conducting lab experiments, possible errors are usually present which can affect the results. In this experimental work, several uncertainties and inaccuracies were known in advance and also discovered during the experiment. This section aims to summarize some of these errors that are deemed most important to discuss.

Uncertainties in Wave Probes and Water Tank Level

The wave probes measure the wave elevation by using the conductivity of the water. The measurement will be influenced by temperature, which then affects the water density, and viscosity. By using the table on page 175 in Faltinsen (1990), it is possible to estimate the uncertainty in temperature and viscosity. The change in density and viscosity for each degree change in water temperature between 15° and 20° Celsius is estimated to be $\pm 2.8{\cdot}10^{-8}[m^2/s]$ and $\pm 0.18[kg/m^3]$ respectively. This results in possible deviation of 2.8% for the viscosity and 0.018% for the density. The temperature was monitored continuously, and no significant change could be observed. Due to leakage in the tank, the water level varied between 0.6-0.7m which required refilling of the tank. This is normally not an issue but due to construction work in the area, the available water for the refilling was household intake freshwater. In order to use the conductivity of the water, it requires to contain some chloride. Since the refilling water does not contain the same amount of chloride as the original tank water this might very well be a source of error. It is assumed, however, that the added water is such a small proportion compared to the total amount of water in the tank that this has not affected the measurements in any significant way. Another equally or more important reason to ensure the water level is the same for all tests is to assure the tension and pretension in the mooring lines stays the same.

Uncertainties in the Model

In order to tweak the model to the desired draught, it was ballasted with small weights placed on the top of the model. It was difficult to get the model completely level at the right draught resulting in the model having a small constant angle at approximately 0.02° in roll in all tests. The reason for this difficulty is because of the instrumentation setup on the model as the cable bundle was attached approximately on the side of the model. It was also noted that changing from one design configuration to another, the draught altered with a maximum difference of 0.1cm from the lowest to highest draught. This is due to the extra buoyancy the horizontal skirt produces. It was decided not to reballast the model for every design configuration mainly due to time limitation.

The horizontal skirt was fastened with eight bolts during the assembly phase. The nuts that these bolts are fastened into were glued into the model which makes it very easy to over-tightening the bolts such that the nuts loosen. This happened with two of the bolts meaning that for some test runs the skirt was only fastened with six bolts. It is rather difficult to quantify the influence this issue might have on the results, but the probability that this would produce significant errors is rather low.

Incident Waves

The regular waves in this experiment were created using provided MATLAB scripts as input to the wavemaker. Figure 4.10 shows the measured wave elevation at wave probe three and four alongside with the calculated wave elevation. It can be seen that the calculated wave corresponds best at the lower wavenumbers for all wave steepness's. There is a transition from infinite to finite water depth at wavenumber equal to 4.4672. Since the method of finding the wavenumber has been used under the assumption of finite water depth, it may be the reason for why the calculated waves fit better to the measured ones for the largest waves at wavenumber around 4 to 1. Another possible and perhaps more likely reason for the discrepancies is that the waves at high kR number are so small and difficult to measure with sufficient accuracy.

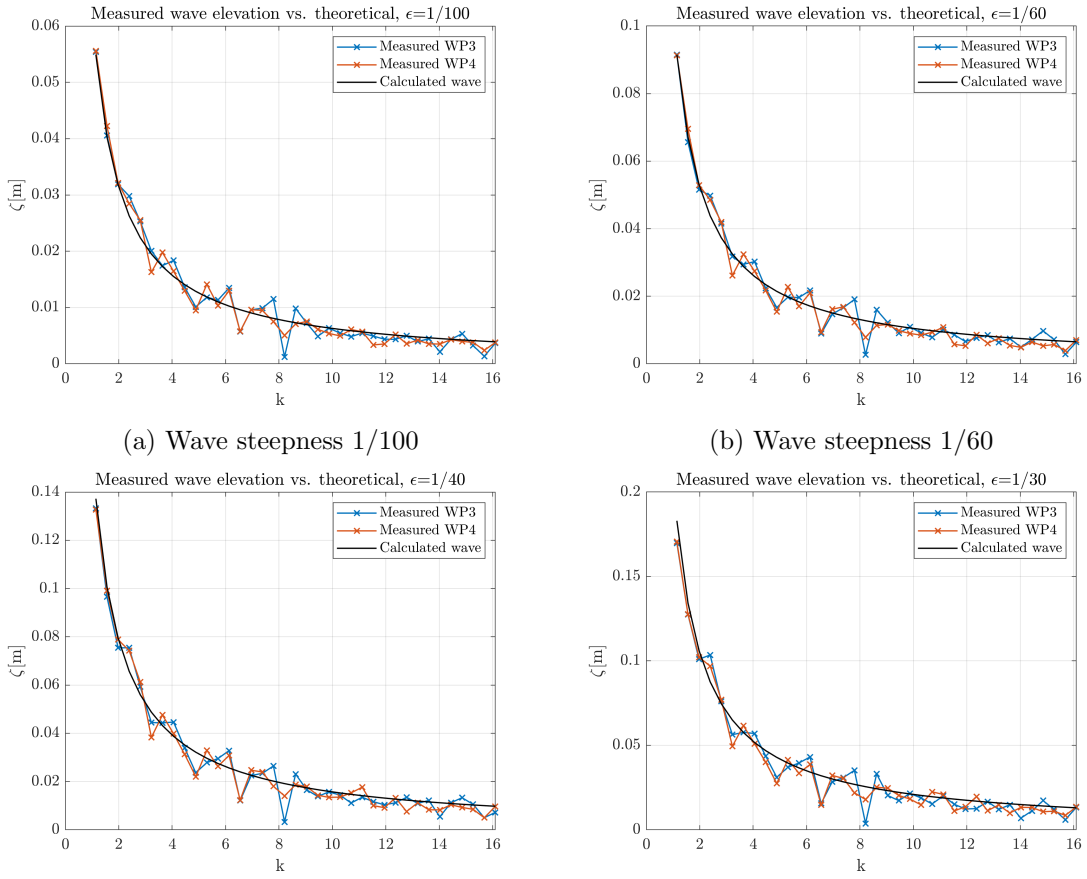

(a) Wave steepness 1/100

(b) Wave steepness 1/60

(c) Wave steepness 1/40

(d) Wave steepness 1/30

Figure 4.10: Measured wave elevation at WP3 and WP4 with the calculated wave elevation in black as a function of the wavenumber k.

Mooring Lines

The mooring lines were attached to the model in a 45° interval, where each of them needs to be fastened manually by someone in the tank where each mooring lines is adjusted

separately while trying to place the model at its intended location. Due to the setup in the small towing tank, it is very difficult to achieve the exact same pretension in all mooring lines while also having the model placed centred in the tank. As a result of this, the pretension varied from 4.1 N to 4.6 N as well as the model being slightly off centre. In addition, the model was somewhat skewed approximately 0.001° in yaw. This is however a rather small value that is most likely negligible for the results.

Viscous Loads

As outlined in Section 4.1, scale effects can have a significant impact on the results. As the proportion of drag force will be higher in this experiment than it would be in full scale, the viscous effects will be different in model scale than full scale. This will lead to both under and overestimation of the viscous effects depending on how prominent viscous damping and viscous excitation will be for this model. Since this error is systematically present in all tests and affecting the results in the same way, it would classify as a bias error.

4.5 Post Processing

Post processing of experimental data can be quite time consuming, which holds true in this thesis work. A short description of the process of obtaining the desired results from the raw data is presented here.

Regular Waves

As described in Section 4.3 the regular waves were run for 3.5 hours for each wave steepness resulting in total run time of 14 hours. Each wavenumber was repeated 60 times with a 5 minute break between the different wavenumbers. The main point of the post processing is summarized below:

- Extracting the correct time window from the total time series for each wave number by excluding the wait time between each wave number.
- Using a Butterworth band-pass filter to remove unwanted noise and higher order effects. Cut-off range corresponding to ±30% of the first harmonic frequency was used in order to obtain the first harmonic response.
- Finding the steady-state interval of the filtered time window as shown in Figure 4.11 and calculating the mean displacement in this steady-state response.

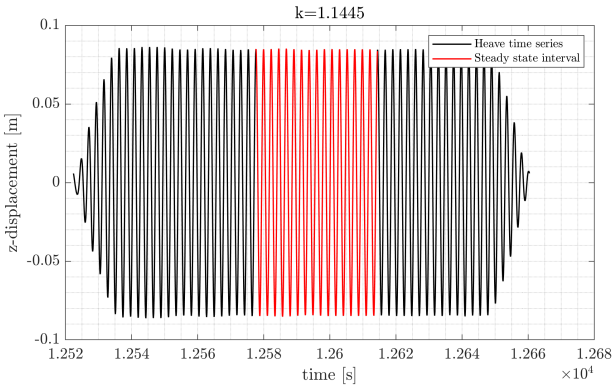

Figure 4.11: Steady-state interval marked in red for heave time series at wavenumber equal to 1.1445.

- By obtaining the mean displacement from the steady-state response and using the mean wave height from the wave probe measurements the RAO can be found using the relation in Equation 2.14.

Coordinate System

The free surface elevation inside the moonpool is measured by wave tapes and wave probes in a body fixed coordinate system. In order to evaluate the free-surface elevation without the influence from the rigid body motion, it must be transformed into the earth fixed coordinate system. This can be done by the relation,

$$WE^{EF} = WE^{BF} + Z_i \tag{4.4}$$

where WE^{EF} represents the earth fixed displacement, WE^{BF} represent the body fixed displacement and Z_i is the vertical displacement of s_3 at a point i given by the relation,

$$s_3 = \eta_3 + y\eta_4 - x\eta_5 \rightarrow s_3 = \eta_3 - x\eta_5 \tag{4.5}$$

where the roll motion is assumed negligible for the vertical displacement due to symmetry of the model. The roll motion is also not evaluated in the work conducted in this thesis.

Chapter 5

Numerical Method

For the numerical analyses, a program called WAMIT has been utilized. Version 7.4 of this particular program has been recommended as it allows inclusion of tank-wall effects. This will give a better basis for comparison of the numerical results with the experimental work. The focus for the numerical work has been on performing a mesh sensitivity study, investigating the motion of the body and also evaluating quantities such as added mass and damping. The analysis has been designed in a way that it is as similar to the experimental setup as possible in order to get fewer discrepancies in the results.

5.1 WAMIT

WAMIT is a panel-code program that solves the radiation and diffraction problem in potential flow. It is mainly developed for analyses of the interaction of surface waves with offshore structures. The software consists of two subprograms called POTEN and FORCE. POTEN solves for the radiation and diffraction velocity potentials on the body surface whereas FORCE computes global quantities such as the hydrodynamic coefficients, motions and first- and second-order forces. In order to perform simulations, a variety of input files must be assembled. The main files that are required are as follows; A *.gdf* file which describes the body using panels, a *.pot* file which includes physical quantities such as water depth, wave-numbers, etc., a control file, *.cfg*, that determines options for the analysis such as inclusion of tank wall effects and level of accuracy of the analysis, and a *.frc* file that includes physical properties of the body such as mass, radius of gyration, external restoring effects such as mooring lines and what quantities the FORCE module is to solve for. The *config.wam* file describes the work and license directory and *fnames.wam* specifies all the mentioned files to be included in the simulation. All of these files are needed to perform analyses and must be modified according to the desired outcome. Figure 5.1 shows how these subprograms cooperate. The subprogram FORCE can evaluate a variety of quantities specified in the $.frc$ file and in this thesis, the body motion is of most

interest. Other quantities of interest that have been evaluated are added mass and damping coefficients as well as excitation forces. The output from Wamit is in nondimensional form given by the relations below:

$$\bar{A}_{ij} = \frac{A_{ij}}{\rho L^k} \qquad \bar{B}_{ij} = \frac{B_{ij}}{\rho \omega L^k} \qquad \bar{\eta}_i = \frac{\eta_i}{A/L^n} \qquad \bar{X}_i = \frac{X_i}{\rho g A L^m}$$

The parameters L^k, L^n and L^m are called length scale parameters which have been set equal to one for the simulations. The X_i component is evaluated by either direct integration of the hydrodynamic pressure or the Haskind relations.

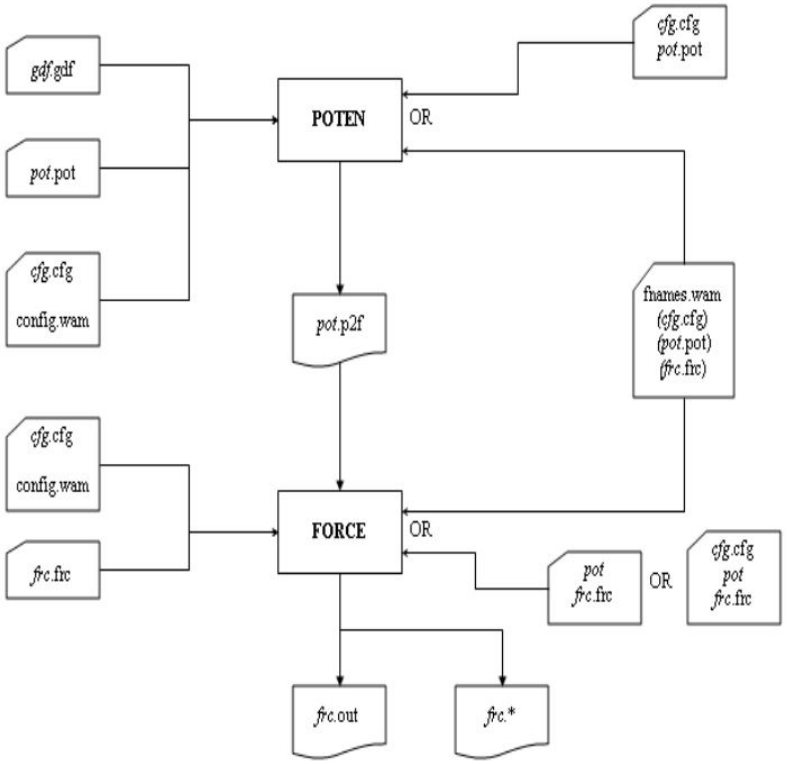

Figure 5.1: Outline of the POTEN and FORCE subprogram routine (Massachusetts Institute of Technology Inc and WAMIT Inc 2020).

Limitations

Wamit is based on linear potential flow theory, with its consequence that no viscous effects are captured by the program. Due to the presence of the moonpool, horizontal and vertical damper plates on the model, viscous effects such as flow separation at the skirt tip, will be significant especially around resonant frequencies. The additional viscous damping due to flow separation might be quite significant which Wamit will not capture at all. It is therefore expected that Wamit will at least overestimate the motion at resonant frequencies. Viscous excitation is an equally important factor that Wamit do not consider, which it is expected that the response evaluated by Wamit will be underestimated where viscous excitation is prominent.

5.2 Mesh Convergence Study

As described in Section 5.1, the body must be represented by a mesh with an adequate number of panels. Two matlab scripts made by Mael Moreau have been utilized for this; *DockMeshing.m* and *nemoh2wamit_01a.m* which implements the program NEMOH (LHEEA-Lab 2022). This program converts the mesh made in matlab into the desired *.gdf* format needed in WAMIT. Figure 5.2 shows the meshed geometry generated by Matlab. Because of the symmetry in the xz- and yz-plane, it is only necessary to generate one quarter of the model. The specific geometry shown in Figure 5.2 represents configuration 1 as described in Chapter 4 and has been utilized in the convergence study. Several different mesh sizes have been investigated to obtain a suitable mesh for the simulations and an overview of the variations can be seen in Table 5.1. In order to evaluate the mesh variations, some parameters must be chosen to indicate the variation with mesh size. The added mass and damping in heave have been the main parameters chosen to evaluate this. The RAOs in surge, heave and pitch have also been included to investigate if these motions are affected.

Table 5.1: Number of panels generated by Matlab and the corresponding number of panels in the *.gdf* file produced by NEMOH. Total number of panels in WAMIT is four times the values listed in the table for configuration 1 to 6.

Mesh	1	2	3	4	5	6	7	8	9
N panels Matlab	600	800	1000	1200	1400	1600	1800	2000	2200
N panels in WAMIT	546	754	819	1170	1287	1560	1651	1781	2028

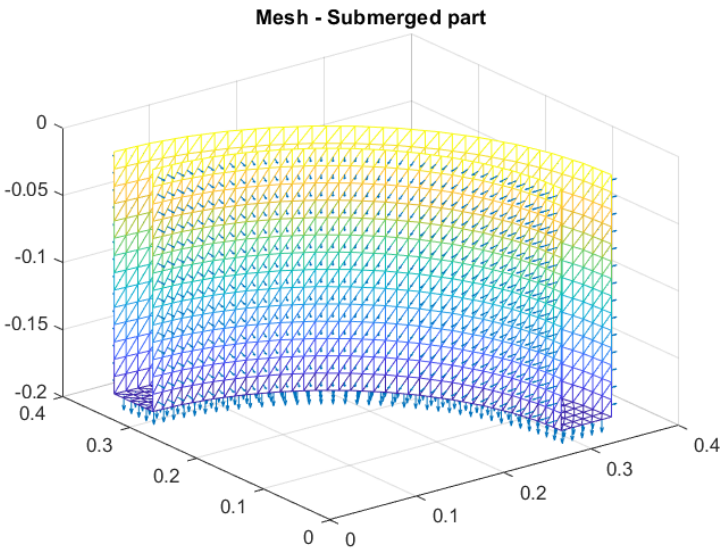

Figure 5.2: Mesh generated in Matlab with number of panels equal to 1600. Only the submerged part is meshed with a central revolution z-axis at point 0,0.

Figure 5.3 shows the results of the mesh convergence study. Figure 5.3a and Figure 5.3b show the added mass and damping in heave for the different meshes, where it can be observed that the effect of mesh size is insignificant for the sizes used here. Figure 5.3c

and Figure 5.3d shows the added mass and damping in heave for the different mesh sizes at T=0.5.

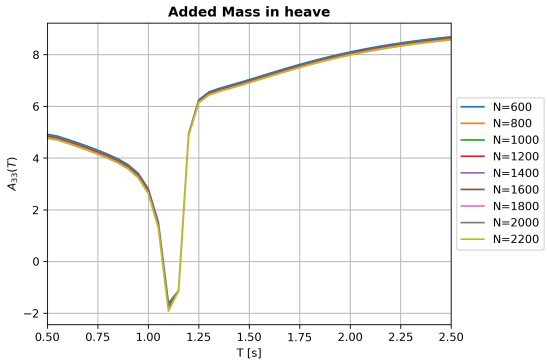

(a) A_{33} for different N.

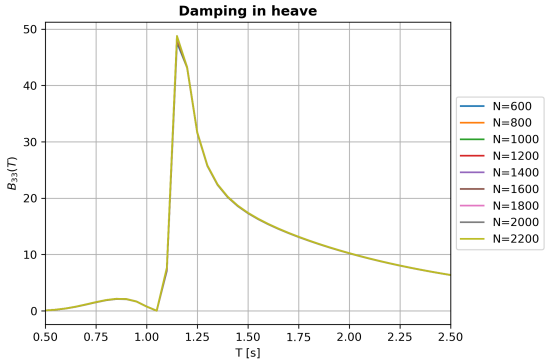

(b) B_{33} for different N.

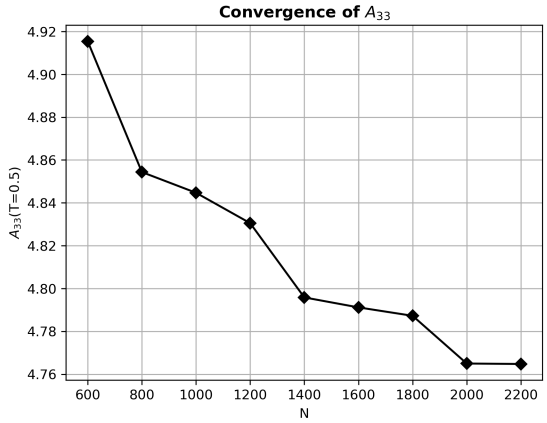

(c) A_{33}(T=0.5) for different N.

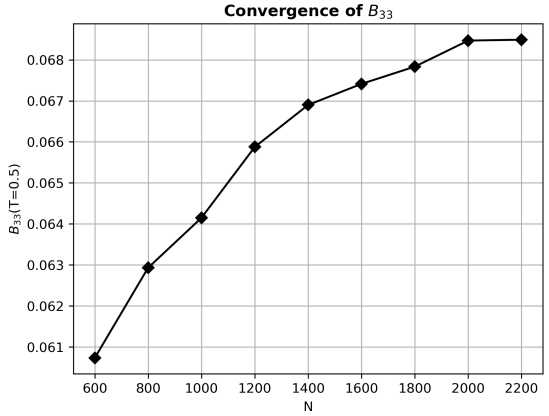

(d) B_{33}(T=0.5) for different N.

Figure 5.3: Convergence study of the WAMIT model by using the added mass and damping values as determination parameters. Plotted against wave period for all variation of N panels in a) and b) and plotted against number of panels N for T=0.5s in c) and d).

The difference in added mass between the largest and smallest panel size, is 3% which is rather small. The same calculation in added mass from the mesh size 1400 to 2200 showed a difference of less than 1% which is negligible. For that reason, and the fact that computational time increases with smaller mesh size, the number of panels equal to 1400 seems like an adequate value. For the damping however, the difference between the largest and smallest mesh size was 12% and a difference of 2.3% from mesh size 1400 to 2200. The difference between mesh size 1600 and 2200 is 1.6%. Since it is preferable to not have a finer mesh than necessary, 1600 panels will be the preferred panel size based on the results in damping. The RAOs of surge, heave and pitch have also been included in the mesh convergence study to investigate the potential difference in motion due to panel size which can be seen in Figure 5.4.

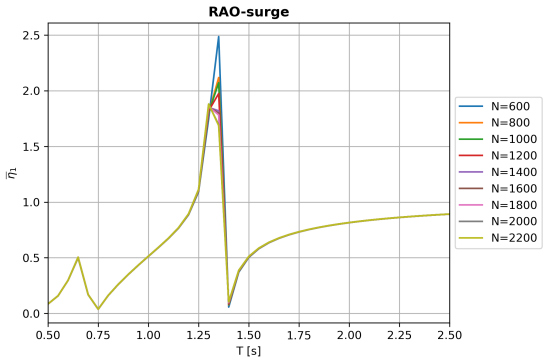

(a) Surge motion for different number of panels.

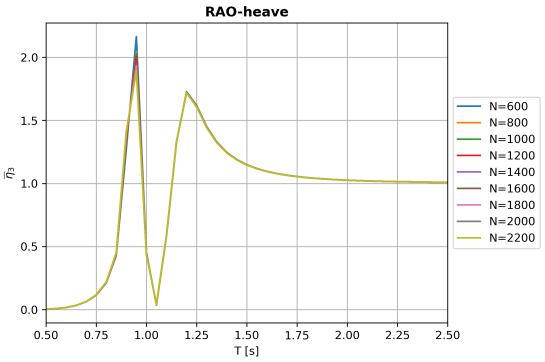

(b) Heave motion for different number of panels.

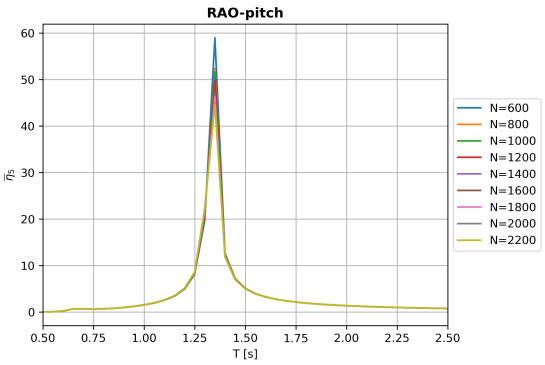

(c) Pitch motion for different number of panels.

Figure 5.4: Motion in surge (a), heave (b) and pitch (c) for different number of panels N.

As can be seen, there is little difference in motion behaviour except at resonance periods. By calculating the motion difference between the largest and smallest panel size at the first heave resonance period, the difference is equal to about 13%. This shows that the choice of panel size becomes important for the behaviour of the body, especially at resonant periods. The difference in surge and pitch was actually much greater at resonance, about 38% and 27% respectively. It is expected that the geometry used in the convergence study yields large responses at resonance due to the fact that there is little damping introduced to the system. The difference mentioned above might seem significant, but the change in motion behaves the same as for the added mass and damping. Meaning that the difference between 600 and 1200 panels is much greater than the difference between 1200 and 1800 panels and further up to 2200 panels. Since the difference in mesh size in terms of damping showed greater differences between mesh sizes compared to added mass, it has been chosen to use 1600 panels in the further simulations based on the calculation mentioned above and limits in both time and computational power.

It is important to note that the results of the added mass, damping and responses presented here are not representable as valid results other than for the mesh convergence study. The reason for this is that this study was conducted early in this thesis work where adjustments and improvements have been made along the way. The results shown in the figure of the mesh convergence study are presented as a function of wave period whereas the results are presented as a function of wave number throughout the rest of this thesis.

5.3 Additional Meshing

For configuration 7 and 8, the meshing of the model came with some extra difficulty compared to configurations 1 to 6. The vertical damper plate situated inside the moonpool made the original matlab script not directly suited for the meshing. Therefore these two configuration have been meshed in python in a modified code that allowed the inclusion of these vertical damper plates. The code has been provided by Mael Moreau, and the basis of the code is the use of symmetry and revolution. The body is divided into three parts where each of these parts are revolved around a neutral axis (x,y=0) with a certain revolution angle. The sides of the vertical damper plates have been manually added onto the revolved body with a simple square mesh grid. Special care has been taken into adding the new mesh such that the nodes and panels match the same coordinates as the revolved body. Otherwise, the free-surface panel produced by Wamit does not form a closed contour and the simulation fails to start. Figure 5.5 shows the meshed part of half the body as produced in the meshing code.

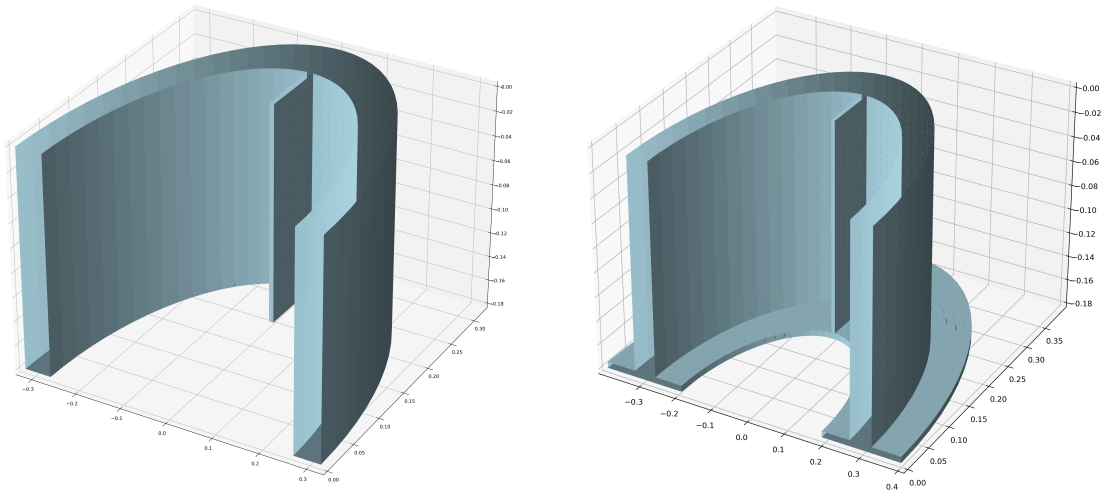

(a) Mesh of configuration 7 with N panels equal to 3360.

(b) Mesh of configuration 8 with N panels equal to 3340.

Figure 5.5: Meshed structure for configuration 7 and 8. The total amount of panels in Wamit will be twice as much as the values given in Figure 5.5a and Figure 5.5b.

The method of choosing the number of panels in this new code proved different than for the matlab code, but the same amount of panels have been aimed for. The number of panels for these configurations is however slightly higher than for the other configurations, which ultimately results in more computational time. There is a small chance that the results for configuration 7 and 8 are not completely comparable to the other configurations because of this adjusted meshing procedure. An alternative would be to produce the mesh for configuration 1 to 6 in python as well. It was assumed however that the potential discrepancies between the programs were of such small magnitude that it could be neglected. This decision was taken mainly due to the time saved in doing it this way.

Chapter 6

Results and Discussion

In this chapter the results from the numerical and experimental work are presented and discussed as well as the result for the parametric study. The numerical results will be presented first followed by the results for the parametric study and lastly the experimental results. Some results from the numerical simulation will also be included in the experimental results in order to compare more easily the similarity and differences between them. The main goal of this chapter is to elaborate and discuss the findings that have been obtained in this thesis work in order to explain the differences between all the design configurations as described in Section 4.2. A note on wave numbers used in the experimental and numerical work; a wider range of wave numbers has been used in the numerical simulation as well as finer steps compared to the wave numbers used in the experiment.

6.1 Numerical Results

The results from the numerical work are presented in terms of added mass, damping and RAOs of the rigid body motion for all design configurations. A main focus of the numerical work has been on replicate the experimental setup as closely as possible, including additional restoring effects from the mooring lines, finite water depth and channel wall effects. It has also been conducted simulations without mooring lines, channel wall effects and in infinite water depth in order to evaluate the possible difference the change in environment might have on the body. It is important to note that the numerical results presented here do not include the additional linearized damping and change in I_{55} as will be presented in Section 6.2. The reason for this is to investigate in detail the difference between the potential flow theory realm and "real" world scenarios for all configurations and also due to the fact that the parameter study was performed after the simulation work was finalized.

Figure 6.1 shows the added mass and damping coefficients for the model for the numerical replica of the experiment. The added mass and damping coefficients for the model without the additional effects from mooring lines, finite water depth and channel effects can be found in Appendix B.

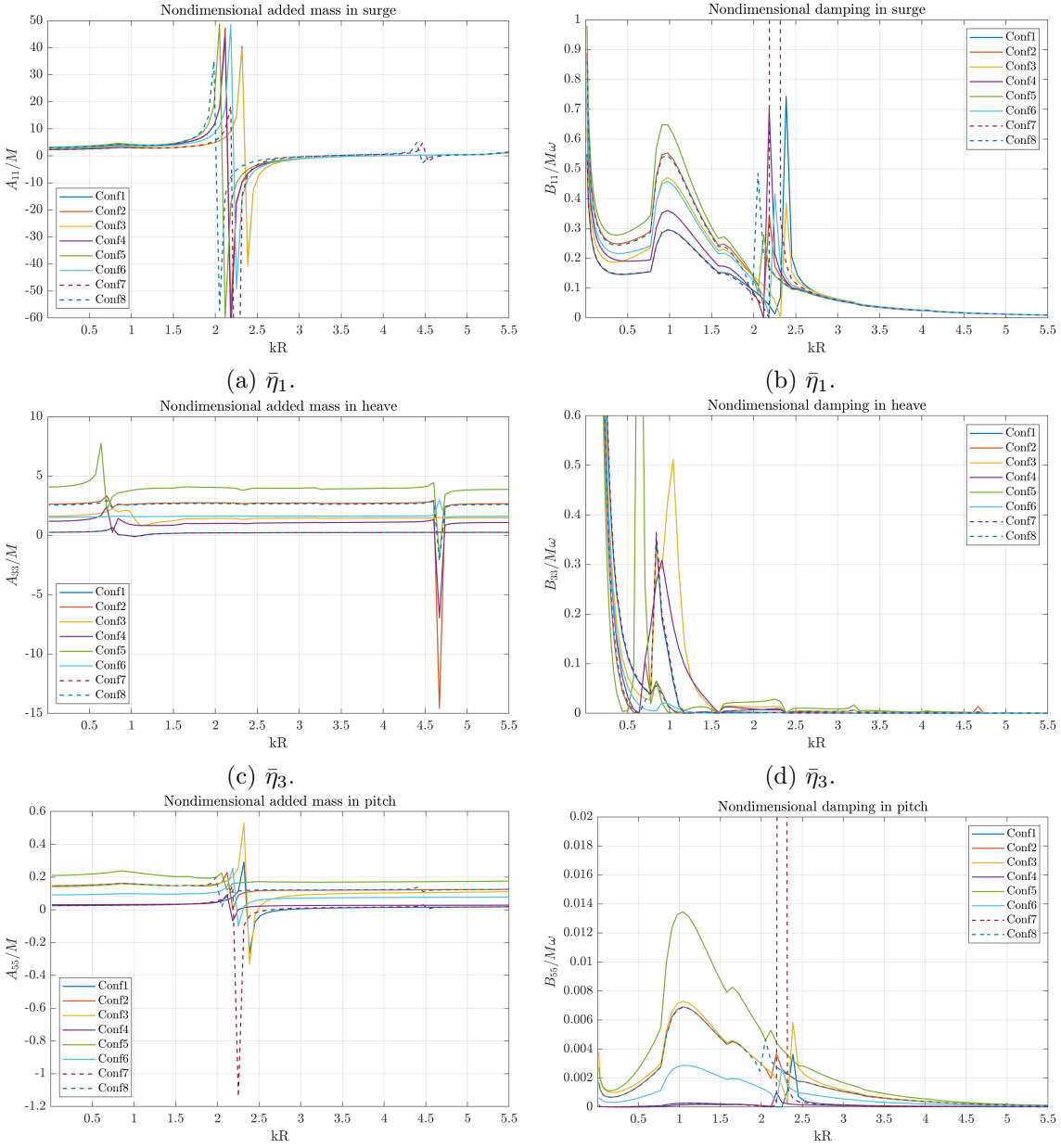

(a) $\bar{\eta}_1$. (b) $\bar{\eta}_1$.

(c) $\bar{\eta}_3$. (d) $\bar{\eta}_3$.

(e) $\bar{\eta}_5$. (f) $\bar{\eta}_5$.

Figure 6.1: Added mass and damping evaluated by Wamit.

The results in surge show that the different design configuration with regards to the horizontal damper plates produce variations in both added mass and surge, as expected. The largest values can however be seen for configuration 5, which also has the largest damper plate attached. What's interesting is the presence of the vertical damper plates which has a larger negative value than its corresponding configuration without the vertical damper plates. The vertical damper plates also introduce some more damping especially

at kR=2.1-2.5. This is also in the range where the first sloshing mode occurs. By observing the results in pitch, it is evident that coupling between surge and pitch is present since their behaviour is fairy similar with regards to where the highest and lowest values are present. The values in heave are uncoupled from pitch and surge, as is evident in the figures. The larger horizontal damper plates produce larger values in added mass due to the fact that the model needs to move more water. The same holds true for surge and pitch. A final note on the nondimensional damping in surge; for the scenario with no mooring lines present, the value goes towards zero as kR approaches zero whereas in Figure 6.1b it increases rapidly when kR approaches zero. There are no restoring effects in surge for a body that is floating freely. As soon as mooring lines are present, additional restoring forces from the mooring lines restrict the system and a natural frequency appears.

In Figure 6.2, RAO's from the numerical simulation are presented. Figure 6.2a, Figure 6.2c and Figure 6.2e are the simulations for the numerical replica whereas Figure 6.2b, Figure 6.2d and Figure 6.2f is the simulation without the additional effects present in the numerical replica. The motion in surge shows that the different design variations seem to behave similarly with some differences, especially at kR = 0.5-0.8. The approximately zero motion that can be seen at kR=2-2.5 is an interesting one. The estimate for the first sloshing mode presented in Table 4.5 seems to suggest that the sloshing resonance that occurs at kR=2.315 cancels the motion almost completely. To explain this, the added mass in surge becomes important. From Figure 6.1a, the added mass at kR=2-2.5 is a negative value which could be interpreted as a "subtraction" of mass. This is however not correct as the body still oscillates the free-surface. The physical interpretation of negative added mass can be viewed as the potential energy in the free surface being larger than the kinetic energy of the body, as outlined by Mciver and Evans (1984). This means that the occurrence of sloshing mode at kR=2-2.5 seems to contribute to produce negative added mass of the body and hence produce a cancellation effect of the motion. This cancellation effect does not come without consequence as the response increases again at kR=3 which can be explained by the increased value in added mass from kR=2 to kR=3 and also the decrease in damping coefficient in the same kR interval. The difference between the two simulations seems like the surge motion presented in Figure 6.2b is overall larger than the numerical replica. Since the numerical replica has the additional effects from mooring lines, it is expected that this will reduce the surge motion and hence explain the difference between the two different setups. The results in heave have been zoomed in in order to get a clearer picture of what is going on. The horizontal damper plates greatly shift the natural frequency from kR=1.5 for configuration 1 and 7 to kR equal to 0.5-0.75 for the configuration with varying horizontal damper plate sizes. From the piston-mode resonance estimated for configuration 1, it can be seen that the response at kR=1.2 for configuration 1 is quite small which may indicate that the piston-mode reduces the motion before the resonance period of the structure itself at kR=1.5. However, for configuration 3, where the structure has outer skirt only, the response at kR=1.2 is much larger than for configuration 1 and, since the outer skirt shift the structure's natural frequency, the piston mode does not seem to cancel the motion but rather increases it compared to configuration 1.

The response in Figure 6.2d seems to be somewhat smaller than in Figure 6.2c. The most likely reason for this is reflections from the channel walls that increases the response in the numerical replica. For the pitch motion, it can be seen that the largest response occurs within the kR range of 0.4-1 for all configurations. For configuration 2, 3, 6 and 8 it can be observed a rapid decrease in the motion between kR=0.5-0.75 whereas this behaviour is much less present for the other configurations. From the experiments, this rapid drop in response could not be observed for the pitch motion.

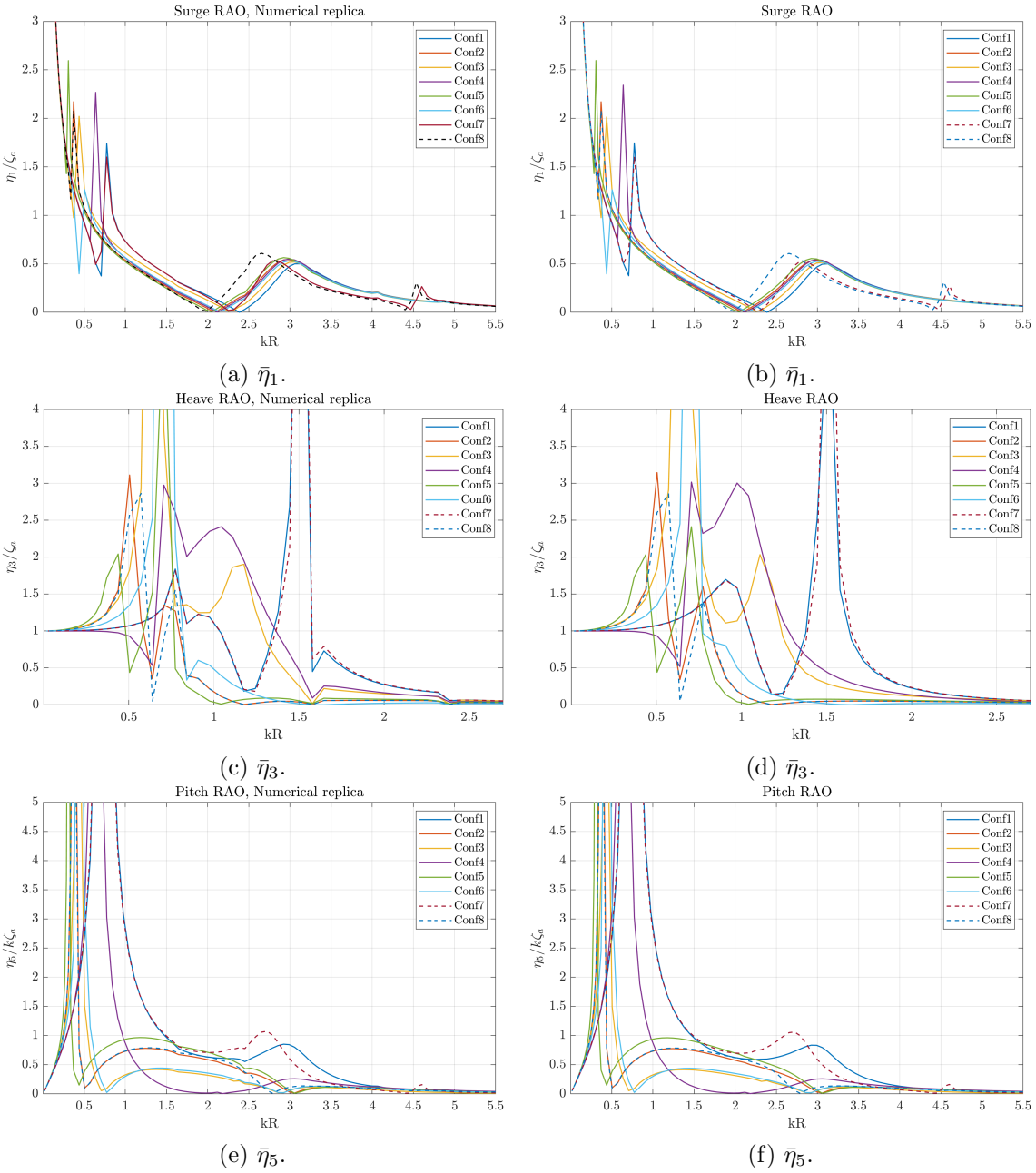

(a) $\bar{\eta}_1$. (b) $\bar{\eta}_1$.

(c) $\bar{\eta}_3$. (d) $\bar{\eta}_3$.

(e) $\bar{\eta}_5$. (f) $\bar{\eta}_5$.

Figure 6.2: RAO in surge, heave and pitch from the numerical simulation done in Wamit. a), c) and e) is a numerical replica of the experiment and b), d) and f) are simulation without channel wall effects, without the extra restoring effects from mooring lines and with infinite water depth.

6.2 Parametric Study

In this section, the results of a parameter study involving varying I_{55} and adding of additional damping in surge, heave and pitch is presented. The goal of this study is to investigate the complexity of dynamic behaviour in floating bodies and more specifically how to include viscous effects in domains that exclude viscosity. The desired output is to obtain RAO's that are more similar to the experimental results than the original numerical results. The goal however is not to produce a complete new set of RAO's to replicate the experimental results but rather an investigation on critical aspects of dynamic behaviour on two of the design configurations. The linear coefficients for added mass, damping, restoring and excitation loads obtained from the numerical analysis in Wamit have been the starting input in calculating the new RAO's. Matlab has been utilized for this study. In order to capture the coupling effects between surge and pitch, the equation of motion have been solved on the full six by six matrix form. Solving the RAO's follows the principal as described in Equation 2.15 with rearranging the variables such that it is solvable in matrix form as,

$$\frac{\eta_a}{\zeta_a} = [(\mathbf{M} + \mathbf{A}(\omega))\ddot{\eta} + \mathbf{B}(\omega)\dot{\eta} + \mathbf{C}\eta]^{-1}\mathbf{F}_{exc} \tag{6.1}$$

where the $[]^{-1}$ indicate the inverse matrix of the quantities inside the brackets. Configuration 1 and 2, as described in Chapter 4, have been utilized in this study. For comparison with the experimental results, it has been chosen to use only results with wave steepness equal to 1/100 due to time limitations. Viscous effects might also be more critical in longer waves than in shorter waves due to less wave diffraction. Since it is expected that the experimental results for wave steepness 1/30 and 1/100 yield different amplitudes in motion, it would require different values for additional damping which takes substantially more time to finalize. The first goal in this study is to ensure the matlab script solves the equation of motion correctly by comparing the results with the numerical analysis. Since the coefficients from Wamit are being utilized, the RAO's should be identical. Figure 6.3 shows this comparison in surge and pitch which indicates that the matlab script solves the equation of motion correctly. The same holds true for heave which is not shown here.

The procedure to include additional damping can be done as shown in Equation 2.20 for the linearized damping term. The term $B_{jk}^{(2)}$ have been estimated using the critical damping relation as,

$$B_{jk}^{(2)} = \left(2\sqrt{(m + A_{jk})C_{jk}}\right) x \tag{6.2}$$

where the variable x is a multiplication factor ranging from 2 to 20% of the critical damping which has been manually chosen to see if this yields reasonable estimates. The reason for using the relation for critical damping as an estimate for viscous damping, is that it yields a fairly easy estimate of what magnitude the viscous damping might be in relation to the critical damping of the system. An overview of the variable x used in estimating the

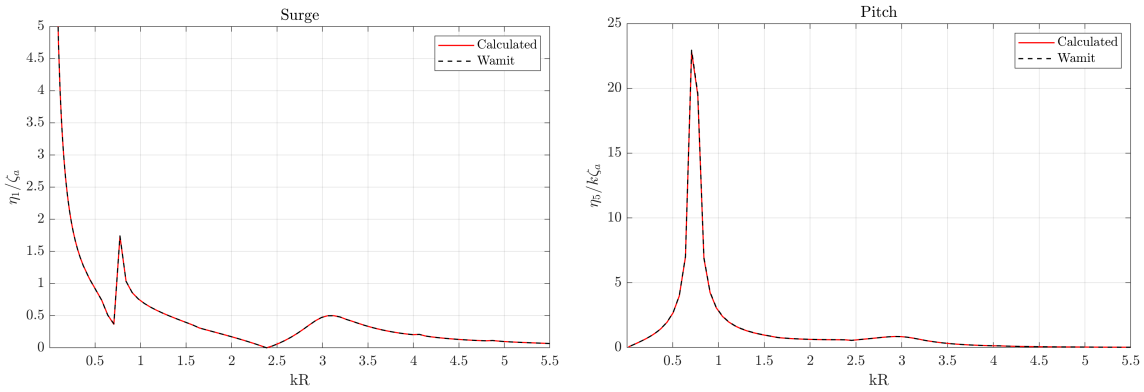

(a) Surge (b) Pitch

Figure 6.3: Comparison of the numerical RAO as evaluated by Wamit and the recalculated RAO in Matlab by using linear coefficients for added mass, damping and excitation loads obtained by Wamit in surge, heave and pitch.

additional damping for heave and pitch as well as the variation range of I_{55} can be seen in Table 6.1.

Table 6.1: Values used in the parametric study in terms of the magnitude of additional damping and I_{55}.

	Conf 1				Conf 2				
	Pitch				Pitch				I_{55}
x [%]	5	10	15	20	5	10	15	20	±10%, ±20%, ±30%
	Heave				Heave				-
x [%]	2	5	7	10	5	10	15	20	-

Since there is no restoring term in surge other than external mooring lines, there is no added damping in surge, but it is expected that the additional damping in pitch will influence the surge motion due to strong coupling.

Figure 6.4 shows the results for all damping values in heave with the original RAO from Wamit shown in black. Since the heave motion is uncoupled from surge and pitch, no influence from either the damping in pitch or change in I_{55} was seen as expected. From the figure, it seems like an additional 5% damping fits the experimental data the best. It also seems that only adding an additional damping coefficient and no viscous excitation loads seem to fit the experimental data fairly well.

Figure 6.5 shows two cases where the best results for surge are shown in Figure 6.5a and the corresponding results in pitch in Figure 6.5b. Figure 6.5d shows the best result in pitch and Figure 6.5c shows the corresponding results in surge. The original RAO from Wamit is shown in black for all figures. It has been chosen to only include the results here that show best fit to the experimental data. The total result of all the damping coefficients and variation in I_{55} can be found in Appendix D.

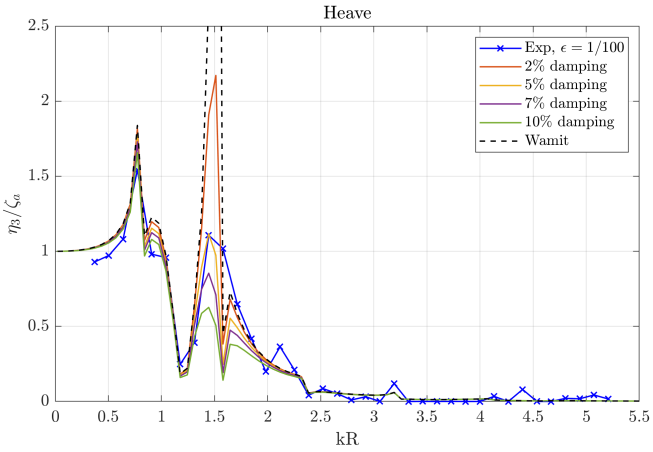

Figure 6.4: Viscous damping study on the heave motion for configuration 1 with the original RAO from Wamit shown in black.

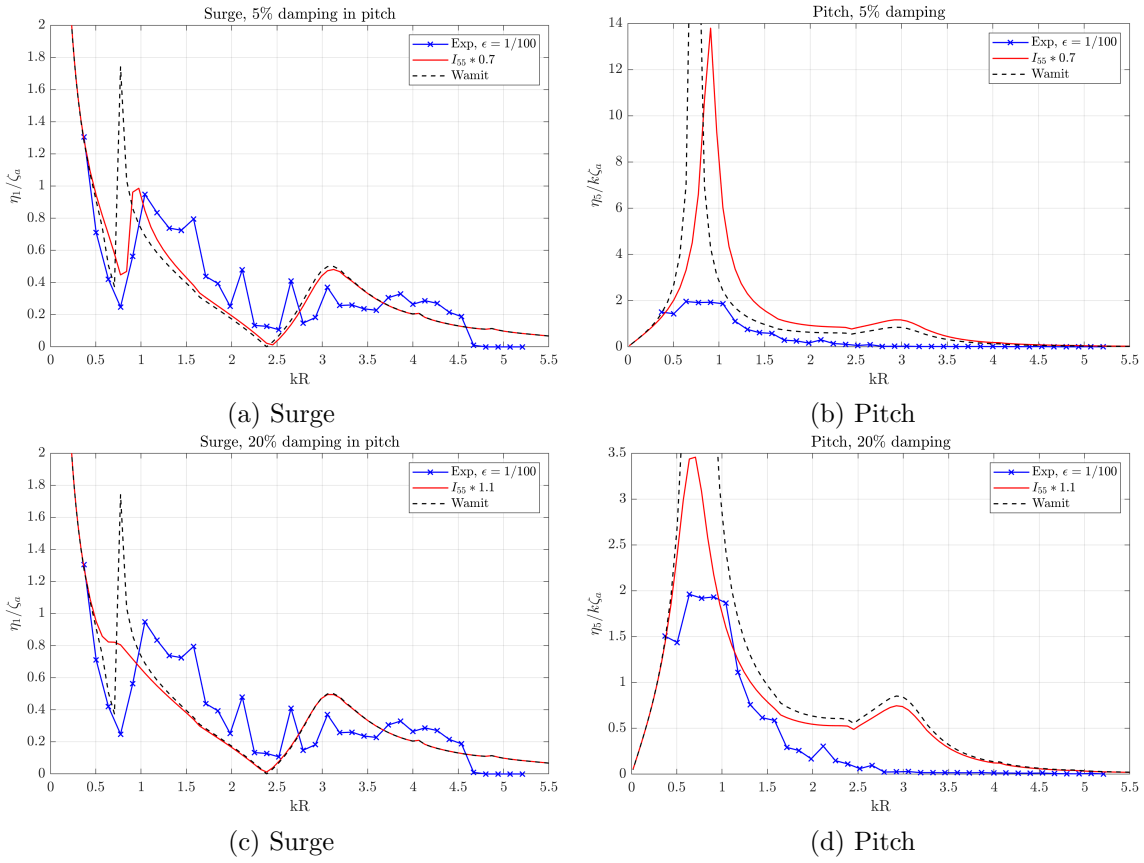

(a) Surge (b) Pitch

(c) Surge (d) Pitch

Figure 6.5: Two cases from the viscous damping study in surge and pitch for configuration 1 with the original RAO from Wamit shown in black.

For the surge motion, it seems like an additional 5% damping in pitch and with $I_{55} \cdot 0.7$ fit the experimental data best with a corresponding pitch motion that does not fit very well. Using $I_{55} \cdot 0.7$ and 20% additional damping in pitch, yielded the best fit for the pitch motion whereas the surge motion then does not fit as well. Even though these estimations give a rough approximation on viscous damping, the results indicate that viscous excitation may be a significant contributor to the motion. Figure 6.6 shows the results for the same study in heave for configuration 2. With the inclusion of horizontal damper plates, the

needed additional damping in heave was higher than for configuration 1. Even though the results do not fit the experimental data as nicely as configuration 1, it seems that an additional 20% damping yields the best fit. The results may indicate that viscous excitation is significant for the heave motion at resonance.

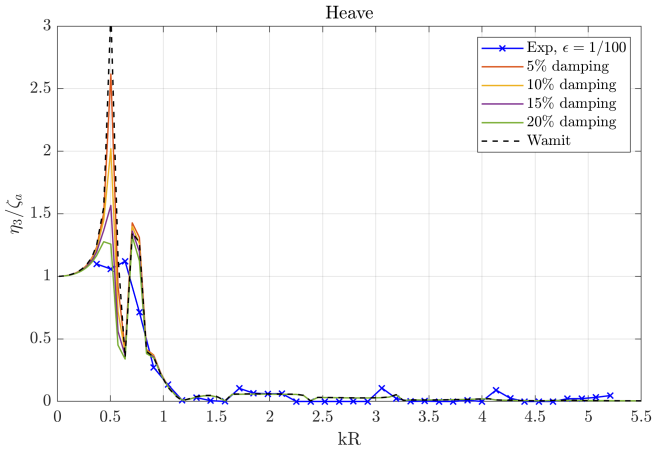

Figure 6.6: Viscous damping study on the heave motion for configuration 2 with the original RAO from Wamit in black.

Figure 6.7 shows the results in surge and pitch for the best case. For this design configuration, the surge motion was very little affected by additional damping as can be seen in Appendix D. Therefore, only one case is shown here where the pitch motion seems to fit the best. It also seem like for this configuration, $I_{55} \cdot 0.7$ yields the best fit with 20% additional damping in pitch. With horizontal damper plates, it seem like the effect if viscous damping is greater than without these damper plates as the pitch motion fit the resonance peak better for configuration 2 than for configuration 1 with the same damping coefficient. It is interesting to see that the surge motion was less affected by additional damping in pitch for configuration 2 than for configuration 1. Evidently viscous excitation plays a significant role in both design configurations as the results generally do not fit the experimental data completely.

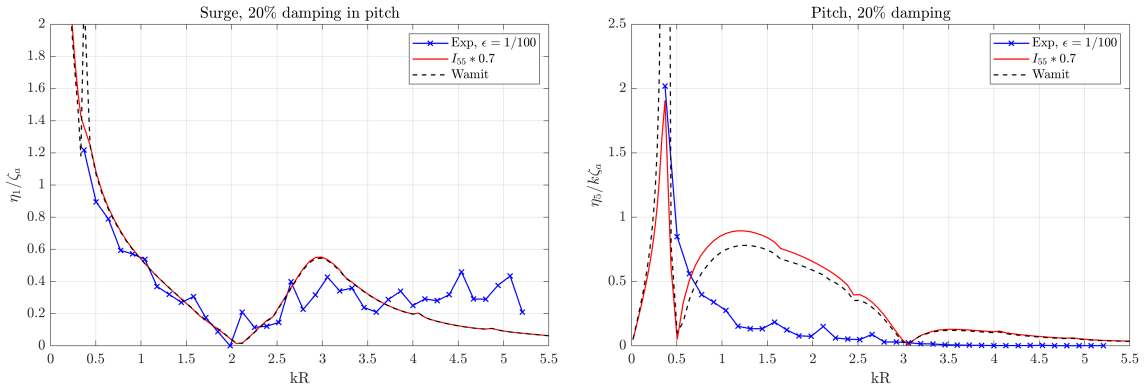

(a) Surge (b) Pitch

Figure 6.7: Viscous damping study in surge and pitch for configuration 2 with the original RAO from Wamit in black.

6.3 Experimental Results

The following pages shows the main results from the experiments in terms of RAO in surge, heave and pitch, alongside with the numerical replica. The results are presented with each degree of freedom on three separate pages for all configurations for closer evaluation of the differences in the design. Further, closer comparisons between configuration 1 and 7, as well as configuration 2 and 8, are presented separately with the main goal to evaluate in detail the effect of the vertical damper plates. Furthermore, a closer comparison between all the horizontal damper plates is presented, meaning configuration 2 to 6, and lastly free surface elevation inside the moonpool is presented to evaluate the influence the vertical damper plates has on the free-surface.

Figure 6.8 shows the response in surge for all configurations and it can be observed that the response behaviour is fairly similar for all configurations. The model experiences a cancellation effect ranging between kR=2-2.5 for the different configurations due to the first sloshing mode estimated for configuration to be at kR=2.315. It does not seem that the horizontal damper plates change the amplitude of the response that much. They seem to shift the cancellation period which means that the damper plates influence the sloshing that occurs. Results for ϵ=1/100 yield the largest response, which is due to viscous effects. As the waves becomes longer, they behave in a more regular fashion with less disturbances or wave breaking. Meaning that vortex shedding that occur on the model as the water passes around it happens further downstream on the model. This means an increase in drag loads which should explain the difference between the wave steepness's. There is however a peculiar peak at kR=2.6 which is present in all configurations. Now, this peak seems to be slightly lower in configuration 1, 3 and 7, as can be seen in Figure 6.8a, Figure 6.8c and Figure 6.8g, respectively. These are configuration that do not have inner skirts which may indicate that the sloshing motion inside the moonpool is larger with the presence of inner skirts. This might make sense as the water inside the moonpool gets more restricted in where it can move with these skirts present. The Wamit results shown in black fit the experimental results fairly well other that at resonant frequencies. A potential solver like Wamit tends to overestimate the motion at resonance due to the fact that it does not include viscous effects. It can therefore be assumed that where Wamit overestimate the motion, viscous effects are of significant importance. For configuration 1 and 7, Wamit also does not hit exactly the peaks that occur at kR=1 which is likely to be the inertial term I_{55} in pitch that is not equal to that in the model which has been discussed in the parameter study. Since the surge and pitch motion are strongly coupled, the same behaviour can be seen in pitch for configuration 1 and 7 as can be seen in Figure 6.10a and Figure 6.10g respectively. The motion in surge and pitch can therefore not be evaluated separately as they will influence each other.

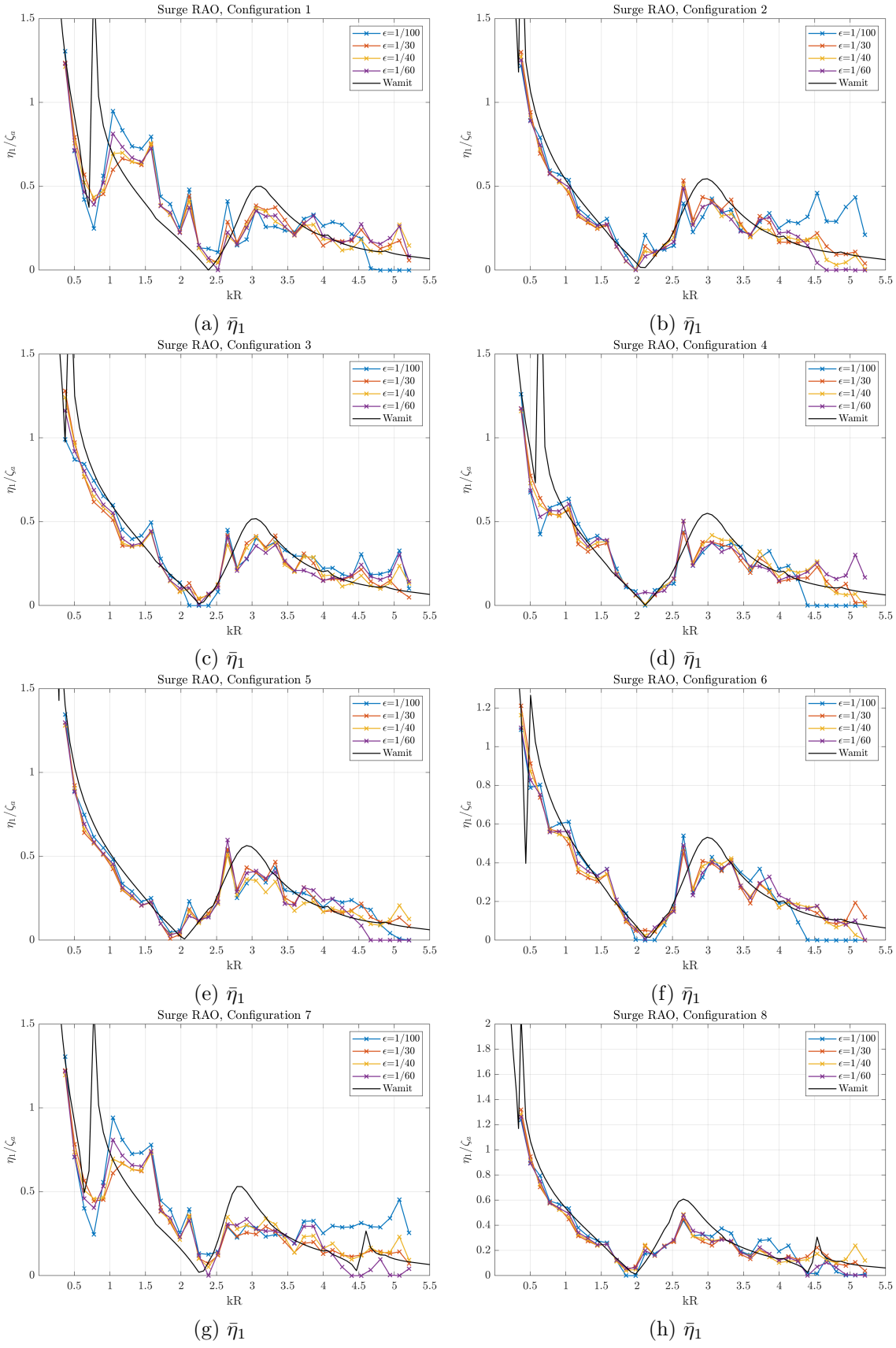

(a) $\bar{\eta}_1$ (b) $\bar{\eta}_1$ (c) $\bar{\eta}_1$ (d) $\bar{\eta}_1$ (e) $\bar{\eta}_1$ (f) $\bar{\eta}_1$ (g) $\bar{\eta}_1$ (h) $\bar{\eta}_1$

Figure 6.8: RAO in surge for all configurations at four different wave steepnesses, ϵ, including the numerical replica simulation from Wamit shown in black.

Figure 6.9 shows the response in heave for all configurations. Heave is uncoupled from surge and pitch and can be treated separately. At first glance, the response seems to change more for the different configurations than for the surge motion. A reason for this is that the natural heave frequency of the structure lies within the range of the tested wavenumbers. As can also be seen, especially for configurations 1 and 2 in Figure 6.9a and Figure 6.9b, the natural frequency changes substantially with presence of inner and outer skirts. This also varies with the varying sizes of the horizontal damper plates. The Wamit results also correlate nicely with the experimental results, other than for the magnitude at the resonance frequency. Since they coincide fairly well, the explanation with regards to the piston-mode resonance given in Section 6.1 holds true for the experimental results. However, the same two peaks can not be seen in the experimental results for configurations with both inner and outer skirts. A hint of this behaviour can be seen for wave steepness 1/100, although the peaks in the numerical result do not coincide perfectly with the minimal double peaks observed in the experiment. It is therefore likely that the vortices that are being shed from the skirts completely eradicate the presence of two peaks in the RAO as estimated by Wamit. Another possible explanation is that in the numerical simulation, the range of wavenumber was used with a finer interval than in the experiment. It can therefore be possible that the wavenumbers used in the experiments do not excite the resonant frequency entirely. The most likely cause is however the significant viscous effects caused by the skirts.

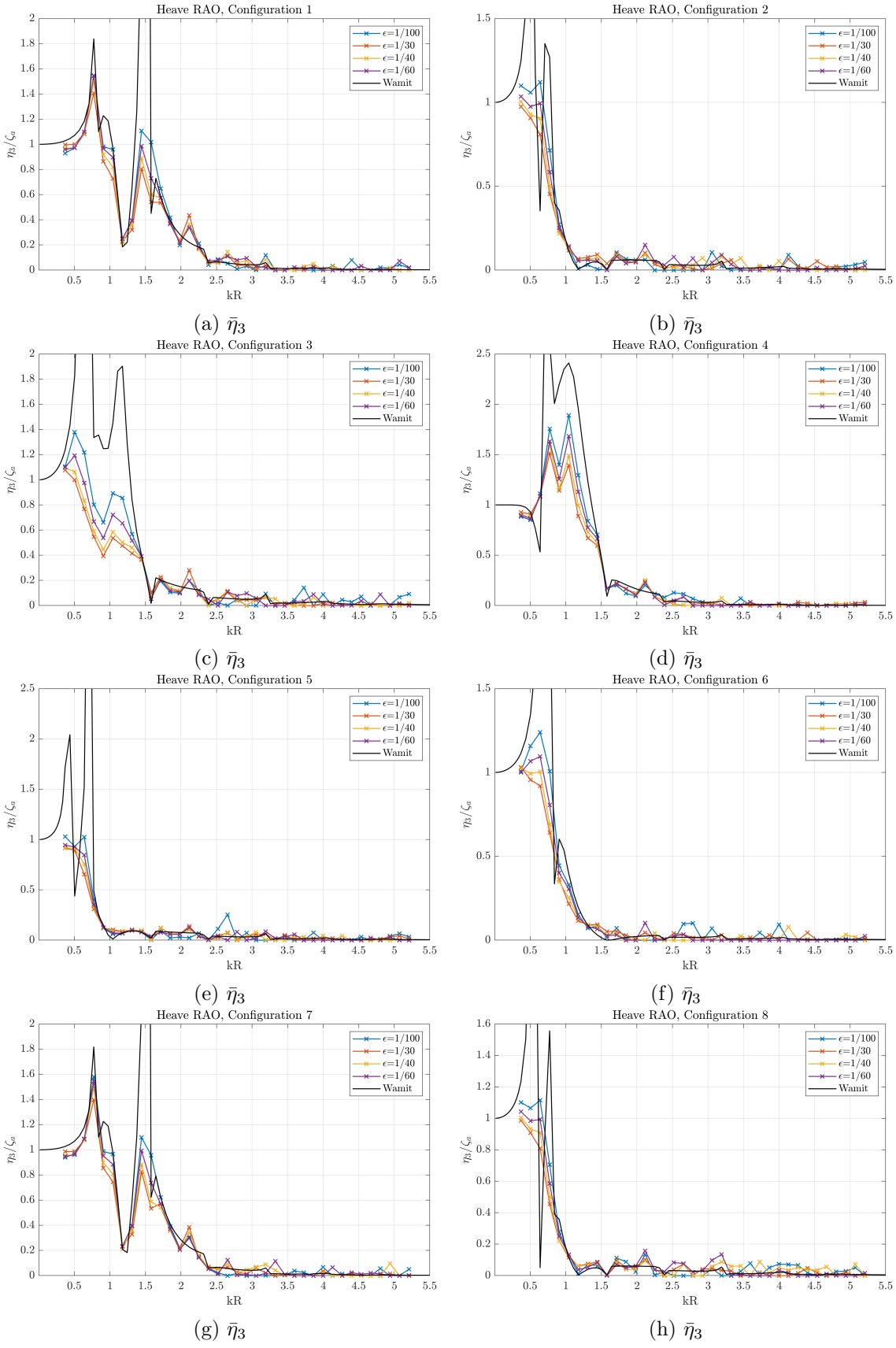

(a) $\bar{\eta}_3$ (b) $\bar{\eta}_3$ (c) $\bar{\eta}_3$ (d) $\bar{\eta}_3$ (e) $\bar{\eta}_3$ (f) $\bar{\eta}_3$ (g) $\bar{\eta}_3$ (h) $\bar{\eta}_3$

Figure 6.9: RAO in heave for all configurations at four different wave steepness, ϵ, including the numerical replica simulation from Wamit shown in black.

Figure 6.10 shows the pitch motion for all configurations. The experimental and numerical results show the largest discrepancy in pitch indicating several things. Viscous damping and excitation seem to be important which Wamit does not capture. The inertial term I_{55} is also a factor that will influence the motion. As previously discussed, this term is difficult to obtain a correct solution for. Wamit does however hit the resonance frequency which indicates that I_{55} cannot be too far off. The most likely cause for the discrepancy is as just mentioned, viscous damping and viscous excitation. Configurations 2, 3, 5, 6 and 8 are very similar in the response behaviour, except for the magnitude. Where the numerical simulation underestimate the response, viscous excitation becomes prominent and where the numerical overestimates, viscous damping becomes prominent. It seems that configuration 5 as can be seen in Figure 6.10e, yields the lowest response at the lowest kR number. This configuration has the largest value for the inner and outer skirts. This means that the skirts produce a larger value in added mass, as more water needs to be pushed away as the model pitches and, more importantly, larger damping. By looking at the smallest kR number for configuration 6 in Figure 6.10f, the response for ϵ=1/100 increases to around 2.2 as compared to 1.4 for configuration 5 in Figure 6.10e. The horizontal skirts also offer a pitch restoring moment as the skirts on opposite side of the model each yield a pitch moment which acts in opposite direction of each other when the model pitches. There is a fine line to tread here since larger skirts also yield larger excitation forces due to the fact that the water can act on a larger surface which can lead to larger responses. It appears that might be the case between kR=0.5-2 compared to configuration 6. It does however seem like configuration 5 is the best choice for the pitch motion specifically at the lower end of kR but as it unfortunately yields larger response between kR=1-2 compared to configuration 6, no unambiguous conclusion can be drawn.

As can be seen in Figure 6.10e, the Wamit result do not seem to match the natural frequency of the experimental results. At first glance it may look like a larger discrepancy between the numerical and experimental results. By using the values provided by Wamit, the analytical estimate shows that the natural frequency does not lie in the kR range for which the experimental results are presented. Wamit tends to overestimate the response at resonance, but since the resonance area is outside the experimental range, viscous excitation becomes prominent here. By observing the largest experimental response and the corresponding numerical result marked with a red dot, it underlines that viscous excitation is significant at least for this specific kR number. For the other configurations, it is clear that viscous damping due to flow separation is crucial at resonance, but the contribution of viscous excitation becomes much clearer for configuration 5.

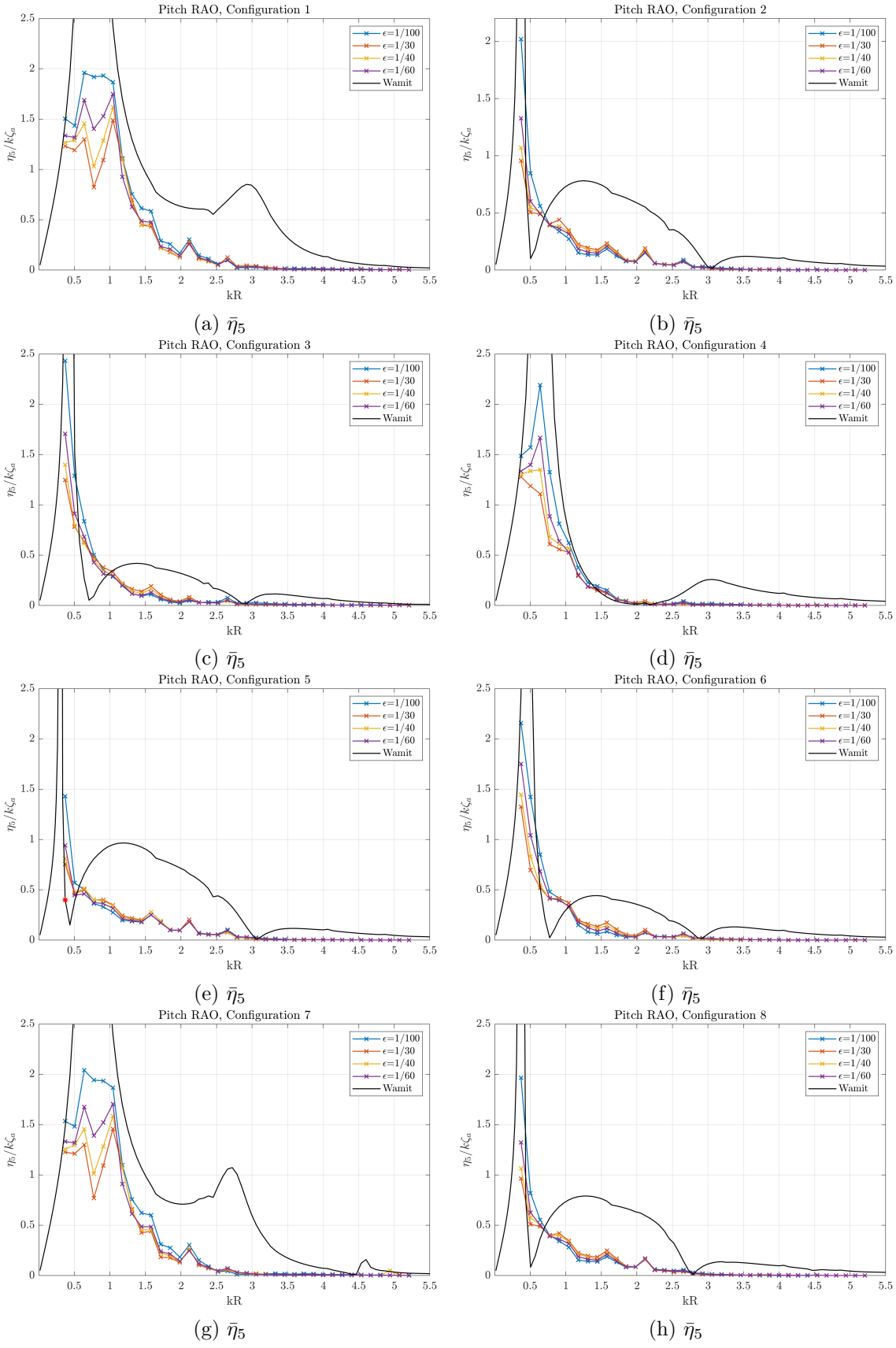

(a) $\bar{\eta}_5$ (b) $\bar{\eta}_5$

(c) $\bar{\eta}_5$ (d) $\bar{\eta}_5$

(e) $\bar{\eta}_5$ (f) $\bar{\eta}_5$

(g) $\bar{\eta}_5$ (h) $\bar{\eta}_5$

Figure 6.10: RAO in pitch for all configurations at four different wave steepness, ϵ, including the numerical replica simulation from Wamit shown in black.

Figure 6.11 shows the RAO for configuration 1 and 7 where the figures on the left-hand side show the motion with wave steepness equal to 1/30 and the figures on the right-hand side with wave steepness equal to 1/100. It can be seen from the figure that the vertical damper plates produce almost no change for the heave and pitch motion. The biggest difference can be seen for the surge motion.

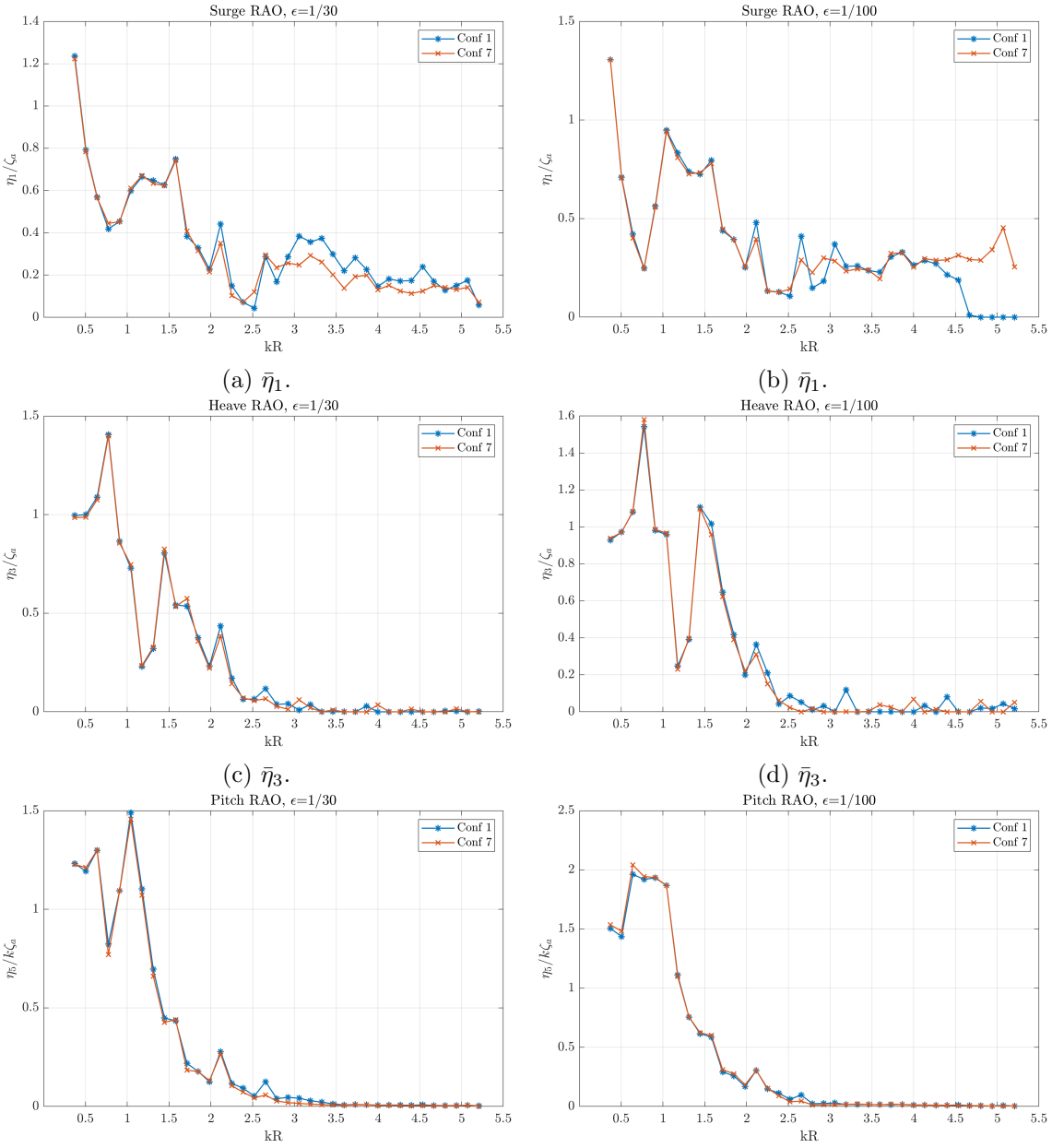

(a) $\bar{\eta}_1$. (b) $\bar{\eta}_1$.

(c) $\bar{\eta}_3$. (d) $\bar{\eta}_3$.

(e) $\bar{\eta}_5$. (f) $\bar{\eta}_5$.

Figure 6.11: RAO in surge, heave and pitch for configuration 1 and 7 for wave steepness 1/30 and 1/100 showing in detail the more or less negligible effect from the vertical damper plates.

Figure 6.12 shows the RAO for configuration 2 and 8 where the figures on the left-hand side show the motion with wave steepness equal to 1/30 and the figures on the right-hand side with wave steepness equal to 1/100. It can be seen from the figure that the results show the same trend as for configuration 1 and 7 shown on the previous page.

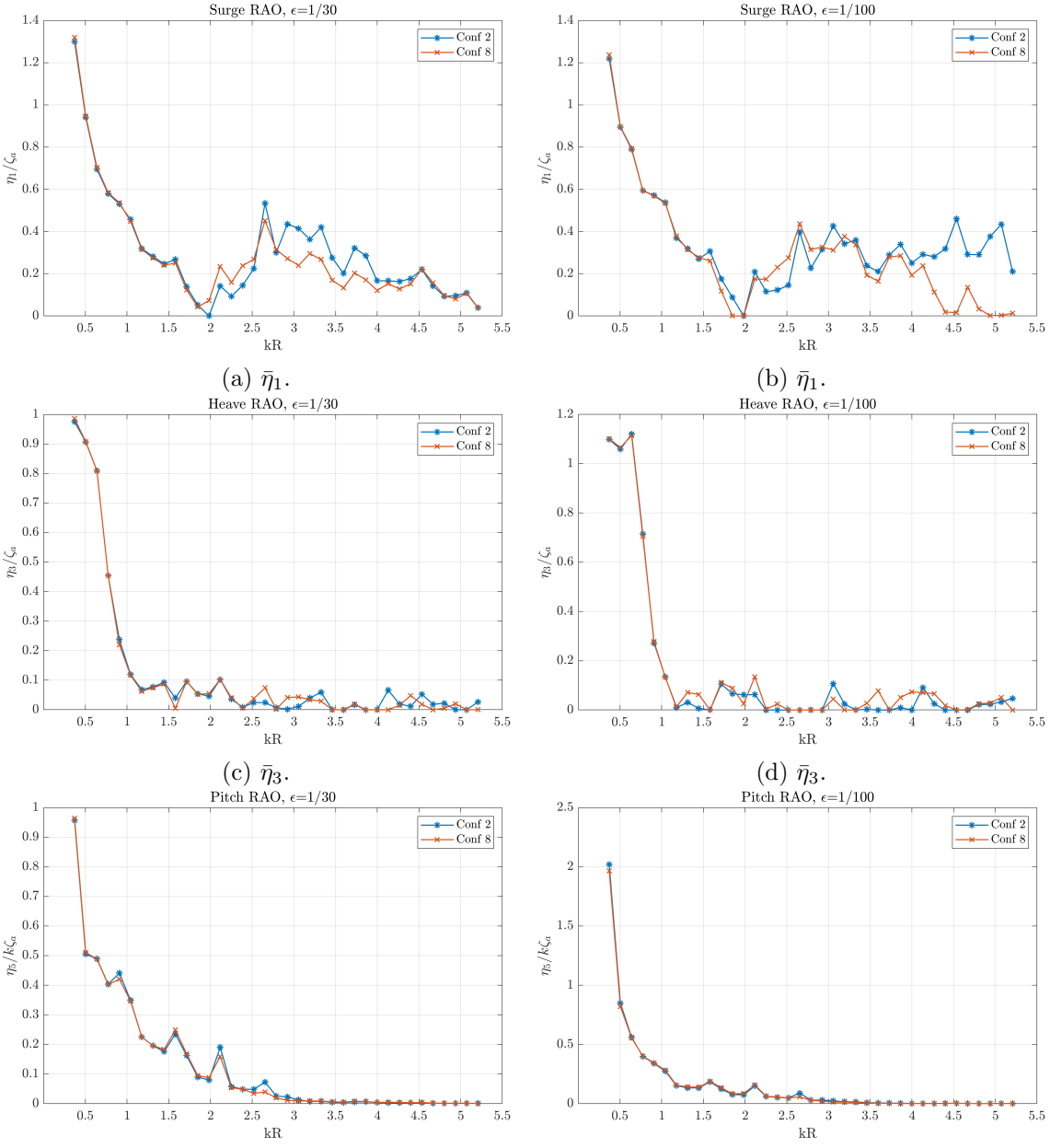

(a) $\bar{\eta}_1$. (b) $\bar{\eta}_1$.

(c) $\bar{\eta}_3$. (d) $\bar{\eta}_3$.

(e) $\bar{\eta}_5$. (f) $\bar{\eta}_5$.

Figure 6.12: RAO in surge, heave and pitch for configuration 2 and 8 for wave steepness 1/30 and 1/100 showing in detail the more or less negligible effect from the vertical damper plates.

The initial idea for the vertical damper plates was to investigate if they would influence the sloshing motion in a beneficial way. Both Figure 6.11 and Figure 6.12 indicate very little to no improvement on the motion with these vertical damper plates included. They show a negligible effect in heave and pitch with only noticeable effects in surge. In Figure 6.11 it

seem that the plates have a small beneficial effect for ϵ=1/30 whereas the same cannot be said for ϵ=1/100. During the tests it could be observed that the vertical plates produced more disturbance of the water inside the moonpool that behaved in a very non-linear way as shown in Figure 6.13. The same behaviour of the free surface inside the moonpool could not be observed for configuration 1. In Figure 6.12, the vertical plate seems to be a bit more beneficial for the surge motion. For kR=2.5-5, the plate shows a positive influence on the motion indicating that it yields reduction in the motion for higher frequencies. The results do not indicate however that this is a design feature that ought to be implemented as the effects in surge, heave and pitch are almost negligible, so that it is unnecessary to include these specific plates. It does however indicate an interest for further investigation on this idea since only one type of vertical plate has been tested. Varying the dimension, perforation ratio or even the placements of the plates, could give a better understanding and conclusion if a such design feature is beneficial for this kind of structure.

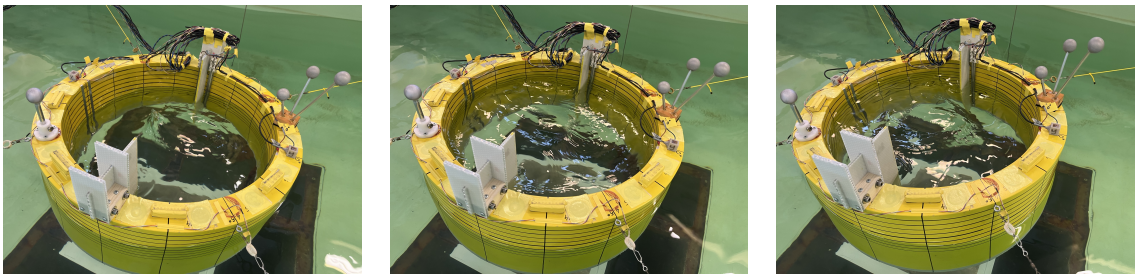

(a) Time instance 1 (b) Time instance 2 (c) Time instance 3

Figure 6.13: Snapshots of configuration 7 showing the free-surface disturbance inside the moonpool due to the vertical damper plates.

Figure 6.14 shows configuration 2 to 6 for ϵ=1/30 to the left and ϵ=1/100 to the right with the aim to see more clearly the difference between the different horizontal damper plates. Results for ϵ=1/40 and ϵ=1/60 can be seen in Appendix A. For the surge motion, the differences between them becomes larger at wave steepness 1/100, whereas they are more consistent at wave steepness 1/30. It also seem that configuration 5, shows a somewhat lower response at least between kR=0.5-2 and also between kR=3.5-5 for wave steepness 1/100. For the heave motion, configuration 4 stands out to be the worst plate configuration as it shows the largest response over a larger span of kR numbers.

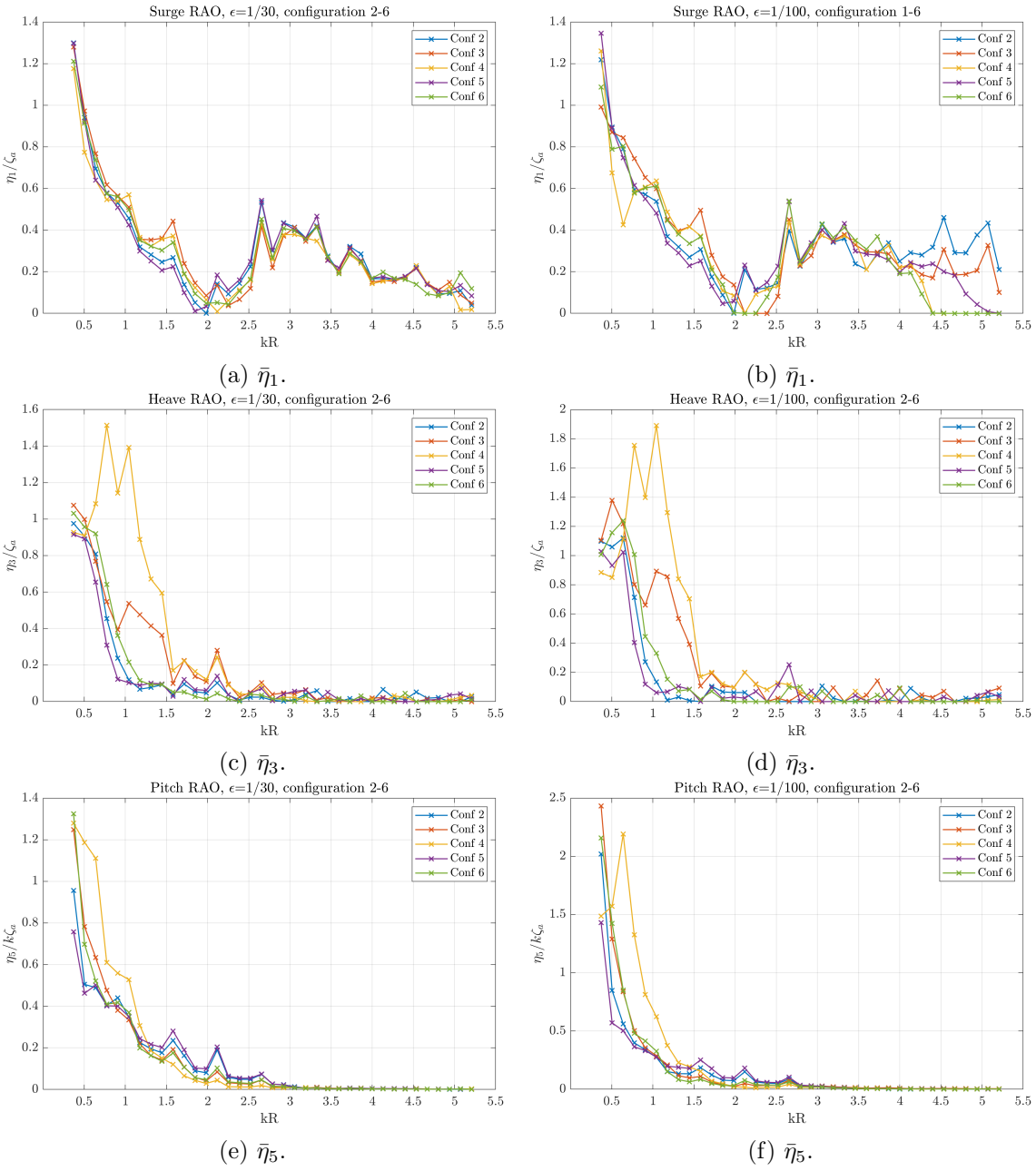

(a) $\bar{\eta}_1$. (b) $\bar{\eta}_1$.

(c) $\bar{\eta}_3$. (d) $\bar{\eta}_3$.

(e) $\bar{\eta}_5$. (f) $\bar{\eta}_5$.

Figure 6.14: RAO in surge, heave and pitch for configuration 2 to 6 for wave steepness 1/30 and 1/100.

During the test of configuration 4, some interesting effects could be observed as shown in Figure 6.15. The behaviour of this sloshing effect is highly non-linear and is beyond the scope of this work to discuss in a professional manner. It was however interesting that this effect could be observed and captured during the experiments.

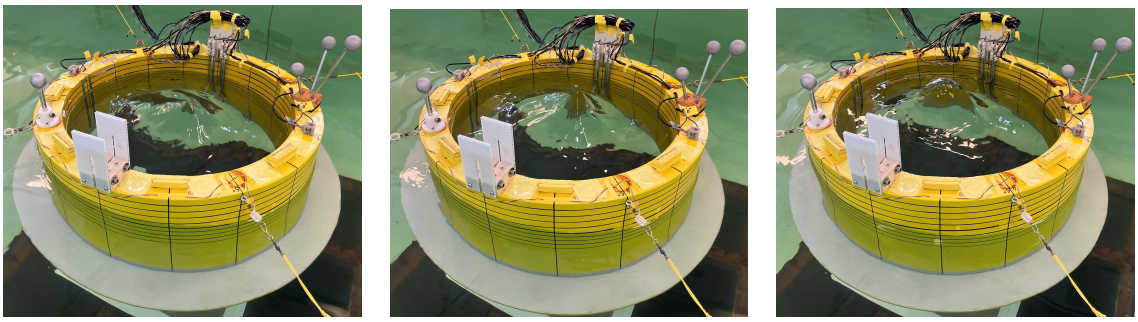

(a) Time instance 1 (b) Time instance 2 (c) Time instance 3

Figure 6.15: Snapshots of configuration 4 showing the free-surface disturbance inside the moonpool.

The last results that are presented are for the free-surface elevation inside the moonpool for wave steepness 1/30. Results for wave steepness 1/100, 1/60 and 1/40 can be found in Appendix C. The model was fitted with wave probes at three different locations inside the moonpool in order to evaluate sloshing and piston-mode. It also becomes clearer how the vertical damper plates influence the free-surface. Figure 6.16 shows the free-surface elevation in the earth fixed coordinate system. Figure 6.16a and Figure 6.16b shows the surface elevation for all configurations at zero and 180°, respectively. Figure 6.16c and Figure 6.16d show a closer comparison between configuration 1 and 7 with regards to the vertical damper plates. Figure 6.16e and Figure 6.16f show the same comparison for configuration 2 and 8.

From Figure 6.16a and Figure 6.16b it can be seen that configuration 1 appears to yield the largest response in surface elevation inside the moonpool. Configuration with both inner and outer skirts show very similar results. The influence the vertical damper plates have on the free surface becomes prominent here. It can be seen that for configuration 7 and 8, there is a significantly higher motion of the surface at kR=4.5 than for configuration 1 and 2. From the RAO's shown earlier, this increased motion does not seem to produce higher response of the body at this specific kR number. An interesting observation can be made for the peaks at kR=2.2 and kR=2.6 approximately in Figure 6.16c. These peaks can also be observed in the surge and pitch motion for configuration 1 as previously shown in Figure 6.11a and Figure 6.11e. From the results at the wave probe located at 270°, the plates significantly increase the free-surface elevation at approximately kR=2 towards kR=5 for both configuration 7 and 8 as shown in Figure 6.16d and Figure 6.16f respectively.

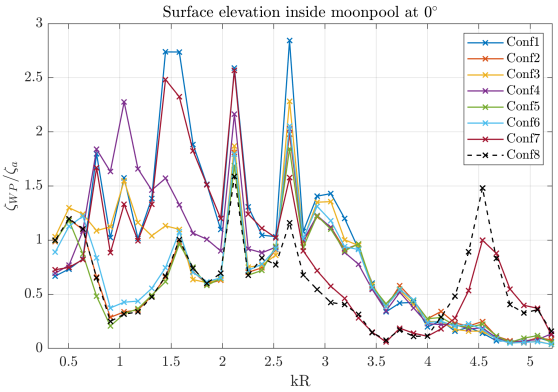

(a) Configuration 1-8.

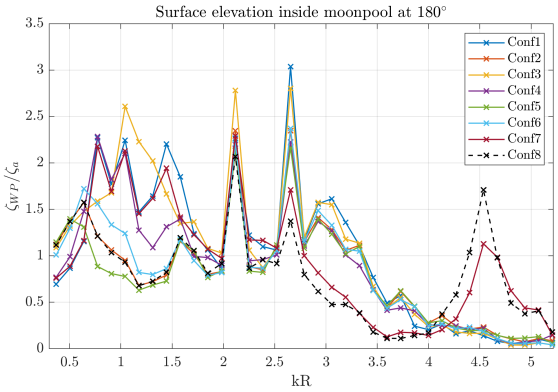

(b) Configuration 1-8.

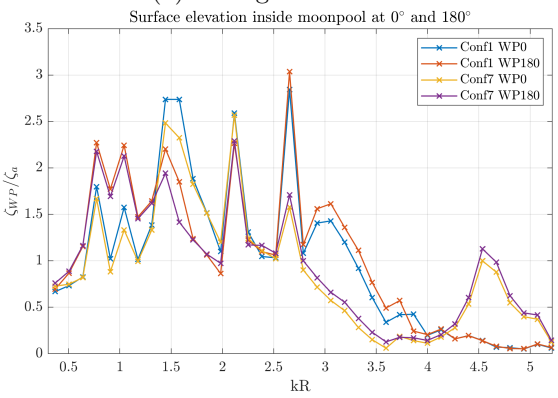

(c) Configuration 1 and 7.

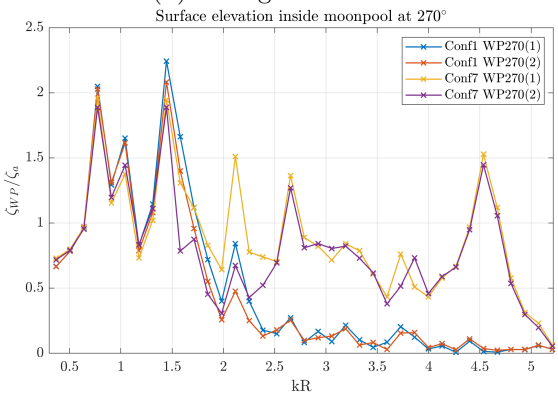

(d) Configuration 1 and 7.

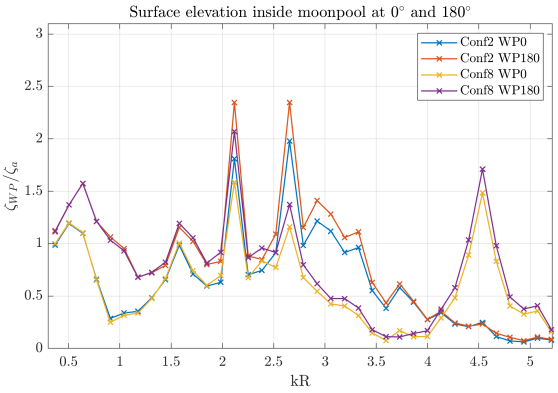

(e) Configuration 2 and 8.

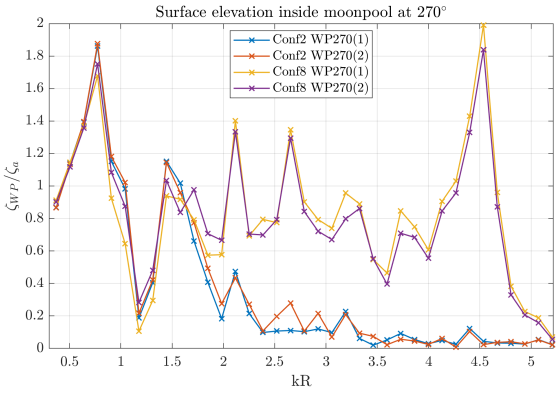

(f) Configuration 2 and 8.

Figure 6.16: Free surface elevation inside moonpool for all configurations at 0° and 180° in a) and b) respectively. A detailed comparison at 0, 180 and 270° between configuration 1 and 7 in c) and d) and between configuration 2 and 8 in e) and f).

During the experiments, the piston-mode behaviour could be observed and Figure 6.17 shows snapshots of configuration 1 where this could be observed more easily. It is difficult to isolate piston-mode behaviour from the free-surface elevation results in Figure 6.16 as sloshing in greater or lesser form occur. The piston-mode resonance can however be observed at approximately kR=1.4 in Figure 6.17c and Figure 6.17d as the values for surface-elevation at 0°, 180° and both wave probes at 270° are fairly similar indicating a more vertical elevation of the free-surface. This is also in the kR range where piston-mode resonance frequency were estimated to be. Since the natural frequency of configuration 1 is in the range of kR=1.5, it is likely that the piston-mode is excited by the natural

frequency of the structure. The free-surface elevation peak observed in Figure 6.16c at kR=2.2 may also indicate piston mode behavior as this peak could also be seen for the heave RAO at configuration 1 shown in Figure 6.9a.

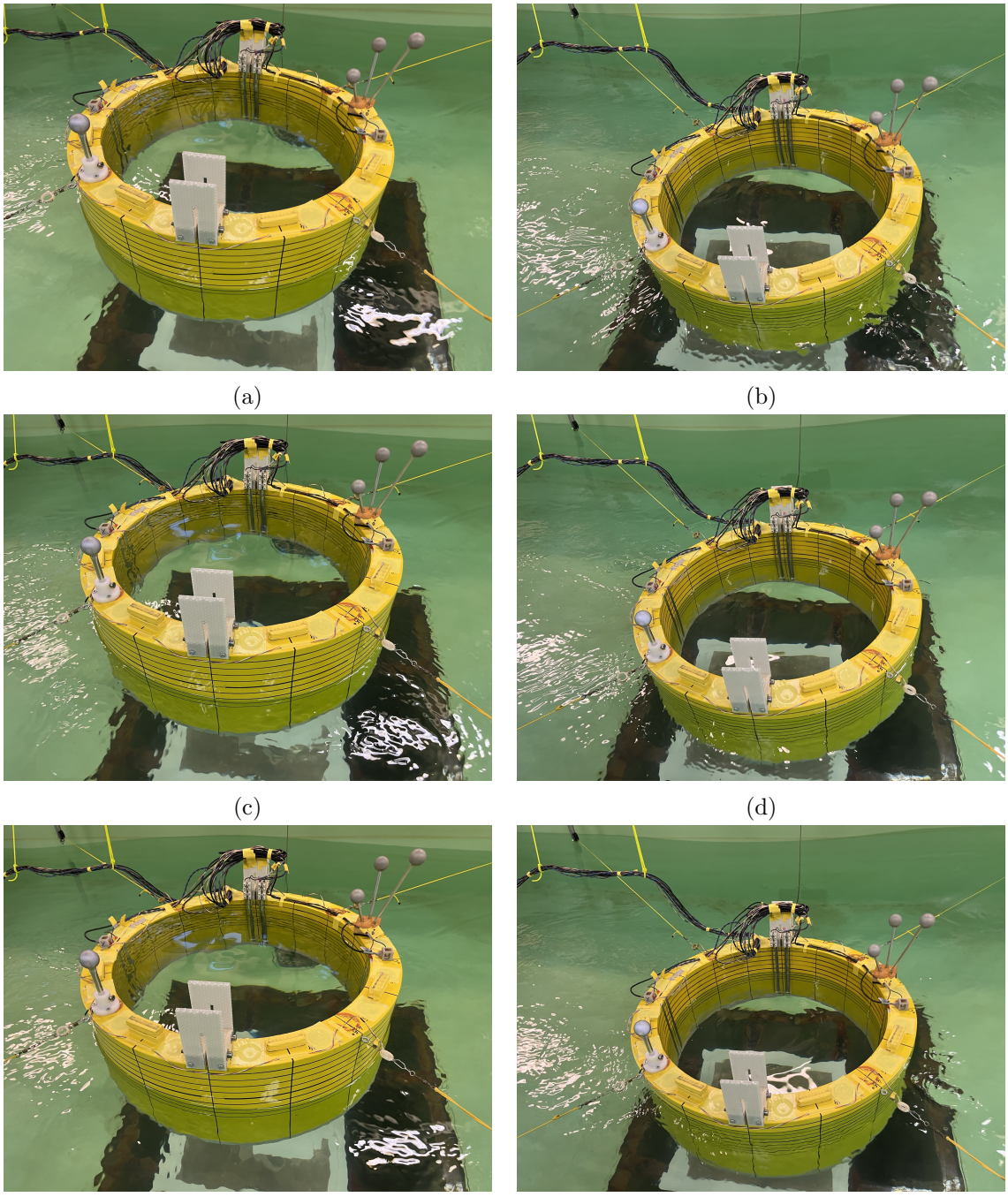

(a) (b) (c) (d) (e) (f)

Figure 6.17: Piston mode at different time instances for approximately kR=1.4.

Comments on the Experimental Results

After the experiments were finalized, it was discovered that the range of tested wave numbers were not as originally intended. Wave numbers equivalent to wave period 0.5 to 2.3s with steps of 0.05s was the initial plan. The method used of converting this set of wave periods to wave numbers yielded the following results: a larger amount of wave numbers was generated for low wave periods and a fewer amount of wave numbers were generated for high wave periods. As an example, the step from kR 0.5 to 0.37 is equivalent to wave period 1.8 to 2.3s meaning the model have not been subject to wave numbers equivalent to wave period between 1.8 and 2.3s which is unfortunate. This could also give an additional explanation for the discrepancies between the numerical and experimental results.

Chapter 7

Conclusion and Further Work

The work conducted in this thesis have yielded results indicating clear influence of different types of damper plates as well as influence of the moonpool on the rigid body motion. This chapter aims to conclude the main findings and propose further investigation areas that might be of interest.

7.1 Conclusion

This thesis have investigated mainly the rigid body motion of a floating offshore wind turbine concept made by Sevan SSP. The concept is a circular structure with a large circular moonpool taking up a substantial portion of the concept. The main goal have been on testing different sizes of horizontal damper plates as well as include a new design configuration with vertical damper plates situated inside the moonpool with the intention on reducing the motion in specifically pitch. The results shows that configuration 5 seem to yield the lowest response at the lowest kR numbers up towards kR=1 where it then shows larger response than the other horizontal damper plates. This is the configuration with the largest horizontal damper plate. With regards to the original objective of reducing the pitch motion by 25% at wave periods around 1.2-1.4 seconds, equivalent to kR=0.7-0.9, the different horizontal damper plates showed little variation on this front but configuration 5 yielded the lowest response at those kR numbers. The vertical damper plates was implemented with this objective in mind, which unfortunately also showed no improvement on the pitch motion. There was some reduction in surge for kR=3-5.2 but no other than that. A concluding thought on the varying damper plates; it is evident from the results that both inner and outer skirt is more beneficial than the other configurations.

For this concept, sloshing effects proved to be quite significant where the first sloshing mode more or less cancel out the motion in surge at specific frequencies. Because of the different damper plates, this cancellation effect occur between kR=1.8-2.5 depending on the present horizontal damper plates. The piston-mode resonance frequency where

estimated to be at kR=1.371 for configuration 1 where this had an impact on the response in heave.

The largest discrepancy between the numerical and experimental results took place for the pitch motion. Also, the numerical results deviated more from the experimental with the presence of both inner and outer skirts. This indicates that viscous damping and viscous excitation is significant in estimating the motion in pitch with the presence of horizontal damper plates.

7.2 Further Work

A considerable amount of time have been spent on planning and execution of the experiment as well as post-processing the experimental results. It was initially planned to perform model tests in irregular waves but time did not allow for it. It would be interesting to subject the model to sea states in areas close to resonant frequencies in order to investigate the response this might have on the body.

The model have been subject to only one variation of the vertical damper plate. Even tough it showed little improvement on the rigid body motion, it would be interesting to further investigate the influence of vertical damper plates by varying the size and perforation ratio on these plates. Since a variety of horizontal damper plate sizes have been tested, a future work could be to test different design of these plates where they are designed in a more wedge shape rather than completely horizontal. This could reduce the excitation loads that are induced on the body which could ultimately reduce the motion.

Estimating the forces that is developed in the mooring lines is an area that is important to evaluate in designing a concept from start to finish which would be recommended as further work. In general, no loads have been evaluated in this thesis and the logical step forward when a functional design have been obtained, is to evaluate the wave induced loads acting on the structure in order to the stress that occur in the structure.

The model had a scale ratio of 1:100, and for future work it would be beneficial to use a larger model for two reasons: The negative effect of scaling with regards to ensuring equality in Froude number and Reynolds number simultaneously would be reduced. The influence from the instrumentation cable bundle would be reduced if the model was larger. These reasons would yield results more representative for full scale.

References

Bachynski-Polic, E. E., T. Kristiansen and D. Myrhaug (2021). *Marine Dynamics Compendium*. Department of Marine Technology, Faculty of Engineering, NTNU.

Faltinsen, O. M. (1990). *Sea loads on ships and offshore structures*. Cambridge University Press.

Faltinsen, O. M. and A. N. Timokha (2009). *Sloshing*. Cambridge University Press.

Jiang, Z. et al. (2020). 'Design, modelling, and analysis of a large floating dock for spar floating wind turbine installation'. In: *Marine Structures* 72, p. 102781. ISSN: 0951-8339. DOI: https://doi.org/10.1016/j.marstruc.2020.102781. URL: https://www.sciencedirect.com/science/article/pii/S0951833920300757.

LHEEA-Lab (2022). *NEMOH-Presentation*. URL: https://lheea.ec-nantes.fr/research-impact/software-and-patents/nemoh-presentation (visited on 15/12/2022).

Massachusetts Institute of Technology Inc and WAMIT Inc (2020). *WAMIT User Manual, Version 7.4*. WAMIT, Inc. URL: https://www.wamit.com/manualupdate/v74_manual.pdf (visited on 08/12/2022).

Mciver, P. and D.V. Evans (1984). 'The occurrence of negative added mass in free-surface problems involving submerged oscillating bodies'. In: *Journal of Engineering Mathematics* 18, pp. 7–22. DOI: 10.1007/BF00042895.

Molin, B. (2001). 'On the piston and sloshing modes in moonpools'. In: *Journal of Fluid Mechanics* 430, pp. 27–50. DOI: 10.1017/S0022112000002871.

Molin, B. et al. (2018). 'On natural modes in moonpools and gaps in finite depth'. In: *Journal of Fluid Mechanics* 840, pp. 530–554. DOI: 10.1017/jfm.2018.69.

Moreau, M. et al. (2022). 'An upright bottomless vertical cylinder with baffles floating in waves'. In: *Applied Ocean Research* 119. ISSN: 0141-1187. DOI: https://doi.org/10.1016/j.apor.2021.102934. URL: https://www.sciencedirect.com/science/article/pii/S0141118721004016.

Mukhlas, M. (2017). 'Roll Damping Investigation of Two-Dimensional Ship Section with Bilge-Boxes'. URL: http://hdl.handle.net/11250/2453079.

Newman, J.N. (2017). *Marine Hydrodynamics, 40th Anniversary Edition*. The MIT Press.

Qualysis (2023). *Motion Capture*. URL: https://www.qualisys.com/product-tag/oqus/ (visited on 18/05/2023).

Reiersen, L.M.U et al. (2021). 'Investigation of moonpools as pitch motion reducing device'. In: *Applied Ocean Research* 108. ISSN: 0141-1187. DOI: https://doi.org/10.1016/j.apor.2020.102477. URL: https://www.sciencedirect.com/science/article/pii/S0141118720310361.

SevanSSP (2022). *Master thesis presentation.*

Steen, S. (2014). *Compendium: Experimental Methods in Marine Hydrodynamics.* Department of Marine Technology, Faculty of Engineering, NTNU.

Wettre, S. H. R. (2022). 'Numerical and Experimental Investigation of a Floating Offshore Wind Turbine Foundation with a Moonpool and Inner and Outer Skirts'. URL: https://hdl.handle.net/11250/3028950.

Appendix A

Additional RAO

Conf 1 and 7, Wave steepness 1/40 and 1/60

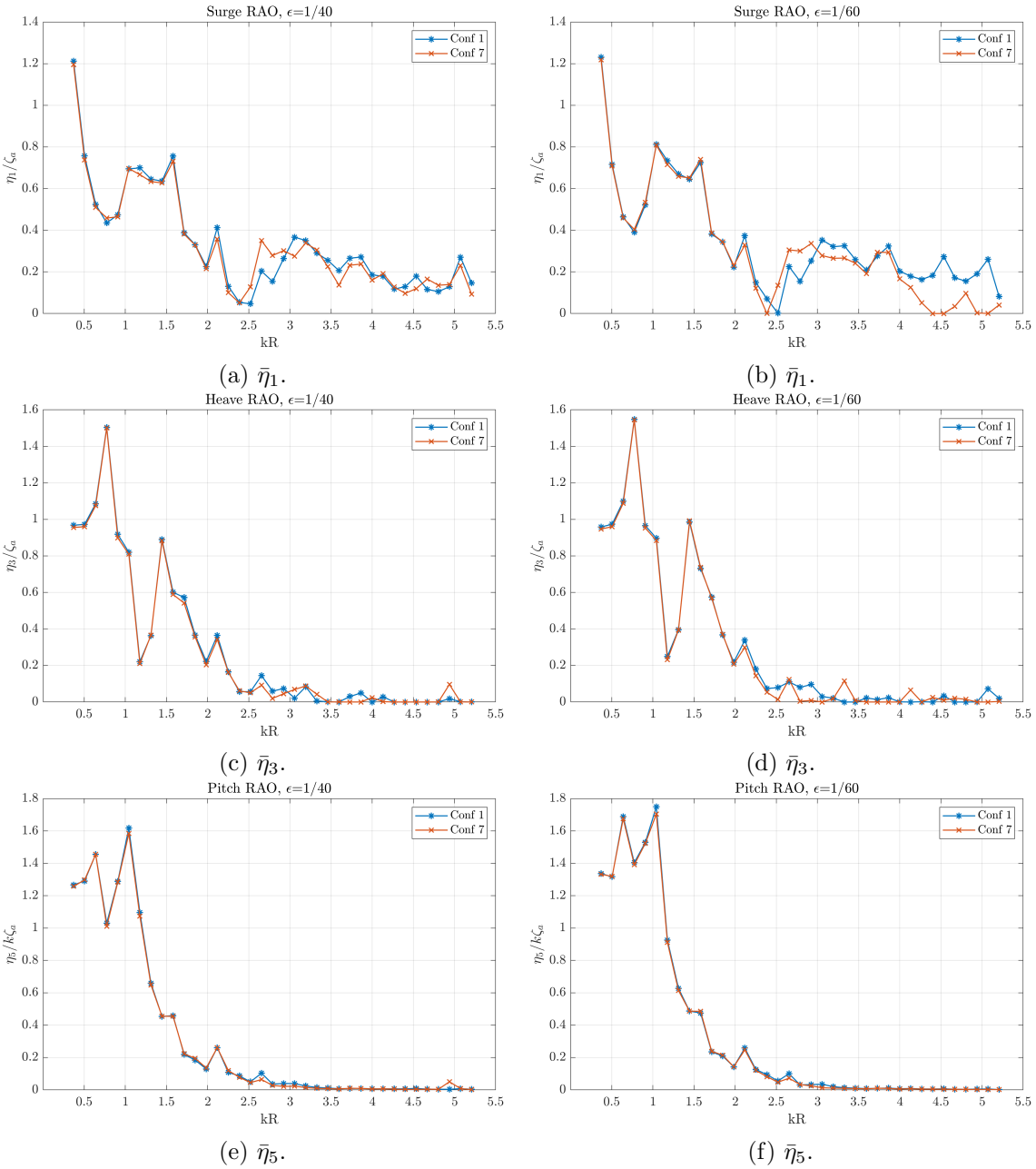

(a) $\bar{\eta}_1$. (b) $\bar{\eta}_1$.

(c) $\bar{\eta}_3$. (d) $\bar{\eta}_3$.

(e) $\bar{\eta}_5$. (f) $\bar{\eta}_5$.

Figure A.1: RAO in surge, heave and pitch for configuration 1 and 7 for wave steepness 1/30 and 1/100.

Conf 2 and 8, wave steepness 1/40 and 1/60

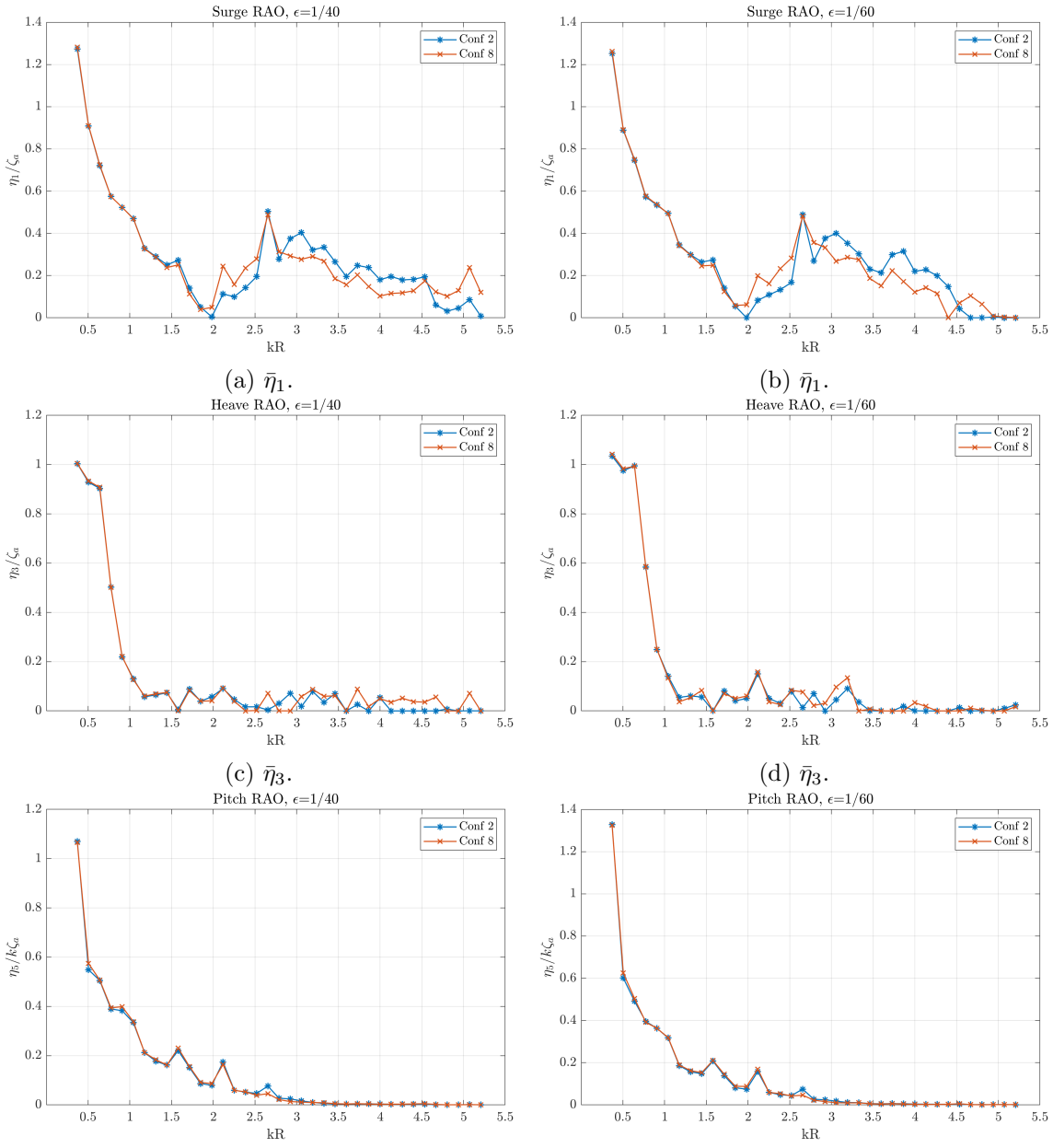

(a) $\bar{\eta}_1$. (b) $\bar{\eta}_1$.

(c) $\bar{\eta}_3$. (d) $\bar{\eta}_3$.

(e) $\bar{\eta}_5$. (f) $\bar{\eta}_5$.

Figure A.2: RAO in surge, heave and pitch for configuration 2 and 8 for wave steepness 1/40 and 1/60.

Conf 2 to 6, wave steepness 1/40 and 1/60.

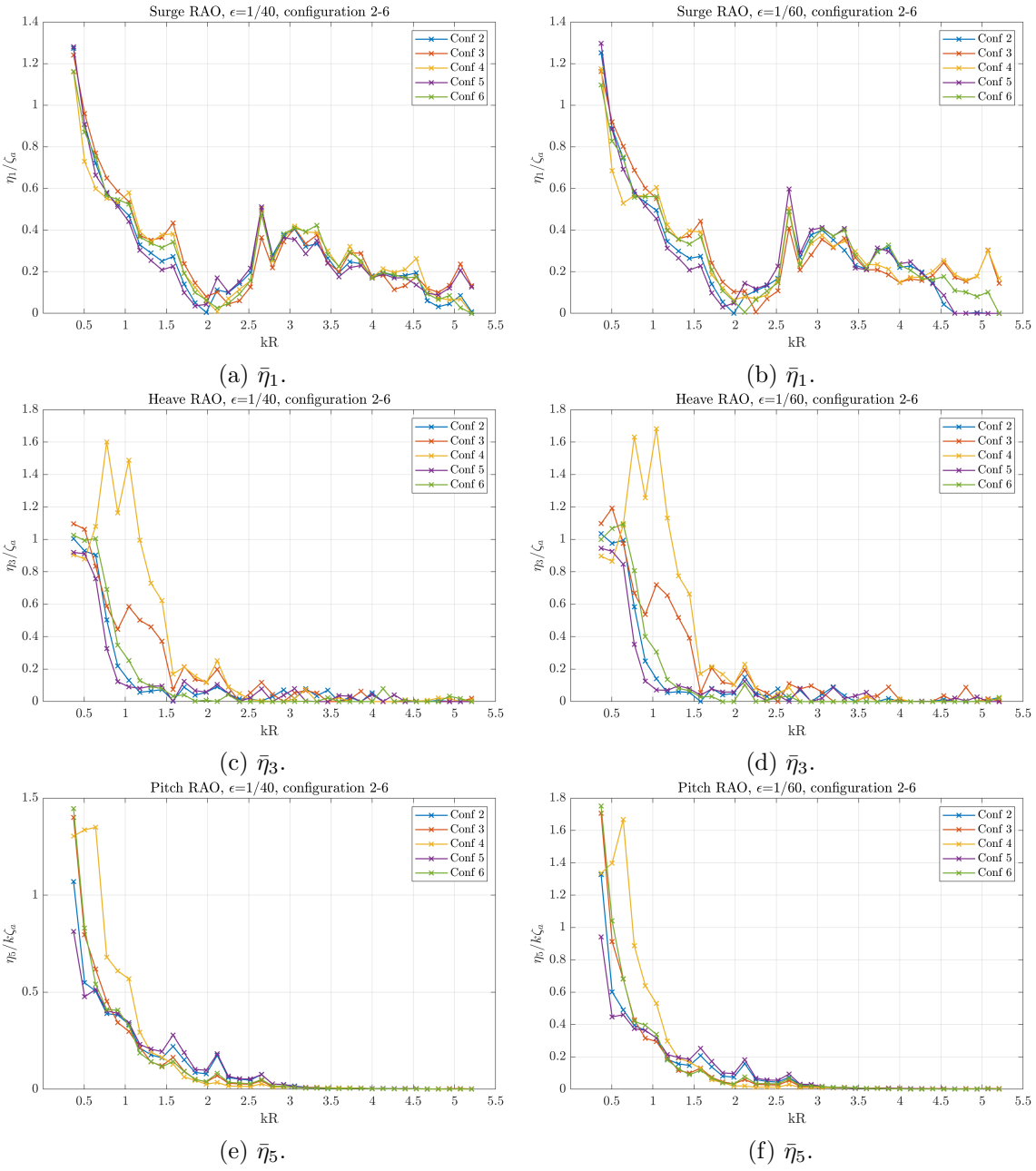

(a) $\bar{\eta}_1$.

(b) $\bar{\eta}_1$.

(c) $\bar{\eta}_3$.

(d) $\bar{\eta}_3$.

(e) $\bar{\eta}_5$.

(f) $\bar{\eta}_5$.

Figure A.3: RAO in surge, heave and pitch for configuration 2 to 6 for wave steepness 1/40 and 1/60.

Appendix B

Added Mass and Damping

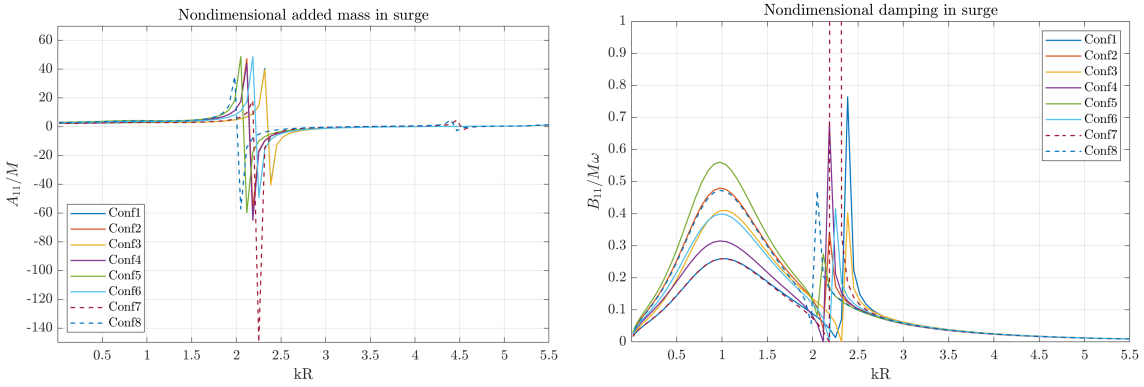

(a) $\bar{\eta}_1$.

(b) $\bar{\eta}_1$.

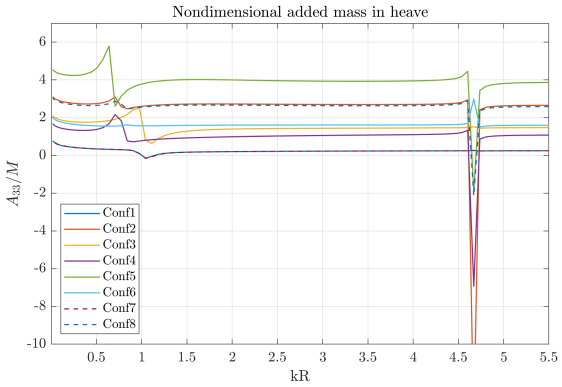

(c) $\bar{\eta}_3$.

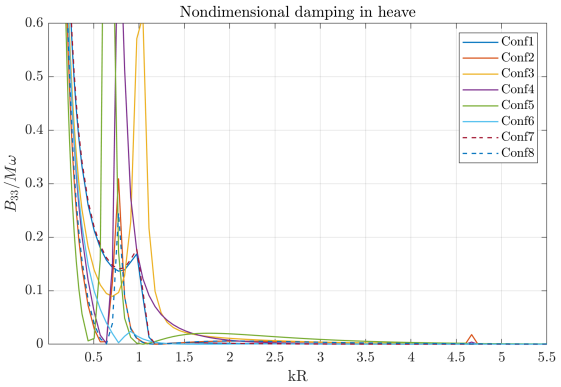

(d) $\bar{\eta}_3$.

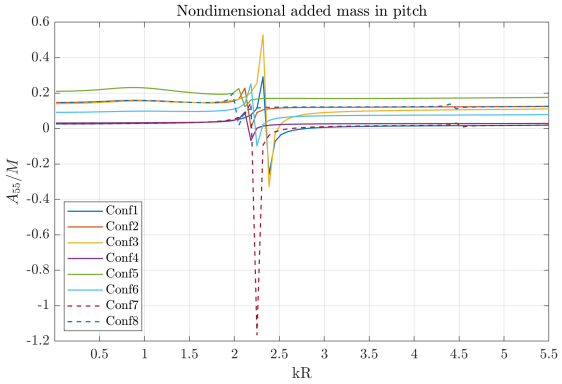

(e) $\bar{\eta}_5$.

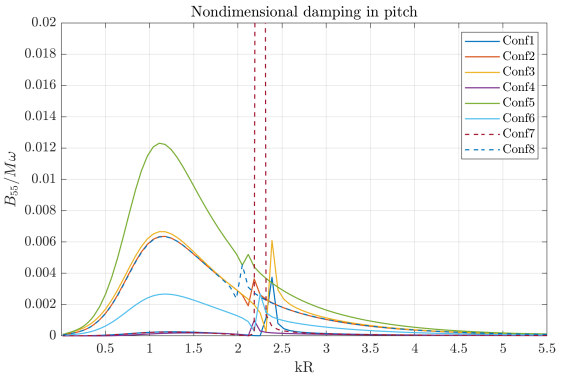

(f) $\bar{\eta}_5$.

Figure B.1: Added mass and damping from Wamit with infite water depth

Appendix C

Free-surface Elevation

Wave steepness 1/100

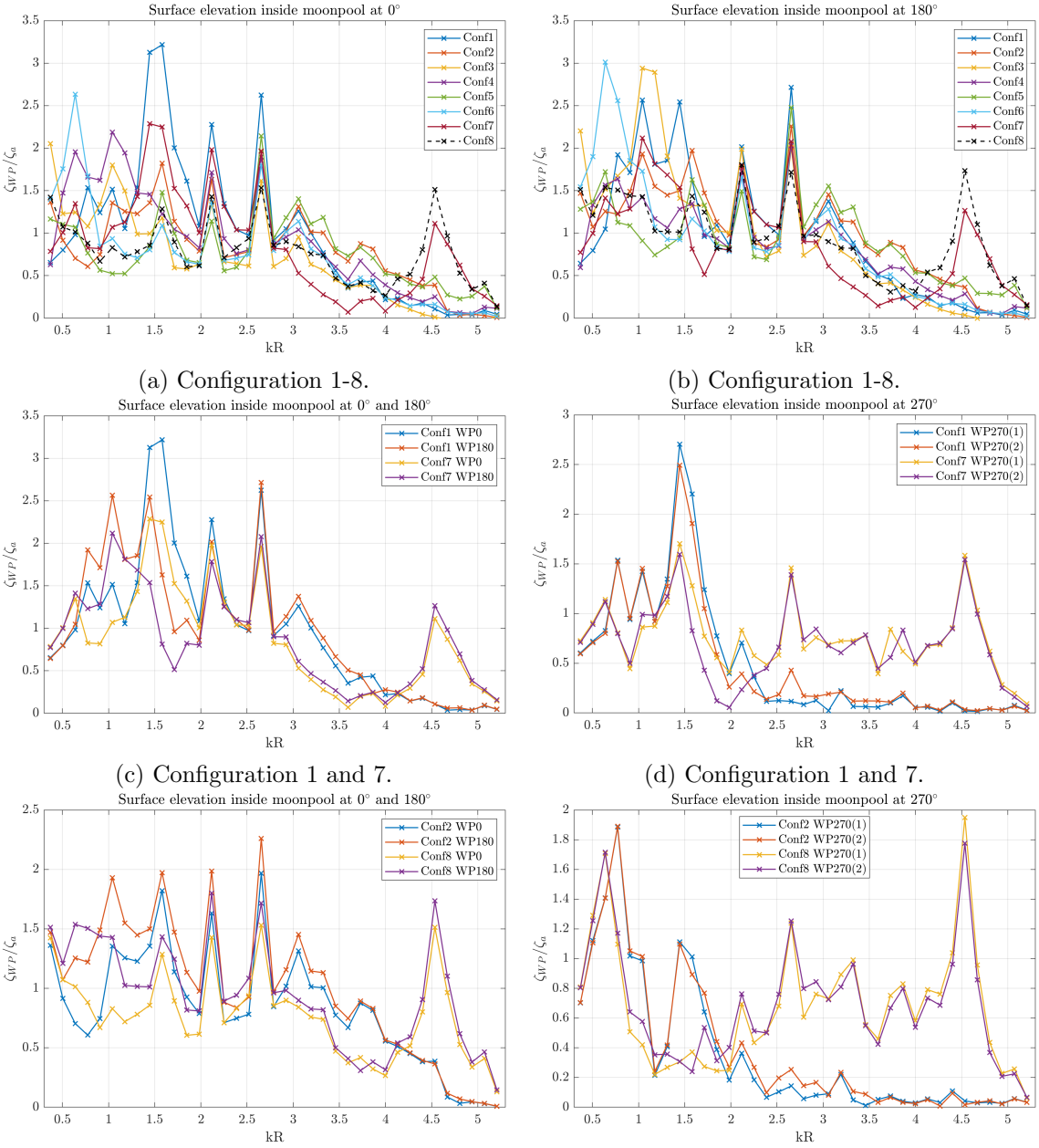

(a) Configuration 1-8.

(b) Configuration 1-8.

(c) Configuration 1 and 7.

(d) Configuration 1 and 7.

(e) Configuration 2 and 8.

(f) Configuration 2 and 8.

Figure C.1: Free surface elevation inside moonpool for all configurations for wave steepness 1/100 at 0° and 180° in a) and b) respectively. A detailed comparison at 0, 180 and 270° between configuration 1 and 7 in c) and d) and between configuration 2 and 8 in e) and f).

Wave Steepness 1/60

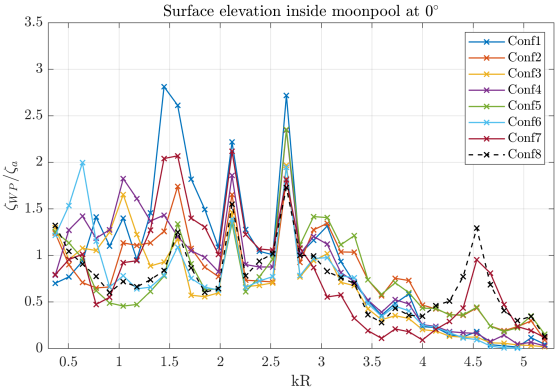

(a) Configuration 1-8.

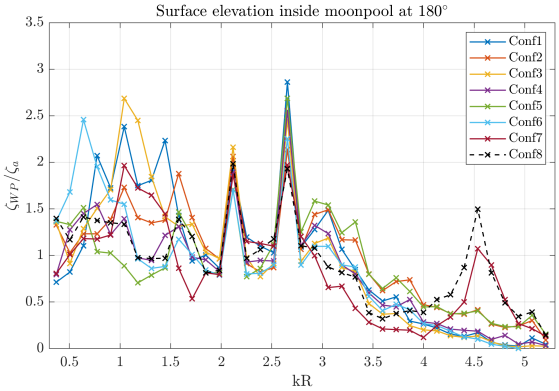

(b) Configuration 1-8.

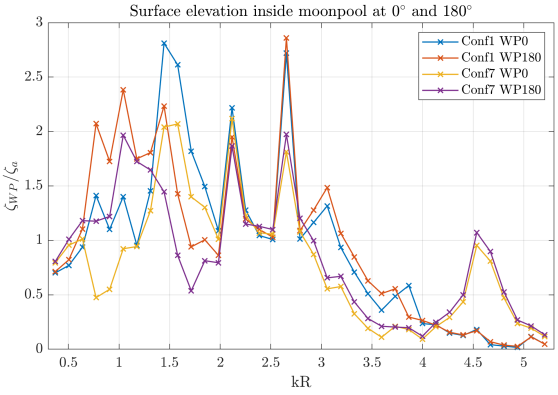

(c) Configuration 1 and 7.

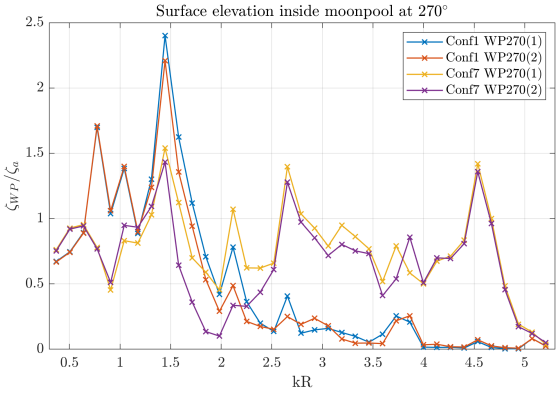

(d) Configuration 1 and 7.

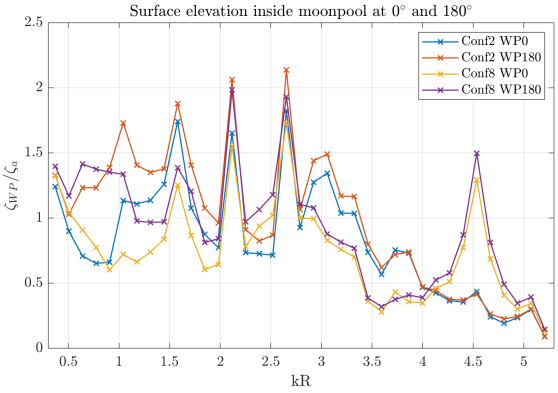

(e) Configuration 2 and 8.

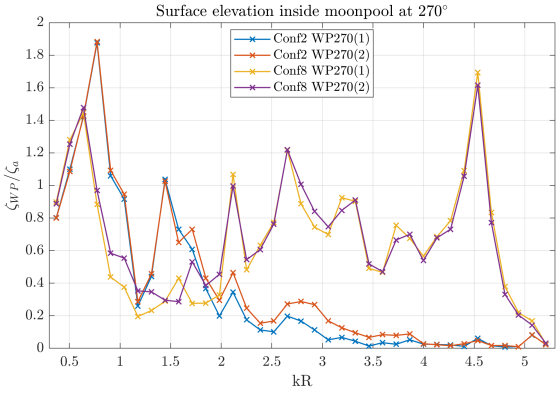

(f) Configuration 2 and 8.

Figure C.2: Free surface elevation inside moonpool for all configurations for wave steepness 1/60 at 0° and 180° in a) and b) respectively. A detailed comparison at 0, 180 and 270° between configuration 1 and 7 in c) and d) and between configuration 2 and 8 in e) and f).

Wave Steepness 1/40

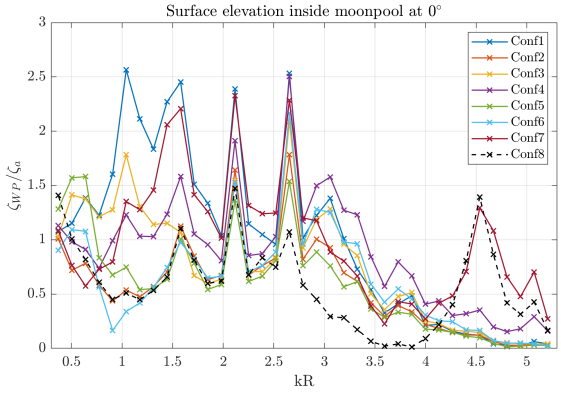

(a) Configuration 1-8.

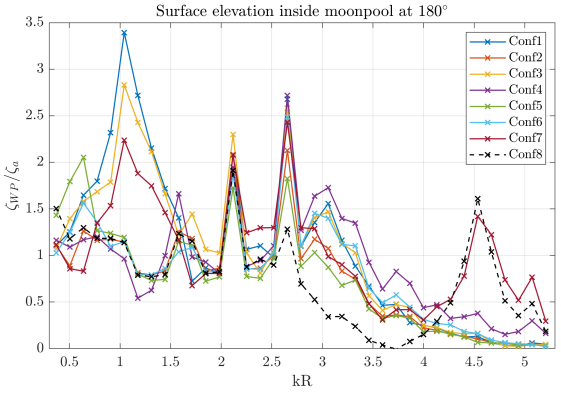

(b) Configuration 1-8.

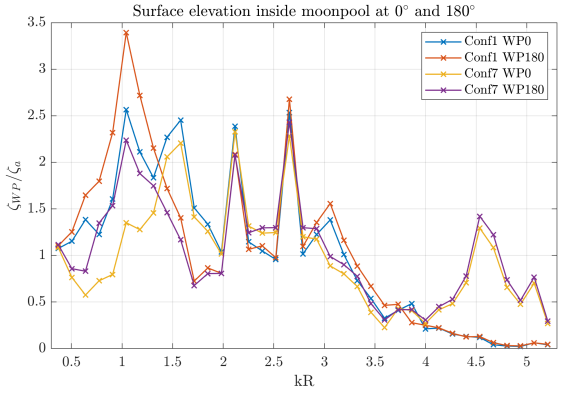

(c) Configuration 1 and 7.

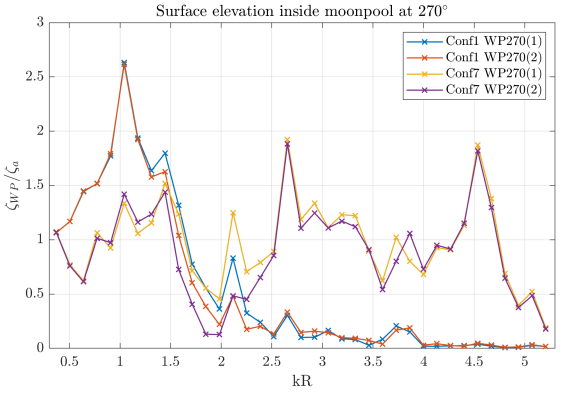

(d) Configuration 1 and 7.

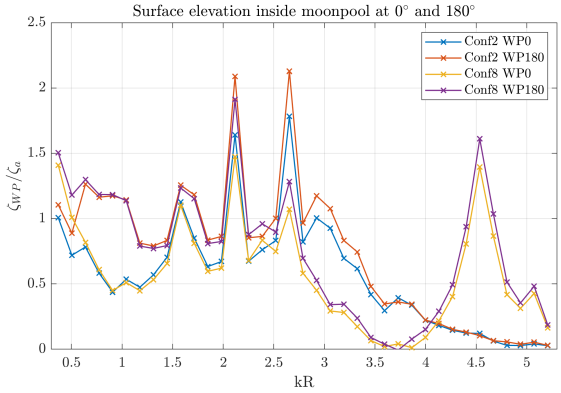

(e) Configuration 2 and 8.

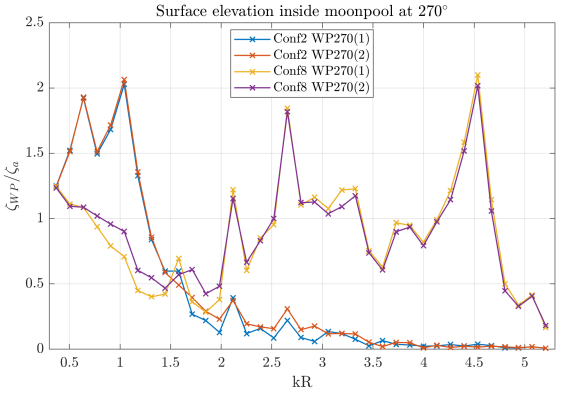

(f) Configuration 2 and 8.

Figure C.3: Free surface elevation inside moonpool for all configurations for wave steepness 1/40 at 0° and 180° in a) and b) respectively. A detailed comparison at 0, 180 and 270° between configuration 1 and 7 in c) and d) and between configuration 2 and 8 in e) and f).

Appendix D

Viscous Damping Study

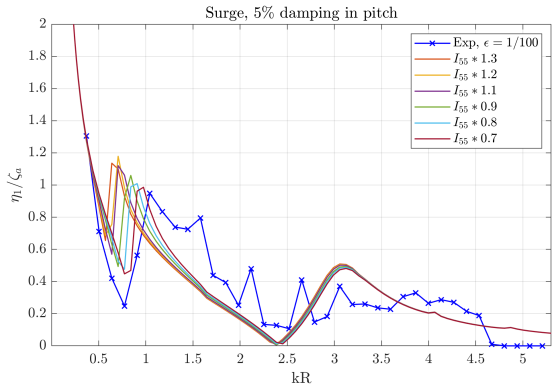

(a) $\bar{\eta}_1$

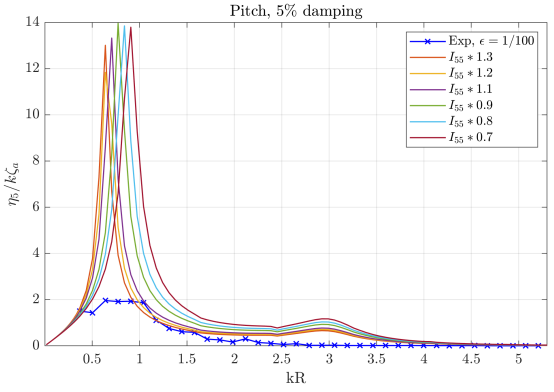

(b) $\bar{\eta}_5$

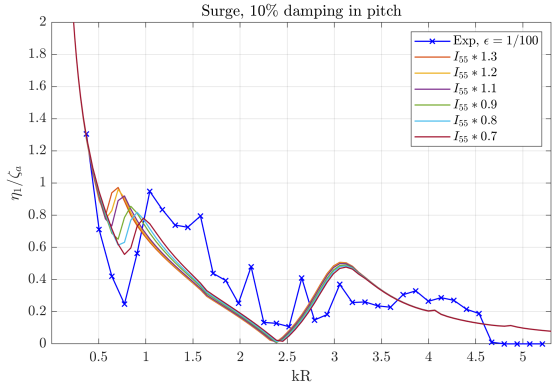

(c) $\bar{\eta}_1$

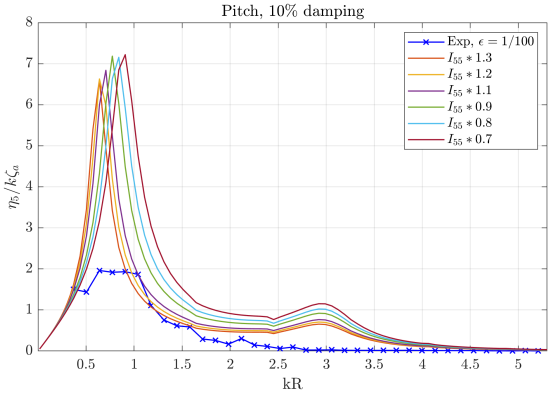

(d) $\bar{\eta}_5$

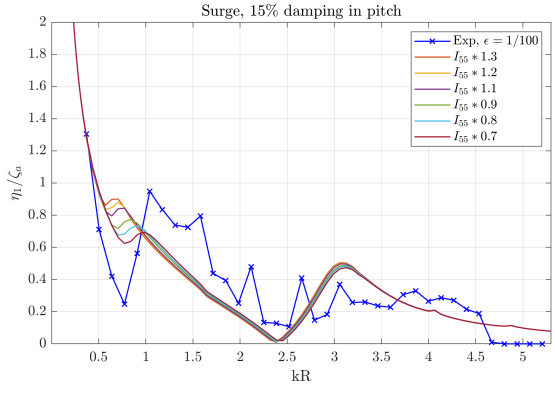

(e) $\bar{\eta}_1$

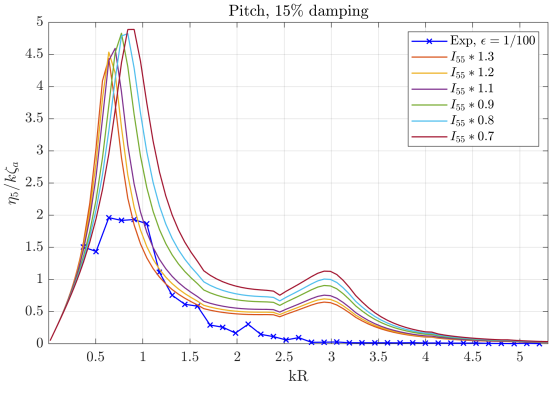

(f) $\bar{\eta}_5$

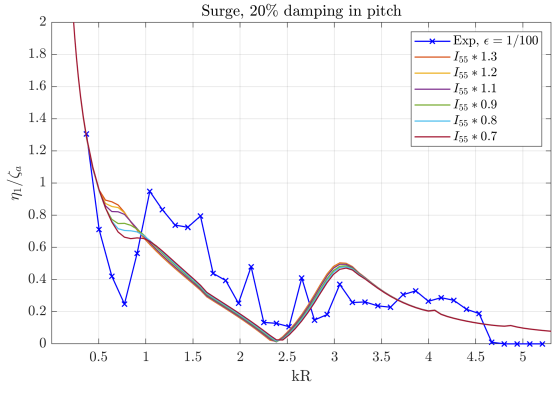

(g) $\bar{\eta}_1$

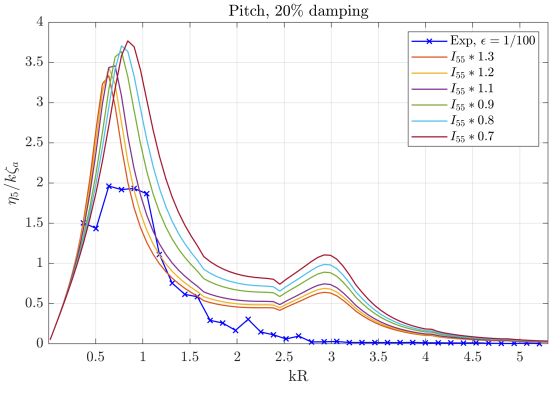

(h) $\bar{\eta}_5$

Figure D.1: Viscous damping study for configuration 1.

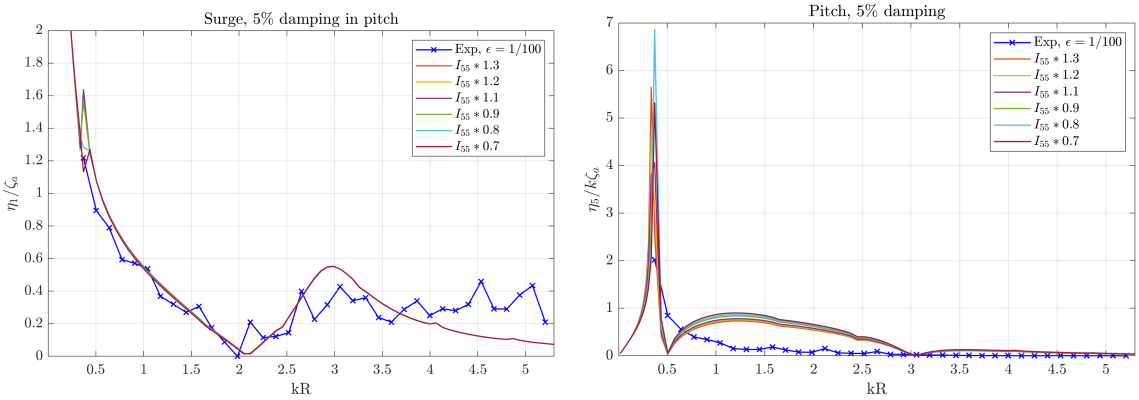

(a) $\bar{\eta}_1$

(b) $\bar{\eta}_5$

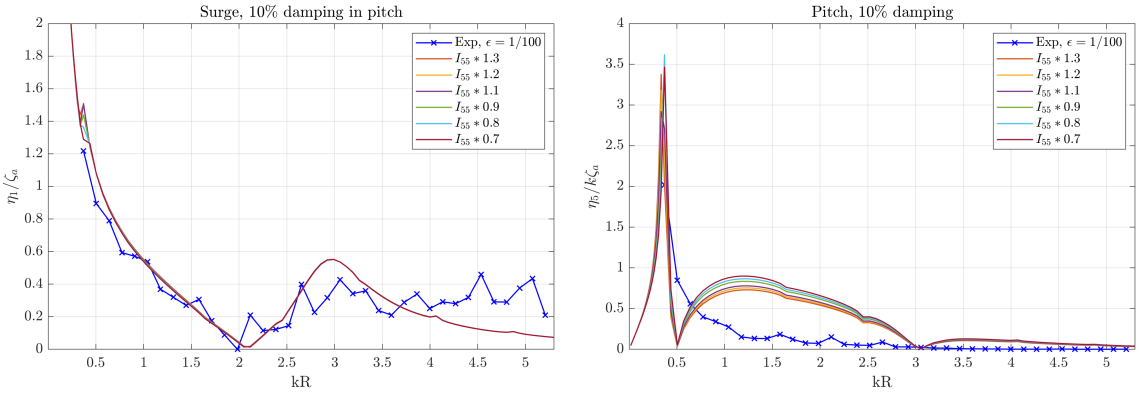

(c) $\bar{\eta}_1$

(d) $\bar{\eta}_5$

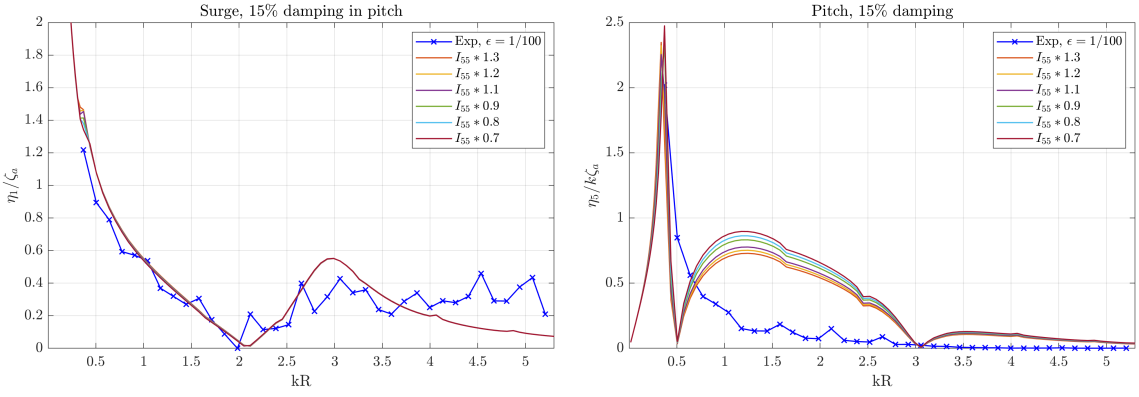

(e) $\bar{\eta}_1$

(f) $\bar{\eta}_5$

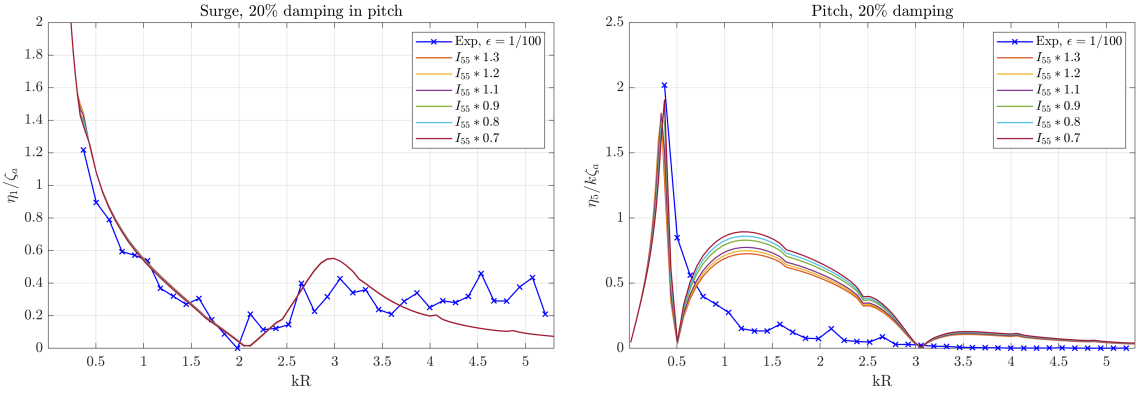

(g) $\bar{\eta}_1$

(h) $\bar{\eta}_5$

Figure D.2: Viscous damping study for configuration 2.

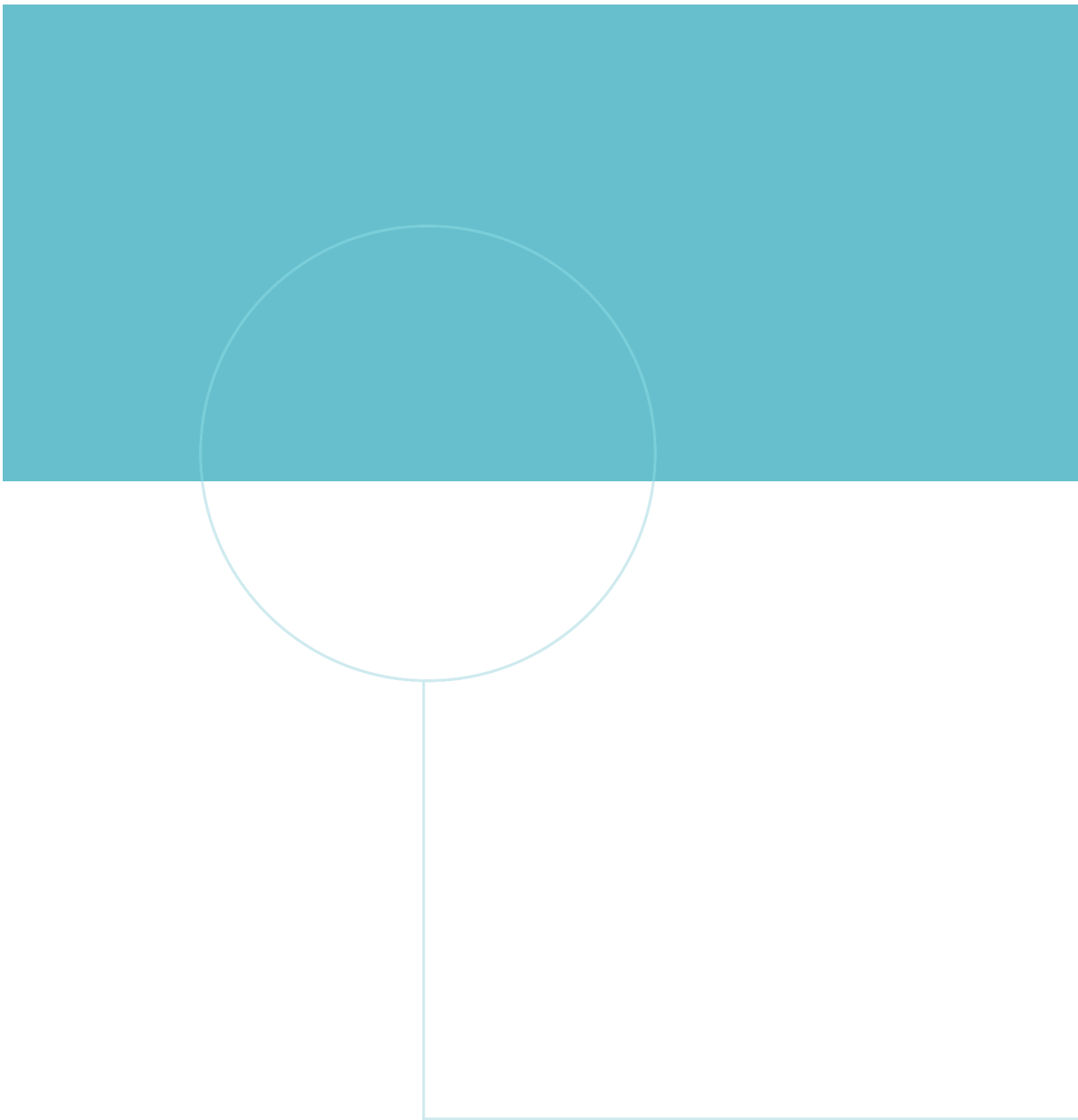

NTNU

Norwegian University of
Science and Technology